TAP2 - PAT2

PROGRAMME TO STIMULATE
KNOWLEDGE TRANSFER
IN AREAS OF STRATEGIC IMPORTANCE

An Aluminium alloy improved by ECAP and formed by SPIF process

ALECASPIF

A.M. HABRAKEN ET AL. (ULG)
A. ROSOCHOWSKI ET AL. (UNIVERSITY OF STRATHCLYDE)
B. VERLINDEN, J. DUFLOU ET AL. (KULEUVEN)
A. SCHMITZ, P. POUTEAU (CRM)

STANDARDISATION

TELECOMMUNICATIONS

SPACE SECTOR

CLEAN TECHNOLOGIES

NEW MATERIALS

.be

PROGRAMME TO STIMULATE KNOWLEDGE TRANSFER IN AREAS OF STRATEGIC IMPORTANCE

TAP2

FINAL REPORT

AN ALUMINIUM ALLOY IMPROVED BY ECAP AND FORMED BY SPIF PROCESS

ALECASPIF

P2/00/01

Promoters

Anne Marie Habraken
University of Liège, Dept. ArGEnCo, Chemin des chevreuils, 1/B52, B-4000 Liège
Andrzej Rosochowski
University of Strathclyde, 16 Richmond Street, Glasgow G1 1XQ, United Kingdom
Bert Verlinden
University of Leuven, Dept. MTM, Kasteelpark Arenberg 44, B-3001 Heverlee-Leuven
Joost Duflou
University of Leuven, Dept. PMA, Celestijnenlaan 300B, B-3001 Heverlee-Leuven
Alain Schmitz
CRM (Centre for Research in Metallurgy), Avenue du Bois St Jean 21, B-4000 Liège

Authors

Anne Marie Habraken, Chantal Bouffioux, Cédric Lequesne (*University of Liège*)
Andrzej Rosochowski, Malgorzata Rosochowska (*University of Strathclyde*)
Bert Verlinden, Vanessa Vidal, George Dragos Ailinca (*University of Leuven*)
Joost Duflou, Hans Vanhove (*University of Leuven*)
Alain Schmitz, Philippe Pouteau *(CRM)*

D/2010/1191/16
Published in 2010 by the Belgian Science Policy
Avenue Louise 231
Louizalaan 231
B-1050 Brussels
Belgium
Tel: +32 (0)2 238 34 11 – Fax: +32 (0)2 230 59 12
http://www.belspo.be

Contact person: *Anna Calderone*
Secretariat: +32 (0)2 238 34 80

A. M. Habraken, C. Bouffioux, C. Lequesne, A. Rosochowski, M. Rosochowska, B. Verlinden, V. Vidal, G. Ailinca, J. Duflou, H. Vanhove, A. Schmitz, P. Pouteau, ***An Aluminium alloy improved by ECAP and formed by SPIF process – ALECASPIF***, Final Report, Belgian Science Policy (Programme to stimulate knowledge transfer in areas of strategic importance – TAP2), Brussels, 2010, 112 p.

Table of contents

Résumé

1. Contexte

L'industrie aéronautique recherche constamment des moyens de réduire le poids des pièces et de la structure des avions. Ainsi, la disponibilité d'un nouveau matériau de la famille des alliages d'aluminium AlMgSc rassemblant les avantages d'un poids spécifique bas, d'une grande résistance à la corrosion, d'une grande solidité et d'une bonne soudabilité, représente un grand intérêt dans ce domaine. Le choix de ce matériau a été guidé par un partenaire industriel: la Sonaca.

Dans le but d'augmenter encore la résistance de l'alliage d'aluminium choisi, le matériau a été soumis à un des différents procédés de déformation plastique sévère (**SPD**) tel qu'une nouvelle méthode d'extrusion angulaire à section constante (incrémental ou non): **IECAP** et **ECAP** ou tel que le laminage à froid asymétrique (**ACR**).

Mais grande résistance est souvent corrélée avec diminution de formabilité: ainsi des risques de fractures sont observés lorsque des matériaux très résistants sont soumis à des méthodes de formage classiques.

La nouvelle méthode, très flexible, de formage incrémental à point unique (**SPIF**) a la particularité de permettre de plus grandes déformations que les techniques classiques de formage. De plus, le procédé requiert le seul usage d'un outil générique, ce qui permet d'éliminer des frais d'outillages spécifiques et de réduire les délais de production. En outre, ce procédé est compatible avec les pièces aéronautiques classiques.

Le but de combiner le choix d'un alliage spécifique **AL**MgSc, l'application des méthodes SPD telles que: I-**ECA**P, **ECA**P ou ACR et le procédé **SPIF** dans le projet: **ALECASPIF** est de produire diverses pièces aéronautiques tout en réduisant considérablement le poids. L'ensemble de ces procédés apporte une valorisation considérable concernant la réduction des frais de fabrication grâce aux réductions des frais d'outillage, un gain de temps ainsi qu'un allègement des composants avec, par conséquence, un intérêt écologique.

2. Objectifs

Le premier objectif du projet ALECASPIF est de tester les trois techniques SPD (I-ECAP, ECAP et ACR) sur l'alliage d'AlMgSc dans son état initial pour voir comment il est possible de raffiner les grains. Le matériau initial et les "nouveaux matériaux"

produits ont été caractérisés et comparés pour voir l'impact des procédés de raffinement sur leurs propriétés.

Le deuxième objectif était de caractériser le matériau initial vu son très grand intérêt pour les industriels pour ses très bonnes propriétés mécaniques et superplastiques.

Le troisième était de vérifier la possibilité d'appliquer le procédé SPIF aux différents matériaux et d'établir un modèle analytique pour prédire la force de formage.

Et enfin, le dernier objectif était de développer la modélisation numérique du procédé SPIF par la méthode des éléments finis pour pouvoir prédire la force de formage nécessaire et la forme finale d'une pièce formée en combinant une bonne précision et une durée de simulation modérée.

3. Conclusions

Les résultats de cette recherche ont montré que:

1. Le procédé ACR apporte un important durcissement du matériau mais pas encore de raffinement des grains parce que le cisaillement n'est pas suffisant pour les réduire.
2. Malgré des problèmes de géométrie d'éprouvettes et des tâches manuelles à résoudre, le procédé I-ECAP a pu être appliqué à des barres, des plaques et des feuilles. Il est très prometteur car il raffine considérablement la structure des grains de l'alliage AlMgSc. De plus, la conception de l'outillage permet de réduire la force à fournir et, de plus, peut être appliquée à de longues pièces.
3. Le procédé ECAP a pu être exploité sur des pièces cylindriques mais, après six passages, les éprouvettes n'atteignaient toujours pas l'état submicronique. Contrairement à l'aluminium pur, ce problème peut provenir de la présence de nano particules.
4. Il a été montré que le procédé SPIF est applicable au matériau initial avec une inclinaison de parois de maximum 46°, ce qui correspond à une faible formabilité. Un modèle analytique permettant de prédire la force de formage nécessaire a été développé pour ce matériau ainsi qu'une formule générale adaptée pour tout matériau.
5. De nombreux tests mécaniques ont été réalisés sur le matériau initial et ont ainsi permis de connaître le comportement du matériau à température ambiante. Une loi constitutive a été choisie pour décrire son comportement élasto-plastique et son écrouissage, les paramètres du matériau ont été identifiés.
6. Le domaine superplastique (température et vitesse de déformation) a été localisé, une loi a été choisie et les paramètres ajustés.

7. Un modèle numérique utilisant la méthode des éléments finis a été adapté pour simuler rapidement le procédé SPIF et pour prédire avec précision la force appliquée par l'outil sur la tôle initiale ainsi que la forme en fin de processus.

4. Apport du projet dans un contexte d'appui scientifique au transfert des connaissances et à l'innovation

La caractérisation du matériau et les informations concernant le domaine superplastique sont des données utiles pour le fournisseur du matériau: Aleris ainsi que pour le partenaire industriel utilisant ce matériau: Sonaca.

Les recherches effectuées ont permis d'améliorer les nouvelles techniques SPD: de résoudre des problèmes techniques et de connaître les caractéristiques du matériau après transformation. Ce nouveau matériau amélioré peut être utile dans le domaine aéronautique (plus grande résistance que le matériau initial).

L'applicabilité du procédé SPIF sur le matériau initial ainsi que son modèle de prédiction de la force sont des informations intéressantes puisque ce matériau est difficile à mettre en forme et que la technique du SPIF est adaptée aux petites séries de production comme c'est le cas pour des pièces du domaine aéronautique.

L'amélioration du modèle numérique du procédé SPIF permet de prédire des informations essentielles (force, forme) sur le procédé SPIF permettant ainsi de réduire le nombre d'expériences nécessaires.

5. Mots-clés

Formage Incrémental, Grains Ultra Fins, Extrusion Angulaire à Section Constante (Incrémental), Identification des Paramètres Matériaux, Simulation par Eléments Finis, Alliage d'Aluminium AlMgSc.

Samenvatting

1. Context

De luchtvaartindustrie is voortdurend op zoek naar mogelijkheden om het gewicht van onderdelen en structuren te verminderen. De beschikbaarheid van een nieuw materiaal van de AlMgSc familie, dat een laag specifiek gewicht combineert met een hoge corrosieweerstand, een hoge taaiheid en een excellente lasbaarheid, is hierbij van groot belang. Een industriële partner -Sonaca- heeft ons begeleid bij de keuze voor dit materiaal.

Een aantal technieken gebaseerd op het aanbrengen van een zeer grote plastische vervorming (**S**evere **P**lastic **D**eformation: **SPD**), zoals ECAP (**E**qual **C**hannel **A**ngular **P**ressing) of **I-ECAP** (**I**ncremental **E**qual **C**hannel **A**ngular **P**ressing) en **ACR** (**A**symmetrical **C**old **R**olling) werden uitgetest met de bedoeling om de sterkte van dit materiaal nog verder te verhogen.

In veel gevallen gaat een hogere sterkte gepaard met een lagere vervormbaarheid. Deze beperking kan bij de vormgeving van sterke materialen met behulp van klassieke vormgevingstechnieken, leiden tot het falen van het materiaal.

Single **P**oint **I**ncremental **F**orming (**SPIF**) is een ontluikende vormgevingstechniek die erg flexiebel is en die toelaat om materialen veel sterker te vervormen dan met klassieke technieken. Bovendien vereist deze techniek een relatief eenvoudige generische vormgevingsmachine,wat toelaat om de machinekosten tot een minimum te beperken en de standtijden te verkorten. Deze vormgevingsmethode is toepasbaar voor de productie van conventionele vliegtuigonderdelen.

De combinatie van een specifieke legering (**Al**MgSc), de SPD technieken zoals **ECA**P, I-**ECA**P of ACR en een nieuwe vormgevingstechniek **SPIF** in het project **ALECASPIF** heeft tot doel om de weg te openen naar de vervaardiging van vliegtuigonderdelen met sterk gereduceerd gewicht. Het voorgestelde proces leidt tot een potentiële valorisatie op gebied van verminderde productiekosten omwille van een gereduceerde infrastructuurkost, een kortere productietijd en lichtere componenten wat dus ook een ecologische voordeel oplevert.

2. Doelstellingen

De eerste doelstelling van het ALECASPIF project was het uittesten van drie SPD technieken (ECAP, I-ECAP en ACR) op de geleverde AlMgSc legering om na te gaan hoe de grootte van de korrels kan verfijnd worden. Het initiële materiaal (“as

received") en de nieuw geproduceerde materialen na SPD werden gekarakteriseerd en hun eigenschappen werden vergeleken om de impact van SPD in kaart te brengen.

Een tweede doelstelling was een grondige karakterisering van het initiële materiaal omdat het zeer interessant is voor de industriële partners omwille van zijn buitengewone mechanische – en superplastische eigenschappen.

De derde doelstelling was het onderzoeken van de toepasbaarheid van het SPIF omvormingsproces voor al deze materialen en het opstellen van een analytisch model om de optredende krachten te voorspellen.

Een laatste doelstelling tenslotte was de ontwikkeling van een eindige elementen model voor SPIF dat toelaat om met korte rekentijd de optredende krachten en de finale vorm van het werkstuk nauwkeurig te berekenen.

3. Besluiten

De resultaten van dit onderzoek hebben aangetoond dat:

1. Het ARC proces veroorzaakt een sterke vervormingsversteviging maar geen korrelverfijning omdat de afschuifcomponent niet groot genoeg is.
2. Ondanks enkele persistente problemen met de monstergeometrie en met de manuele handelingen die vereist zijn bij de uitvoering van de vervorming, zijn we erin geslaagd om het I-ECAP proces toepasbaar te maken voor staven, platen en dunne plaat. Dit zier er veelbelovend uit omdat het proces een substantiële korrelverfijning in de AlMgSc legering genereert. Bovendien laat dit concept een reductie toe van de nodige krachten en is het toepasbaar op lange producten.
3. Het ECAP proces was uitvoerbaar op cilindrische monsters maar na zes vervormingspassen werd nog geen echt submicron materiaal bekomen, dit in tegenstelling tot de situatie in zuiver Aluminium. Een mogelijke verklaring voor dit verschil werd toegeschreven aan de aanwezigheid van nano-partikels.
4. Er werd aangetoond dat het SPIF proces uitgevoerd op het initiële materiaal mogelijk is tot een maximale inclinatie van de wand van 46°, wat overeenkomt met een lage vervormbaarheid. Er voor dit materiaal een analytisch model ontwikkeld om de optredende krachten te voorspellen alsook een veralgemeende formule toepasbaar op alle materialen.
5. Een grote verscheidenheid aan mechanische testen werd uitgevoerd op dunne platen van het geleverde materiaal op kamertemperatuur. Dit leverde heel wat informatie over het gedrag van dit materiaal op kamertemperatuur. Er werd een constitutieve vergelijking geselecteerd om het elasto-plastisch materiaalgedrag te beschrijven. Hiertoe werden de nodige materiaalconstanten bepaald.

6. Het “temperatuur – vervormingsnelheid” venster waarbinnen superplastisch gedrag optreedt, werd bepaald en een gepaste constitutieve vergelijking werd geselecteerd en de materiaalconstanten werden bepaald.
7. Een EE model werd aangepast om de simulatie van het SPIF proces mogelijk te maken. Het laat toe om met korte rekentijd de optredende krachten en de finale vorm van het werkstuk nauwkeurig te berekenen.

4. Bijdrage van het project in een context van wetenschappelijke ondersteuning aan transfer van kennis en innovatie

De karakterisering van het materiaal en de informatie betreffende het superplastisch gedrag zijn nuttig voor de leverancier van dit materiaal (Aleris) en voor de industriële partner die dit materiaal gebruikt (Sonaca).

Het onderzoek heeft toegelaten om de nieuwe SPD technieken te verbeteren, meerbepaald om enkele technische problemen op te lossen en om informatie over het materiaalgedrag na SPD te verzamelen. Het materiaal na SPD heeft op een aantal punten verbeterde eigenschappen en kan nuttig zijn in de luchtvaartsector omwille van zijn hogere sterkte.

Vermits er werd aangetoond dat het SPIF proces toepasbaar is op het geleverde materiaal en het feit dat er een formule werd ontwikkeld die de benodigde krachten kan inschatten, kan een oplossing voor de moeilijke omvormbaarheid van dit materiaal een stap dichter brengen, vooral omdat SPIF specifiek geschikt is voor kleine reeksen, zoals vaak voor vliegtuigonderdelen het geval is.

De verbetering van het numerische model dat de optredende krachten en de vorm van het werkstuk berekent, laat toe om in de toekomst het aantal uit te voeren experimenten gevoelig te verminderen.

5. Trefwoorden

Single Point Incremental Forming, Ultra fijne korrels, Incremental Equal Channel Angular Pressing, Materiaal parameter identificatie, Eindige Elementen simulatie, Aluminium legering AlMgSc.

Summary

1. Context

The aeronautic industry is constantly looking for ways to reduce the weight of aeronautic parts and structures. Therefore, the availability of a new material of the AlMgSc alloy family combining a low specific weight with high corrosion resistance, high toughness and excellent weldability is of major interest in this domain. This material choice was guided by an aeronautical industry: Sonaca.

The **S**evere **P**lastic **D**eformation (**SPD**) techniques such as (**I**ncremental) **E**qual-**C**hannel **A**ngular **P**ressing (**I-ECAP** and **ECAP**) and **A**symmetrical **C**old **R**olling (**ACR**) techniques applied on the selected alloy form a major opportunity to increase the strength.

High strength is however typically correlated with reduced formability. Such limitation can result in material failure when processing high strength materials with conventional forming methods.

Single **P**oint **I**ncremental **F**orming (**SPIF**) is an emerging flexible forming technique that is characterised by extremely high achievable strain levels compared to conventional forming methods. The process furthermore typically uses generic tooling only, offering the advantage of the elimination of tooling costs and providing short lead times. This process can be applied to conventional aeronautic materials.

The combination of a specific **Al**MgSc alloy choice, the SPD techniques such as I-**ECA**P, **ECA**P or ACR applied on it and the **SPIF** process within **ALECASPIF** project offers perspectives for the flexible construction of aeronautic components with significantly reduced weight. This combination offers valorisation potential in terms of reduced manufacturing costs due to significantly reduced tooling requirements and leads both time reductions, weight reduction of the components, which form a major life cycle cost advantage.

2. Objectives

The first objective of ALECASPIF project was to test the three SPD techniques (I-ECAP, ECAP and ACR) applied on the as received AlMgSc alloy to see how to generate the grain refinement. The initial and the new materials produced were characterised and compared together to see the impact of these techniques on their properties.

The second objective was to characterise the as received material as it is of considerable interest for the industrial partners for its superior mechanical and superplastic properties.

The third one was to check the SPIF applicability on all these materials and to develop an analytical force prediction model.

And the last objective was to develop the finite element modelling of the SPIF process to accurately predict, with a short computation time, the forming force and the final shape of a piece. This step is the first one required before the optimisation of the tool path to form a piece.

3. Conclusions

The results of this research bring following conclusions:

1. The ACR process induces a strong strain hardening but no actual grain refinement because the shearing component is not high enough for grain refinement.
2. Despite some problems of sample geometry and manual tasks, the I-ECAP process is adapted to bars, plates and sheets. It is very promising as it generates substantial refining in the grain structure of the AlMgSc alloy. Additionally, this tool design allows a feeding force reduction and can be applied on long pieces.
3. The ECAP process could be carried on cylindrical specimen but, after 6 passes, the samples have not yet reached the state of a submicron material. In opposition to pure Aluminium, it could be related to the presence of nano-size particles in this alloy.
4. The applicability of the SPIF process on as received sheets was demonstrated with a maximum cone wall angle of 46°, which is a low formability. An analytical force prediction model was developed on this material as well as a generalized formula adapted to any material.
5. A set of mechanical tests were performed on as received sheets and gave information about the material behaviour at ambient temperature. A constitutive law was chosen to describe its elastoplastic behaviour and its hardening and the material data were identified.
6. The superplastic domain (temperature and strain rate) has been localised, a material law was chosen and the parameters identified.
7. The FEM model has been adapted to simulate the SPIF process and to accurately predict the tool force and the shape with a short computation time for the as received material.

4. Contribution of the project in a context of scientific support to transfer of knowledge and innovation

The material characterisation and the superplasticity information are useful data for the material provider (Aleris) and for the industrial partner (Sonaca) using the material.

The project investigations help to improve the new SPD techniques: to solve technical problems and to have information about the transformed material. This new improved material can be useful for the aeronautic domain (higher strength than as received material).

The SPIF applicability on the as received material and its force prediction model are helpful information as this material is difficult to form and as the SPIF technique is adapted to small batch production as in the aeronautical parts.

The improvement of the numerical modelling of the SPIF process aimed to predict essential information (force and shape) about the SPIF process reducing the need of the experiments.

5. Keywords

Single Point Incremental forming, Ultra-fine grain, Incremental Equal Channel Angular pressing, Material Parameter Identification, Finite Element Simulation, Aluminium alloy AlMgSc.

Report

Acronyms and abbreviations

ACR:	Asymmetrical Cold Rolling
AR :	As Received AlMgSc hot rolled plate
CP:	Commercial Purity
CR:	Cold Rolling
DD:	Dual Drive rolling configuration
EBSD:	Electron Back Scatter Diffraction
ECAP:	Equal Channel Angular Pressing
EDX:	Energy Dispersive X-ray
FE:	Finite Element
FEM:	Finite Element Method
FLD:	Forming Limit Diagram
I-ECAP:	Incremental Equal Channel Angular Pressing
LVDT:	Linear Variable Differential Transformer
ND:	Normal Direction
RD:	Rolling Direction
SD:	Single Drive rolling configuration
SEM:	Scanning Electron Microscopy
SPD:	Severe Plastic Deformation
SPIF:	Single Point Incremental Forming
TD:	Transverse Direction
TEM:	Transmission Electron Microscopy
UFG:	Ultra-Fine Grain

Introduction

As the objectives were to test the three severe plastic deformation (SPD) techniques (I-ECAP, ECAP and ACR), to check the applicability of the SPIF process on the as received and the transformed materials, to characterise the materials and to model the SPIF process, it was obvious to gather the following five teams within this project:

- The University of Glasgow (US) for the I-ECAP process and its modelling,
- The University of Leuven (KUL, MTM department) for the ECAP process and microstructure analysis,
- The Centre for Research in Metallurgy (CRM) for the ACR technique and mechanical tests,
- The University of Leuven (KUL, PMA department) for the SPIF process and the force regression formula,
- The University of Liège (ULg) for the superplastic tests and the SPIF numerical model.

Figure 1 indicates the initial project flowchart that the teams tried to follow as well as possible.

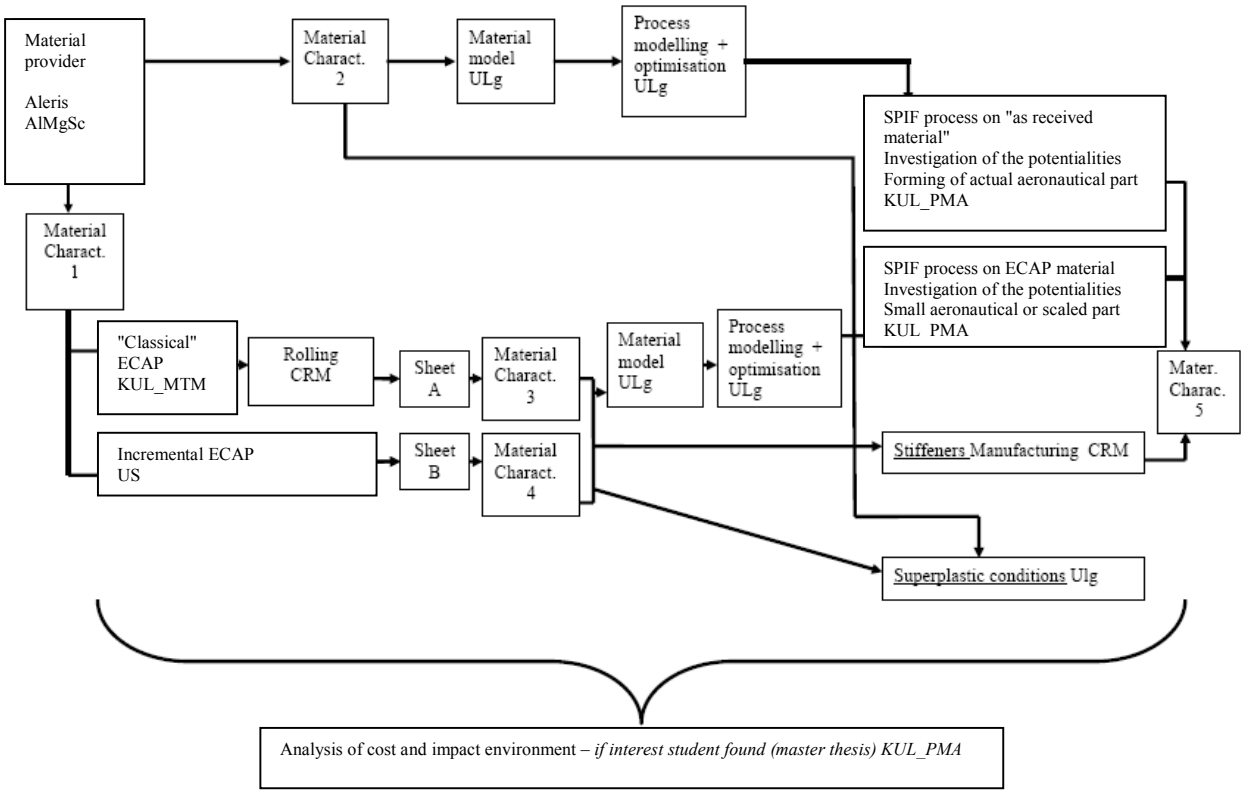

Figure 1: Project flowchart

Due to delay of material delivery and some experimental problems, we had to adapt this flowchart.

Indeed different SPD processes were tested to reach grain refinement: I-ECAP, ECAP and ACR and to obtain the desired sheet shape (cold rolling process).

Many mechanical tests and microstructure analysis were performed on the as received sheets and on all the transformed material to compare their properties before and after SPD transformation. The interest of each SPD process was defined. These tests provided the required data to describe the superplastic behaviour and to identify the material constitutive laws allowing the modelling of the material behaviour.

Thus, the forming processes were compared.

The SPIF forming process gave information to define the forming limit and to establish a regression formula.

And finally, the numerical model was improved and the SPIF process was simulated.

Processes description

1. *Cold rolling*

Conventional cold rolling

The conventional cold rolling is performed under symmetrical conditions: the roll diameters are equal (Figure 1.1), there is no use of lubrication to avoid any asymmetric effects and the same motor drives both rolls. The stand is mounted in duo configuration.

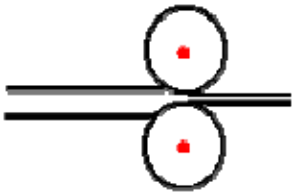

Figure 1.1: Performed conventional cold rolling (roll diameter 396 mm)

Asymmetric cold rolling

Asymmetrical rolling is a conventional rolling where 2 different roll diameters or 2 different roll speeds are used.

Several combinations of work rolls are usually performed on the CRM pilot line in combination with disconnecting the upper shaft to make the bottom roll the only driven roll. The following figure gives an overview of the different line-ups of the CRM stand.

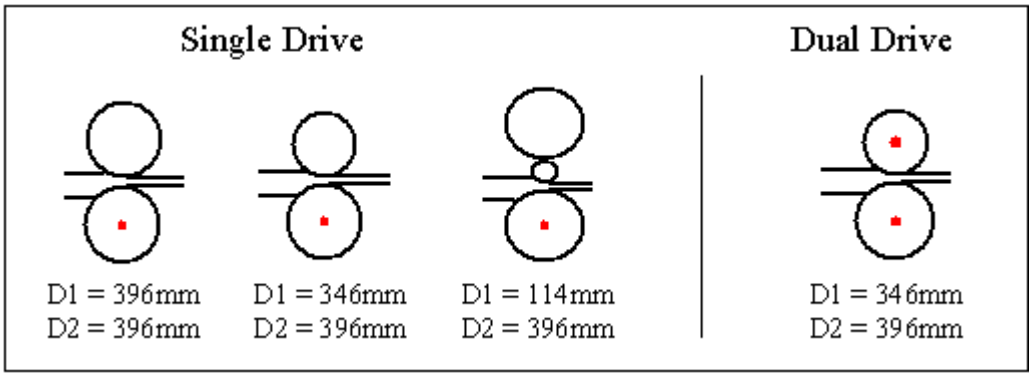

Figure 1.2: Performed asymmetrical cold rolling configurations

The performed asymmetrical configurations performed were as follows:

1- Different diameters, disconnected upper roll with backup roll (single drive (SD) configuration)

This trial is a combination of the quarto and duo configuration of the rolling mill. The upper half is placed in quarto configuration: a small work roll (114 mm) with a backup roll whilst the lower half is one driven work roll but with a bigger diameter (396 mm).

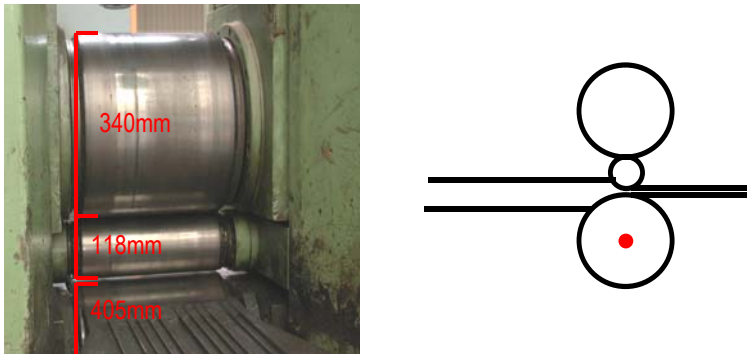

Figure 1.3: Line-up for the single drive, different diameters with backup roll - trial

In this configuration a huge difference in work roll diameter is obtained. The big work roll is more than three times as big as the small one.

2- Different diameters in dual drive configuration (DD)

For this kind of trials the difference in diameter can't be too high as this would lead to problems with the reduction unit of the drive. The diameters of the rolls that are used are 346 mm for the top roll and 396 mm for the bottom roll. This makes a difference of ±12%. The line-up is shown in the following image:

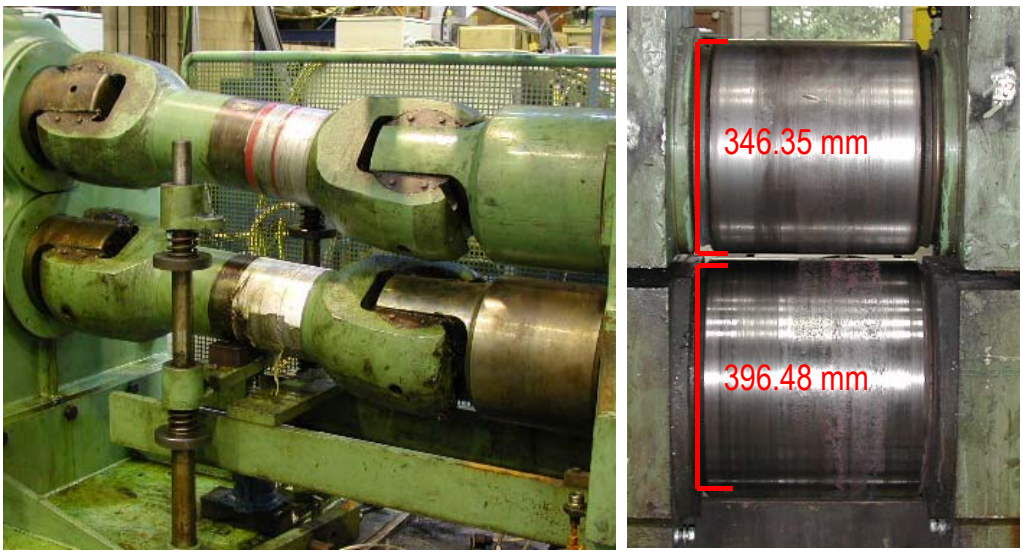

Figure 1.4: Line-up for the twin drive, different diameters

Since both rolls are driven, their rotation speed (rpm) is equal. If not the gearbox would have a break down. This means that the speed difference between top and bottom roll is also ±12% ($v = \omega \cdot R$).

2. *I-ECAP process*

Introduction

The most popular SPD method is equal channel angular pressing (ECAP) [1]. In this process, a round or square billet is forced through a sharply bent channel. Since the cross-section of the channel does not change, plastic deformation occurs only at the channel bend; the mode of deformation is close to simple shear as illustrated in Figure 2.1 by a unit square changing its shape into a parallelepiped. However, the length of the leading channel limits the length of the billet processed to about 6 lateral dimensions. It must not be too long to avoid an excessive force caused by friction and the associated tool design problems. The short length, together with end effects, causes poor utilisation of the material, often not exceeding 50% [2]. To address some of the above problems, a new SPD process, called incremental ECAP (I-ECAP), was proposed [3-4]. I-ECAP is suitable for processing bars, plates and sheets. Initially, it was tried for bars [5] and plates [6]. In this project, bars were processed first but the main emphasis was put on processing sheets.

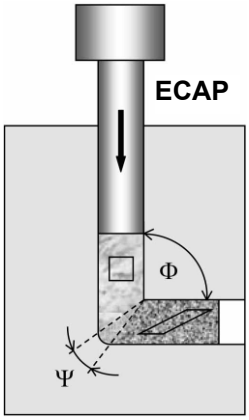

Fig. 2.1: Schematics of ECAP

Principle of Incremental ECAP

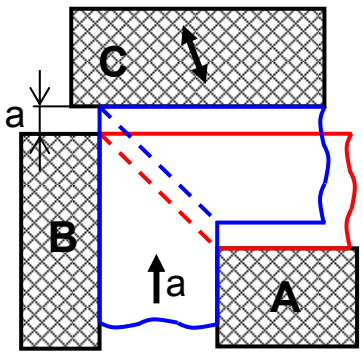

Fig. 2.2: Idea of I-ECAP

In the basic version of I-ECAP, dies A and B define the input channel while die A and punch C, the output channel of the device (Figure 2.2). Punch C moves in a reciprocating manner at an appropriate angle to the billet. Feeding of the billet takes place during withdrawal of the punch when there is no contact between billet and punch. When the billet stops and becomes fixed in position, the punch approaches it and deforms plastically in a “dashed” zone. The mode of deformation is that of simple shear and, provided the feeding stroke "a" is not excessive, consecutive shear zones overlap resulting in a uniform strain distribution along the billet. Separation of the feeding and deformation steps reduces or eliminates friction during feeding; this enables processing very long/infinite billets.

Device for I-ECAP of bars

To realise the I-ECAP process on a standard, vertical press, it is recommended that two billets in the mirror configuration are processed simultaneously in order to avoid a lateral force (Figure 2.3). Such configuration, for 10×10 mm cross-section billets, was tried as described in [5]; two billets were put together, incrementally fed through a vertical rectangular channel and deformed by a reciprocating punch. The face of the punch was shaped with a central spike to help direct billets into the horizontal channel.

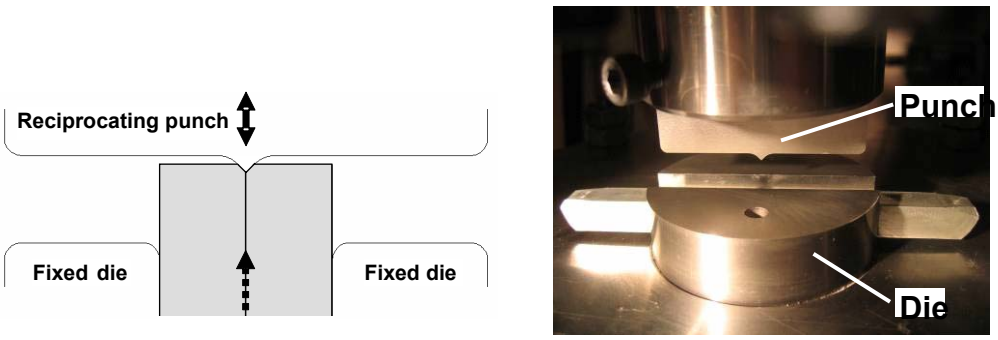

Figure 2.3: I-CAP of two bars

The same tool configuration was used in the current project for processing 10×10 cross-section billets, however, a few changes were also introduced. The first change was moving the process from 250 kN press to a larger 1000 kN press. It was a laboratory press equipped with a hydraulic servo actuator. A sine wave signal, produced by a waveform generator and monitored using an oscilloscope, was fed into the press control module to cause a reciprocating movement of the punch. The press was equipped with a strain gauge load cell to measure punch force and an LVDT transducer to monitor punch movement.

The second change was related to the fact that, under the new press table, there was enough room for a 200 kN self-locking screw jack to be placed and serve as billets' feeder (Figure 2.4).

This required a thick plate to be fixed to the press to provide support for a screw jack. The screw jack was driven manually by turning a system of shafts connected by two gear boxes; their gear ratios, together with that of screw jack, resulted in one turn of the input shaft moving the screw by approximately 0.2 mm.

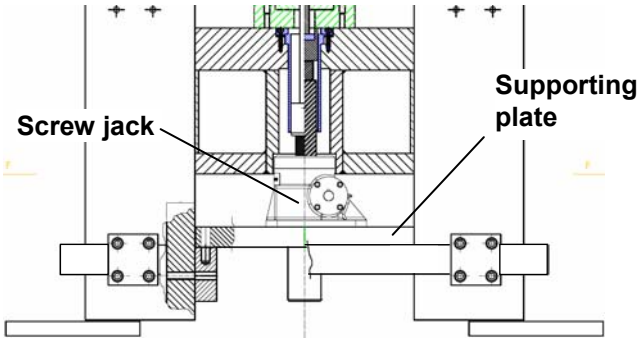

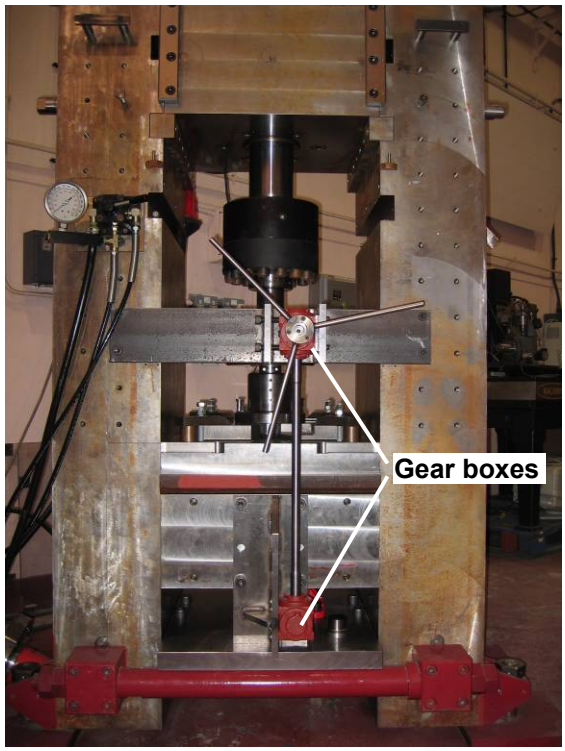

Figure 2.4: Feeding system (screw jack) on 1000 kN hydraulic servo press

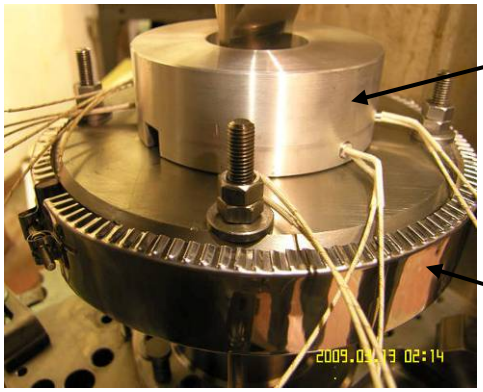

Figure 2.5: Heating elements for I-ECAP of bars

The third change was introduced to enable processing of less ductile materials by increasing their temperature; this was achieved by incorporating a die heating system. It consisted of a 3 kW ceramic band heater mounted around the die prestressing ring and two aluminium heating blocks put on top of the ring, each one equipped with three 0.5 kW heating cartridges (Figure 2.5). The location of heaters followed the idea of heating the tools near the deformation zone rather than along the whole feeding channel. Tool temperature was measured with a 0.5 mm diameter thermocouple inserted in a hole near the deformation zone. A PID temperature control system was designed and built to enable keeping the tool temperature constant during the process.

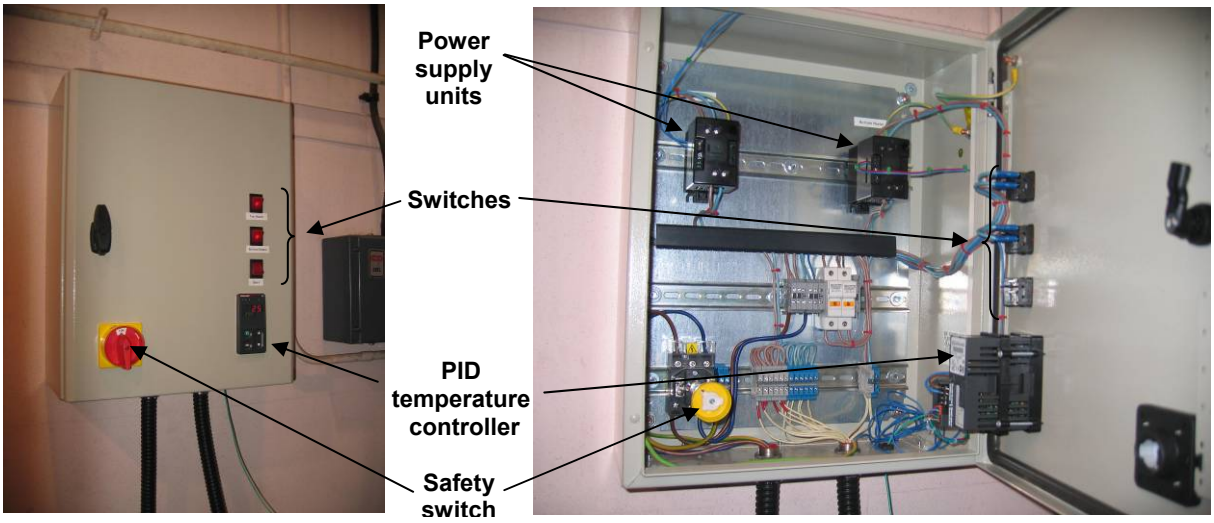

Figure 2.6: Temperature control system

Device for I-ECAP of sheets

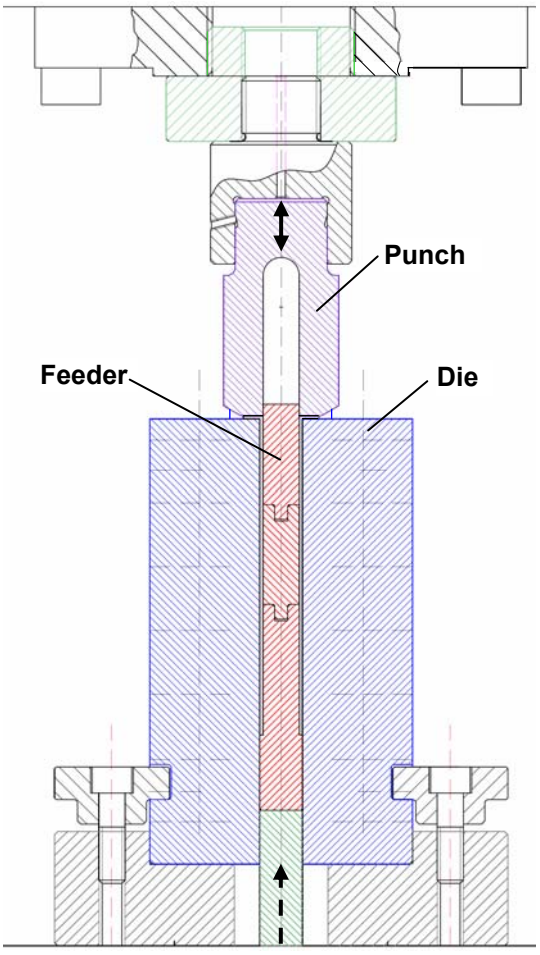

When instead of bars, sheet metal strips with 2×50 mm cross-section were to be processed, an entirely new tool set had to be designed, built and tested (Figure 2.7). It was decided to separate sheet strips with an additional tool to avoid using a blade-thin feeder. The proposed tool served three functions. The bottom part of the tool had a step on each side, which enabled feeding the strips upwards and prevented their backward movement; this justified calling it a feeder. It also played the role of a movable die, which travelled together with the sheet material and, therefore, did not introduce friction. Finally, it was guiding the punch by entering a gap in the punch. Since the gap had a limited length (as the punch itself), the feeder was divided into three segments, of which top two were pushed out as soon as they appeared above the die. Each face of the punch had a half-spike to improve the material flow. The die concept was changed.

The die was divided into four segments, which however, were not prestressed with a ring like it was the case with I-ECAP of bars. Instead they were kept together by the dowel pins and bolts. Some of these segments were taller to provide walls for the horizontal channel (to secure plain strain condition) and guide the punch in the direction perpendicular to that constrained by the feeder. All highly stressed tools were made of high speed steel, Vanadis 23, hardened to 60 HRC.

Figure 2.7: Tool design for I-ECAP of sheets

The die heating system had similar but less powerful heating elements (Figure 2.8). It consisted of a 1.5 kW ceramic band heater mounted around the die, near its top, and two aluminium heating blocks put on top of the die, each one equipped with a 0.25 kW heating cartridge. Since the press displacement transducer was inside the hydraulic actuator, far from the deformation zone, it was not used to set the thickness of the processed strip. Instead, another LVDT traducer was attached to the punch holder, with its rod going through the heating block and resting on the upper die surface.

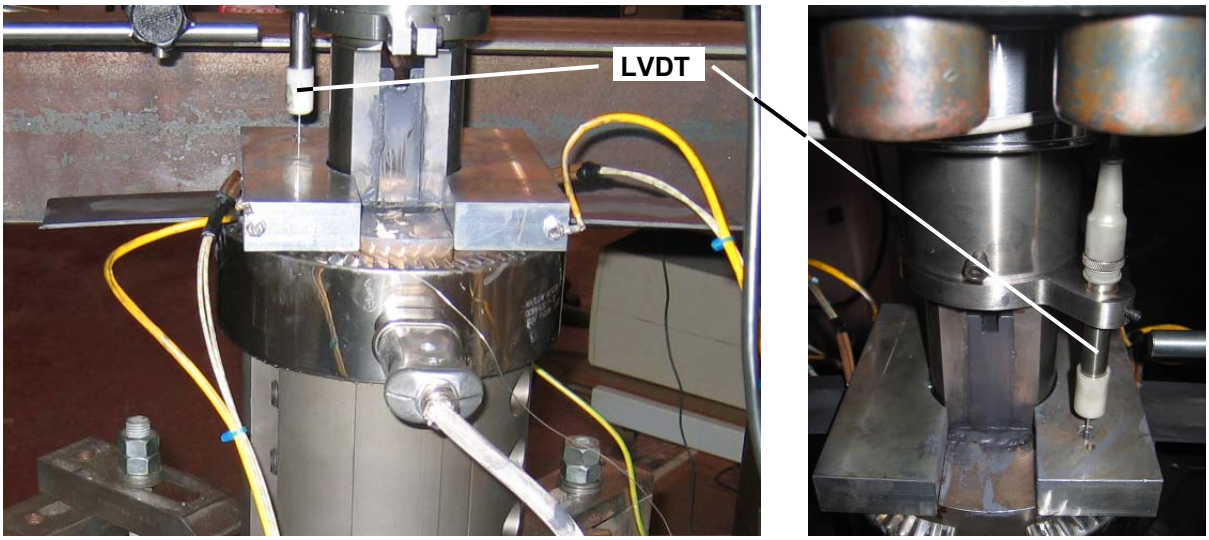

Figure 2.8: Heating elements for I-ECAP of sheets and LVDT

Further development of I-ECAP

Further development of I-ECAP requires, among other things, automation of feeding and better control of material thickness. These have been advanced in the project, however, not finished. A motor driven system of material feeding was designed based on the existing screw jack and a brushless AC servomotor (with controller) and a gear head attached to the input shaft of the screw jack (Figure 2.9). Also, a new LVDT, capable of working at elevated temperature, up to 220°C, was getting ready to be installed.

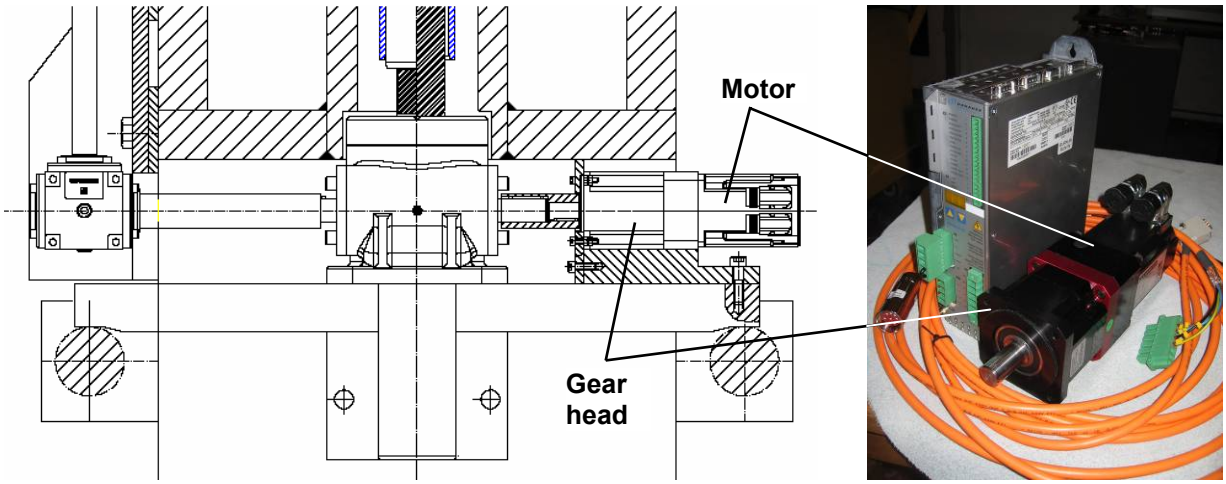

Figure 2.9: Concept of attaching electric motor to screw jack

FE simulation

FE simulation using Abaqus program was a routine part of the process and rig development. For example, the new split die design was initially tested by deflection analysis of bolted die segments (Figure 2.10). Deflection of the screw jack supporting plate was also checked in this way (Figure 2.11). The punch (spike) geometry was established by simulating material flow in I-ECAP and choosing the case with most uniform strain distribution (Figure 2.12).

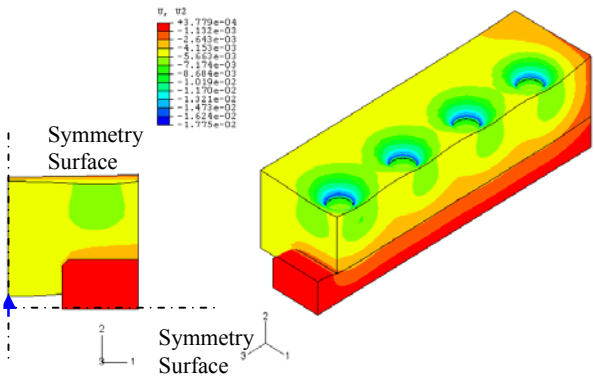

Figure 2.10: Deflection of die due to bolt tightening

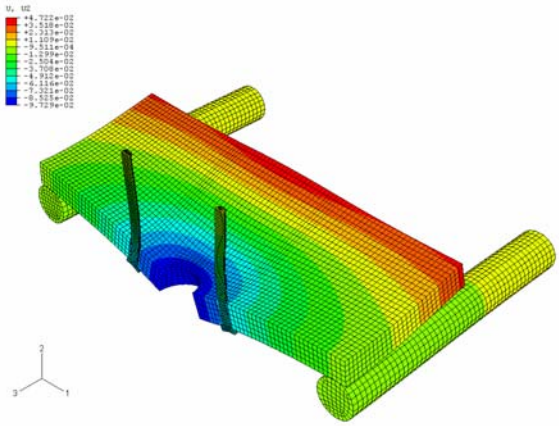

Figure 2.11: Deflection of screw jack supporting plate

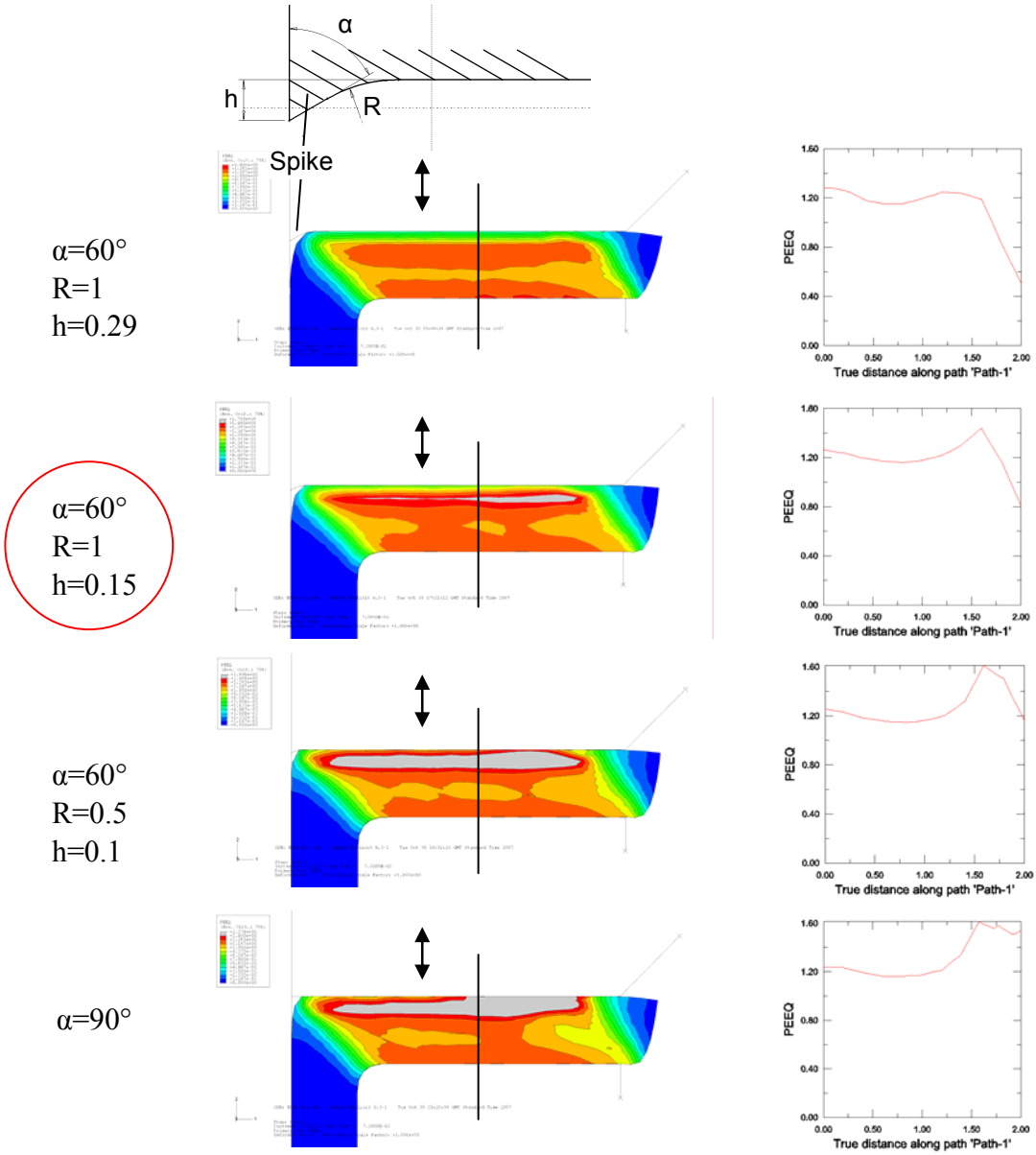

Figure 2.12: FE simulation of material flow during I-ECAP to identify optimum spike geometry

Lubrication

Aluminium alloys have tendency to stick to metal forming tools. This leads to the material pick up by the tools, increased friction and poor surface finish of the processed material. Molybdenum disulfide, MoS_2, is a popular lubricant often used for cold and warm (up to 400°C) SPD processes. However, an attempt to use just MoS_2 as lubricant did not produce good results in the current project; the process force was substantially increased and the aluminium material, which fused to the die, had to be dissolved by warm etching with NaOH. Thus to prevent the material pick up, a conversion coating of calcium aluminate was formed on aluminium billets,

followed by lubrication with soap and MoS_2. The coating process and lubrication with soap were carried out by Dr Lech Olejnik from Warsaw University of Technology. The process involved several operations as illustrated in Figure 2.13. It was essential that the billet surface was completely clean. This required careful degreasing and pickling before coating. Eventually, in order to simplify the lubrication procedure, lubrication with soap was abandoned after checking that the conversion layer and MoS_2 alone give better results.

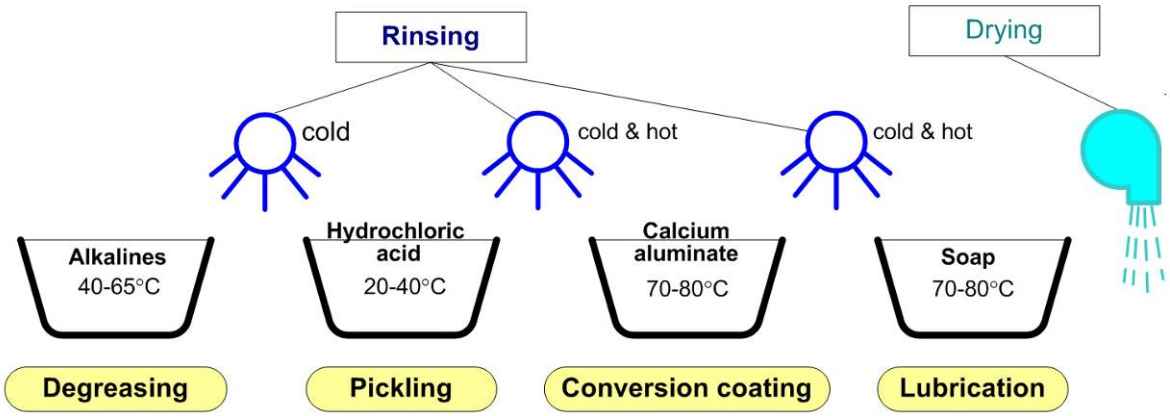

Figure 2.13: Procedure of conversion coating and lubricating with soap

Processing

The above paragraphs help understand the steps involved in I-ECAP. For the case of processing the sheet strips, these steps were as follows. The die was preheated to 200°C; the punch was initially resting on the die so it was also preheated (to the unknown temperature). The two conversion coated strips were lubricated with MoS_2 using a brush and inserted into the die channels, where they were heated by conduction. Finally, the reciprocating movement of the punch was initiated, with the bottom position slightly less than 2 mm above the die surface. Its peak-to-peak amplitude was approximately 2 mm and frequency 0.5 Hz. Such low frequency was required to allow manual synchronisation of the feeding movement. For the same reason, the amplitude of 2 mm was much higher than the feeding increment of 0.2 mm. Due to low frequency and small feeding increment, the whole process took about 30 minutes. During that time, the die temperature was held constant at 200±2°C. The process was stopped when the feeder reached the die surface. After punch withdrawal, the feeder was used as an ejector, which allowed the strips to be removed manually. After that, the strips were cleaned (traces of flash removed), straightened using three point bending and machined to fit the die again.

SPD usually requires repetition of the process in order to accumulate very large plastic deformation. The amount of plastic deformation generated in one pass of ECAP or I-ECAP is about 1.15. In the current project, the process was repeated 6 times to improve the chance for substantial grain refinement, with grains featuring high-angle grain boundaries. It is also customary that the billet is rotated about its axis before each pass. In the case of square cross section bars, the angle of rotation was 90° (so-called route B_C). In the case of sheet strips that type of rotation was impossible so, instead, a 180° rotation was used (route C). In any case, this required feeding the processed material again into the same die. This, in turn, required some machining of the processed billets to enable their insertion into the die channel.

There were three reasons for that: springback, flash and shape errors. Springback in the direction of punch movement was dealt with by reducing the thickness of the material in the output channel. For example, instead of 2 mm thick sheet, a 1.9 mm thick sheet was produced by lowering the bottom dead end of the punch; this enabled easy insertion of the sheet in the 2 mm thick input channel. The same was not possible in the perpendicular direction because the width of the channel was fixed and equal to the nominal width of the material, either 10 mm for bars or 50 mm for sheets. Therefore, some machining was used to reduce the width of the material before next pass. While this could be resolved in the future generation of tooling by changing the geometry of the channel, flash and shape errors would have to be dealt with any way. The flash created in I-ECAP was small but nevertheless had to be removed manually by sanding with sand paper. This alone would remove conversion coating on the bar/sheet edges and destroy any chance of avoiding the repetition of coating procedure. There was some bending in the direction of moving punch, which was removed by straightening of bars/sheets using 3-point bending at room temperature (Figure 2.14). Sometimes, bending in the direction perpendicular to that of moving punch was also observed. In the case of bars, it was easily removed by 3-point bending. However, in the case of sheets, bending in the sheet plane was more problematic. If it was caused by non-uniform thickness of the sheet along its width, the remedy might be additional rolling. It was tried a few times before conversion coating (at

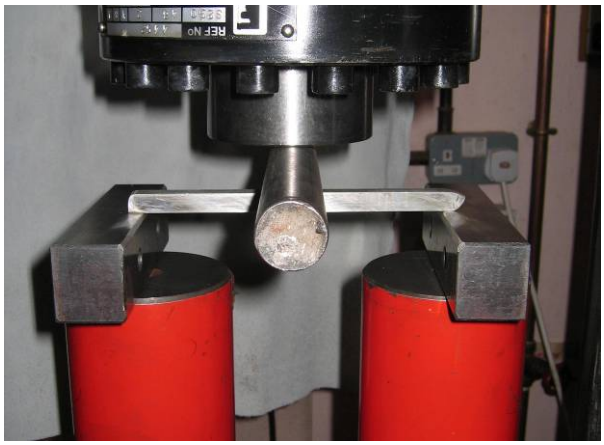

Figure 2.14: Straightening of bars using 3- point bending

Warsaw University of Technology), but it was difficult to control and also caused some bending typical for rolling. If the cause of bending was different friction conditions along both edges of the strip, the only option was to machine off the edges. All the above factors resulted in some loss of the material, which led to shortening of bars/sheets from the initial 190 mm to approximately 150 mm after 6 passes.

3. ECAP process

Equipment

Several techniques to obtain submicron or nano-size grains are now available, e.g. high-energy ball milling, vapor deposition, fast solidification and severe plastic deformation (SPD). The last technique relies upon the natural development of a substructure during deformation. After small to moderate deformation, most metallic materials contain cells or subgrains, usually with sizes in the submicron range, but separated by low angle boundaries (in the range 1 – 10°). During large deformation (ε>3), preferentially with various changes in strain path, the former cells or subgrains will developed high angle boundaries and can be considered as a "submicron grained material".

Probably the oldest, and certainly the most popular SPD technique at the moment, is "Equal Channel Angular Extrusion" (ECAE), also known as "Equal Channel Angular Pressing" (ECAP). A billet of the test material is pressed through a die consisting of two channels with identical cross sections, intersecting at an angle $30° < \phi < 120°$, with ϕ often equal to 90° (see Figure 3.1). The deformation occurs by simple shear parallel to the intersecting plane of the channels. The equivalent strain per pass is given by: $\varepsilon_{eq} = 2/\sqrt{3}[\cot(\phi/2)]$. For $\phi = 90°$, $\varepsilon_{eq} = 1.155$.

Because the channels have an identical cross section, the dimensions of the billet remain unchanged, and the process can, in principle, be repeated any number of times. If the cross section has a 4-fold symmetry axis, the sample can be rotated by 90° or 180° about the extrusion direction (ED) before reinsertion in the die. Based on the regular repetition of such a rotation φ around ED, four commonly applied routes have been defined. For route A, φ is 0° (no rotation), for route C it is 180°, for route BC it is 90°, and for route BA φ is alternatively + 90° and – 90°. In general one can say that ECAP yields grain sizes of 300 – 1000 nm in most metals.

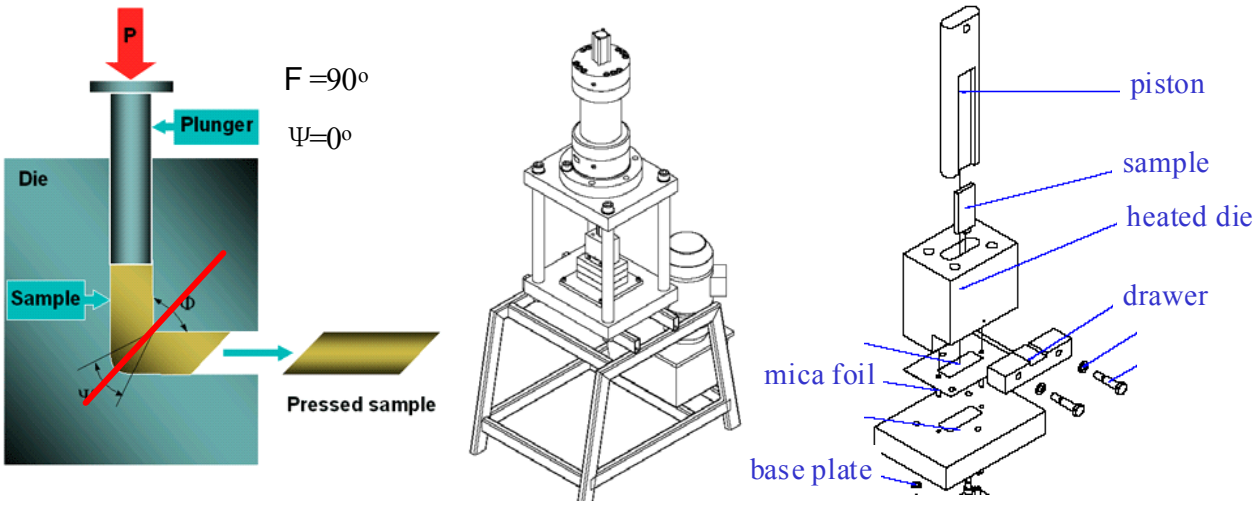

Figure 3.1: Schematic of an ECAP press with (left) a cross section of a die with cylindrical samples and (right) a scheme of a die for rectangular samples

In the present project, part of the test have been carried out with cylindrical samples (cfr. Figure 3.1, left). The initial samples were 60 mm long and had a diameter of 11.9 mm. The die has an angle ϕ = 90° and a maximum pressing force of 110 kN. ECAP tests can be carried out from room temperature up to 400°C. The usual pressing speed is between 1 and 10 mm/min and MoS_2 is used as lubricant.

Since rectangular shaped specimens were needed for further rolling at CRM, a new ECAP press and an ECAP die have been designed (Figure 3.1, centre and right). Nearly all parts of the ECAP press have been selected and bought -mainly financed by another project- and assembled at MTM. The various parts of the ECAP die have been designed in MTM and fabricated in the MTM workshop. The new press can exert a pressure force of 250 kN and can produce samples of 7x35x70 mm^3. The die itself is made of Inconel and can be used at working temperatures between RT and 400°C. The punch envelops the sample on three sides to minimize friction.

Samples shape & size

Figure 3.2 shows a cylindrical and a rectangular sample after several ECAP passes. The production of cylindrical samples goes rather smooth, but unfortunately these samples are not suitable for further processing (rolling and SPIF) because the shape is not good and the volume is too small to yield a sheet that can be clamped in the SPIF device. For this reason the die producing rectangular samples has been designed. A lot of technical problems with this die have occurred during the project and the amount of “usable” samples that have been obtained is extremely small. Very often the die gets stuck because material penetrates in the small fissures between die and punch. Several modifications of the die have been carried out, but the

problem is not completely solved. An inherent problem is that material from head and tail of the samples bend over (see pattern of material flow in Figure 3.3), leaving marks on the surface. This was always the case using route A and less when using route C. These marks will yield cracks during rolling. For this reason part of the sample must be cut before rolling and the remaining material is not enough to get a plate suitable for SPIF.

Figure 3.2: Cylindrical and rectangular ECAP sample after several ECAP passes

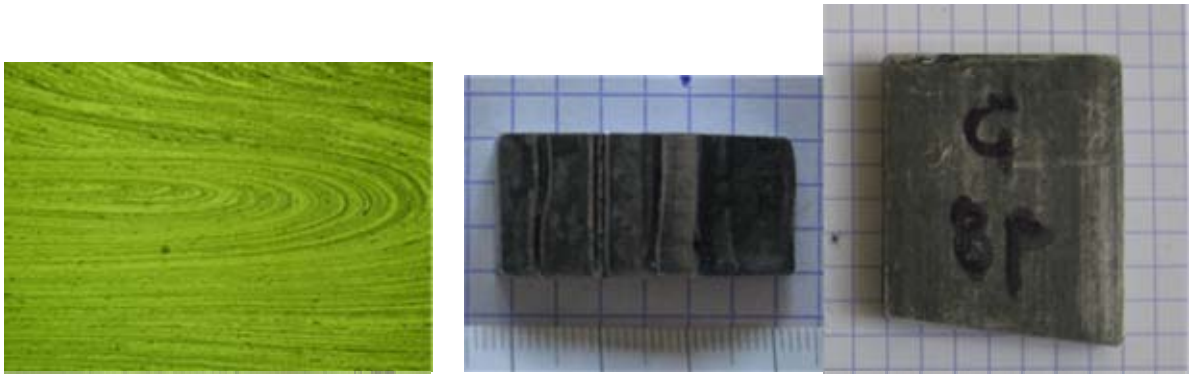

Figure 3.3: Material flow at the tail of a rectangular sample (left) and resulting surface marking (center); the "usable part" of the sample (right) is about 35 mm x 40 mm

4. SPIF process

Single Point Incremental Forming (SPIF) is a dieless sheet forming process that can produce complex parts using a spherically tipped tool to locally deform a sheet blank along a programmed toolpath.

As illustrated in Figure 4.1, a firmly clamped sheet is formed by a contouring operation of the forming tool. The tool moves along a predetermined contour in the horizontal plane, after which the tool incrementally descends and starts a contour in the next horizontal plane. Building up the workpiece layer by layer. A different possible toolpath strategy is a constant spiralling path.

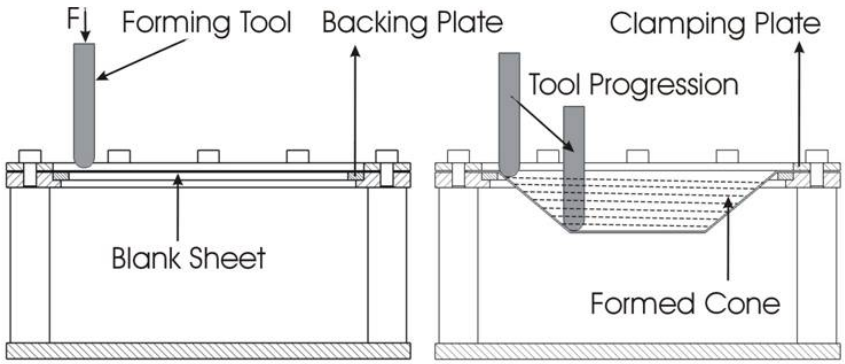

Figure 4.1: Description of SPIF process

Due to the nature of the process large setup and tooling costs are avoided and conventional 3 axis numerically controlled systems can be used to form most shapes. The redundancy of dies in SPIF makes the process very flexible and capable to incorporate design changes and part modifications. This allows for rapid prototyping of sheet metal parts.

The platforms (Figure 4.2) used in the framework of this project were: a 6 axis robot and a 3 axis rigid milling machine, both equipped with a dedicated force measuring device.

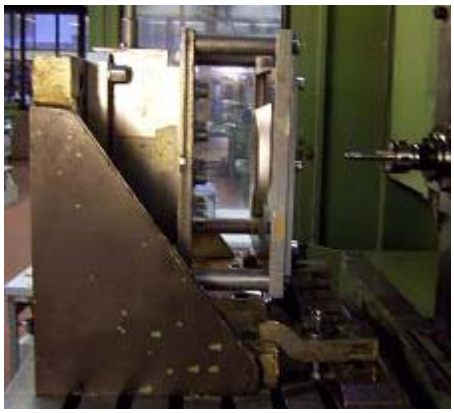

Figure 4.2: Platform description

The forming speed (approx. 2000 mm/min) in combination with the long toolpath results in a slow forming process, which limits SPIF to small batch production.

Thinning of the workpiece is the dominant failure mode in SPIF and is related to a workpiece drawing angle α (Figure 4.3). For a given material and thickness a maximum drawing angle can be determined which represents the limits of the conventional incremental forming process.

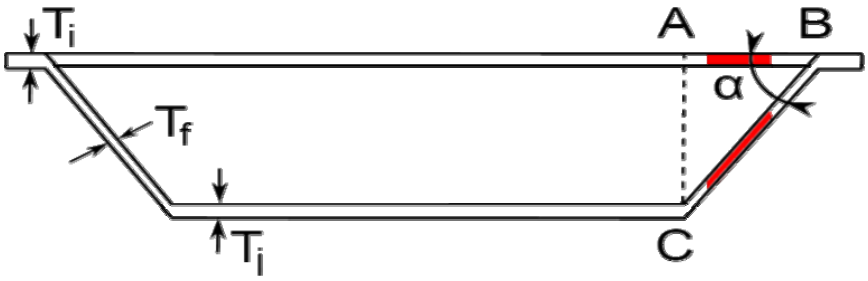

Figure 4.3: Workpiece geometry

The SPIF process is known to shift Forming Limit Diagrams (FLD) to higher formability in comparison to conventional forming processes. This is especially of interest for materials with a reduced formability such as UFG material. This makes it an interesting technique to apply on the material explored within this project.

Preliminary tests on other materials

Writing the project, we knew that the ECAP Al-Mg-Sc alloy would not be available from the beginning but we thought the team KUL-PMA could already work on AR Al-Mg-Sc alloy. As it was not the case, after discussion with SONACA, it was decided that SPIF process would be first investigated on AA2024T3. This material could be provided quickly by SONACA. It has similar material properties as Al-Mg-Sc alloy and is of technological interest for aeronautical industry. The tests performed by KUL-PMA on AA2024T3 have brought new knowledge and allowed checking a methodology for a quick identification of the SPIF forming limits. SPIF processed specimens were produced large enough for material characterisation. Approaches to extend the SPIF forming limits by laser heating or by applying multi-step SPIF process were investigated. The forming forces during SPIF process were measured and regression formulas established. The obtained results for forces of AA2024T3 make it clear that the 3 mm sheet of Al-Mg-Sc cannot be formed by the SPIF machines available in KUL-PMA. As soon as Al-Mg-Sc 3 mm sheets were available, CRM produced cold rolled and annealed small specimens of 1 and 0,5 mm thick with similar properties as the AR 3 mm sheet. A larger quantity of 1 and 0,5 mm thick Al-Mg-Sc sheets, suitable for SPIF experiments, was the result of this rolling. These sheets were delivered in the second half of 2008 by CRM. Experience gained during the tests on AA2024 T3 proved useful and made characterizing Al-Mg-Sc for SPIF go fast and flawless. The tests performed on Al-Mg-Sc are similar to those done on AA2024T3. The SPIF forming limit of this material was determined. Also a factorial analysis was performed on the Al-Mg-Sc sheets. This factorial analysis provides a set of regression formulas to predict the forming forces in processing of Al-Mg-Sc.

AlMgSc characterisation

To facilitate the understanding of this report, the following flowchart (Figure A.0) describes the different shapes of AlMgSc material delivered by the provider: Aleris, the SPD techniques and the forming processes applied.

The same numbering used for this figure and for the next paragraphs should help the reader to understand which sample is characterised.

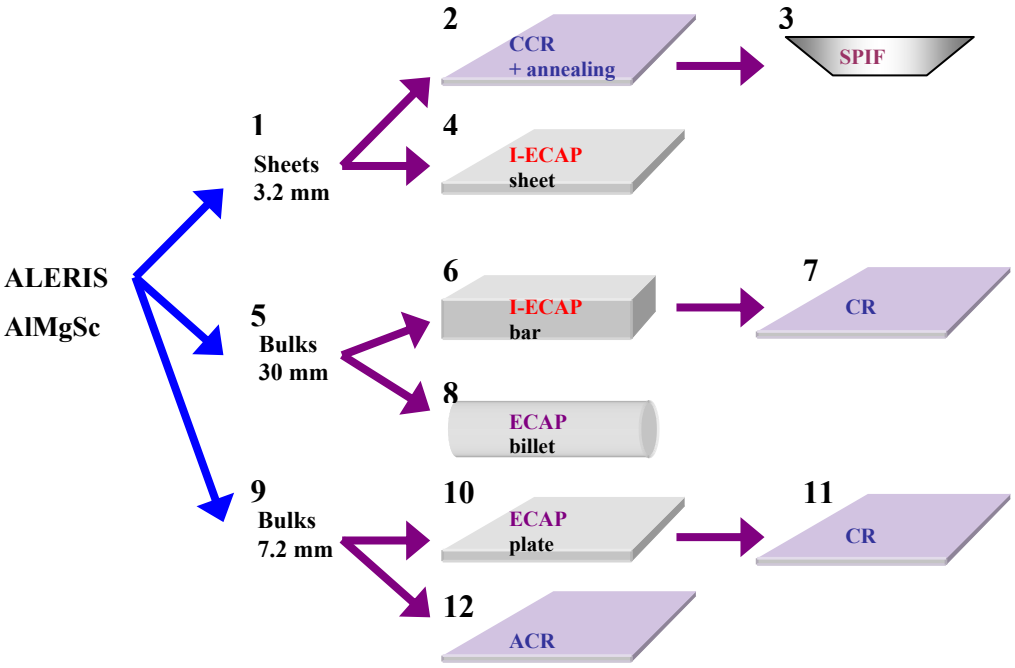

Figure A.0: Material transformation

The states 1, 5 and 9 in Figure A.0 represent the material provided by Aleris.

The sheets A in Figure 1 (see "Introduction") correspond to state 11 and the sheets B correspond to states 4 and 7.

1. As Received sheets (3.2 mm)

Simple tensile tests

To investigate the anisotropy of the material, tensile tests on A50 specimen of AR material at 0°, 45° and 90° from the rolling direction were performed. The results are given in Figure A.1.1 and in Table A.1.1.

For all the tests described, the formulations of true stress: $\sigma_{true} = \frac{F_i}{A_i}$, true strain: $\varepsilon_{true} = Ln\frac{L_i}{L_0}$ are used, even when it is not specified except for Re, Rm in Tables A.1.1 and A.1.2 where the engineering stress: $\sigma_{eng} = \frac{F_i}{A_0}$ is used.

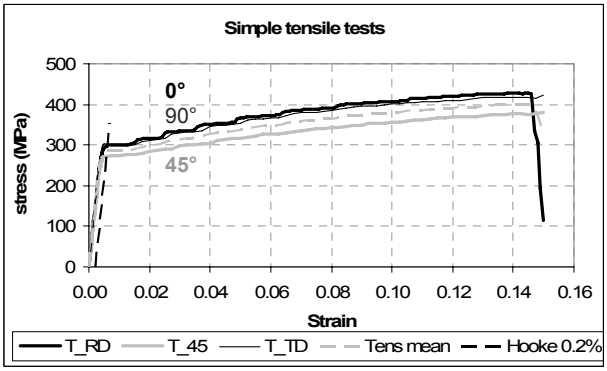

Figure A.1.1: Effect of anisotropy on tensile tests

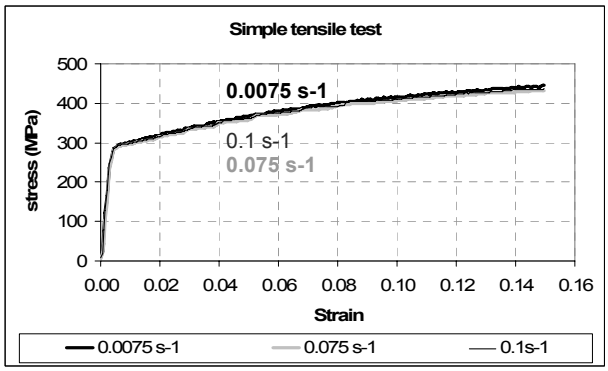

Figure A.1.2: Effect of strain rate on tensile tests

Orient.		E	Re 0,2	Rm	Eu	Etot
		GPa	MPa	MPa	%	%
0°	Mean value	**78.3**	**297.3**	**376.3**	**13.0**	**15.3**
	Std. Dev	2.3	0.6	0.6	1.9	0.4
45°	Mean value	**74.0**	**275.7**	**332.0**	**14.4**	**18.7**
	Std. Dev	5.3	1.5	1.0	1.1	4.0
90°	Mean value	**84.3**	**296.3**	**367.7**	**12.6**	**17.3**
	Std. Dev	2.1	1.5	1.2	0.8	1.4

Table A.1.1: Tensile properties at 0°, 45° and 90° from the rolling direction

Strain rate		E	Re 0,2	Rm	Eu	Etot
1/s		GPa	MPa	MPa	%	%
0.075	Mean Value	88.7	287.3	377.0	15.9	20.4
	Std. Dev	2.1	1.5	2.0	2.2	1.1
0.0075	Mean Value	87.3	289.3	385.3	14.8	16.6
	Std. Dev	8.0	1.5	1.5	0.9	0.9
0.1	Mean Value	94.5	288.5	378.5	14.5	20.7
	Std. Dev	3.5	3.5	2.1	0.1	0.8

Table A.1.2: Tensile properties in rolling direction for different strain rates

A decrease of Yield Stress and Tensile Strength at 45° from the rolling direction is observed. This leads to a light increase of E_u and E_{tot} without any significant change on the strain hardening coefficient n.

Tensile tests were additionally performed in rolling direction (0°) with 3 different strain rates. The results are displayed in Figure A.1.2 and in Table A.1.2. No significant change in the mechanical properties is observed with increasing the strain rate.

The Lankford coefficients: r_0, r_{45} and r_{90} with $r_\alpha = \frac{\varepsilon_{p22}}{\varepsilon_{p33}}$ are classically computed from tensile tests and used to define the parameters F, G, H and N of the Hill yield locus. α is the angle between the longitudinal direction of the test specimen with the rolling direction, ε_{p22} and ε_{p33} are the plastic strain respectively in the transversal and thickness directions.

Due to Portevin-Le Chatelier effect (serrated stress-strain curve as seen in Figure A.1.1, a kind of instability classically observed in AlMg alloys), it was neither possible to define the Poisson ratio, nor the Lankford coefficient at 45° and at 90° from RD.

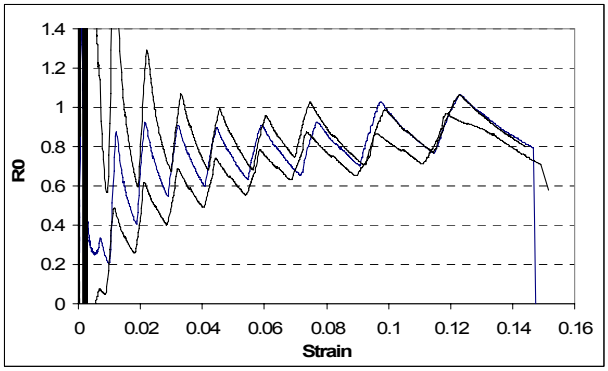

Figure A.1.3: Lankford coefficient in RD direction

The average R_0 coefficient, computed point by point in RD direction (Figure A.1.3) could be estimated by 0.814.

Shear tests, large tensile tests, orthogonal tests and Bauschinger tests

Additional tests, classically used to describe the yield locus shape and to fit the material data of the isotropic and the kinematic hardening have been performed: a monotonic shear test (Figures A.1.4.a and A.1.5), a large tensile test (Figures A.1.4.b and A.1.6), two orthogonal tests (tensile test followed by shear test) at two levels of pre-strain: 4% and 8% (Figures A.1.4.c and A.1.7) and two Bauschinger shear tests (shear test followed by a reverse shear test) at two different levels of pre-strain: Gamma = d/b = 8.8% and 29% (Figures A.1.4.d and A.1.8).

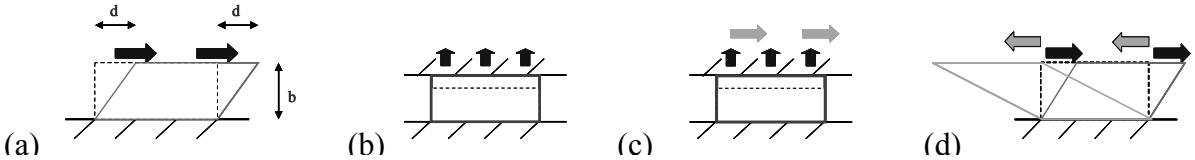

Figure A.1.4: Description of the tests: (a) shear test, (b) large tensile test, (c) orthogonal test and (d) Bauschinger test

The tests were performed three times and showed a good reproducibility, thus an average curve is provided for each loading state.

The tensile, shear and large tensile tests were performed in three directions: at 0° (RD), 45° and 90° (TD) from the rolling direction to see the effect of anisotropy. It is observed that the material is not isotropic. As already observed by simple tensile tests, the behaviour is almost the same in RD and in TD but is different at 45° from RD.

An average curve has been computed for the tensile tests, the shear tests and the large tensile tests as it is indicated in Figures A.1.1, A.1.5 & A.1.6 to characterise the equivalent global behaviour.

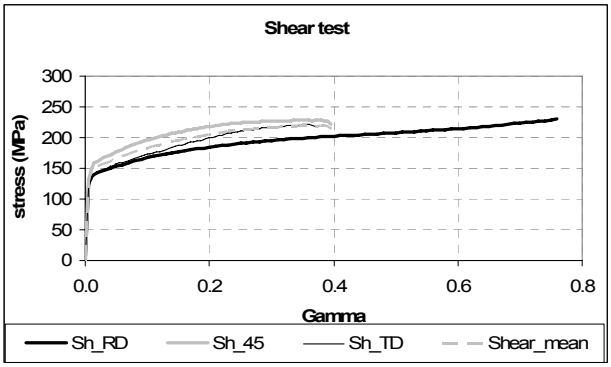

Figure A.1.5: Experimental shear tests and average curve

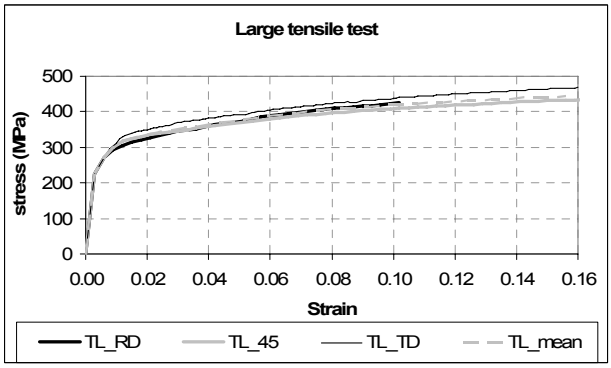

Figure A.1.6: Experimental large tensile tests and average curve

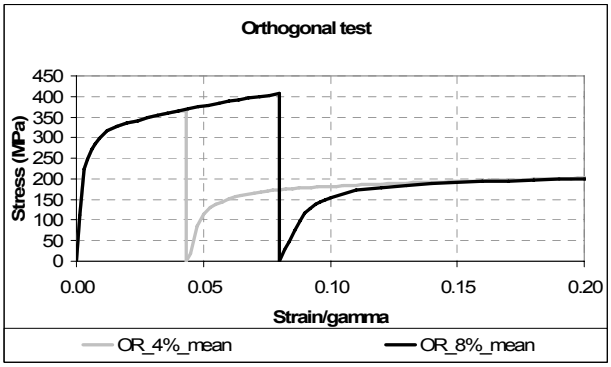

Figure A.1.7: Experimental orthogonal tests (4 and 8%)

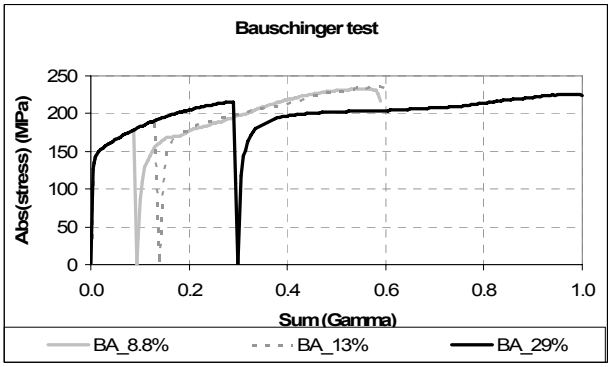

Figure A.1.8: Experimental Bauschinger tests (8.8, 13 and 29%)

All of these tests are useful to describe the yield locus shape and its evolution. The decrease of the stress in the second part of the Bauschinger test indicates that the hardening is both isotropic and kinematic. These results are used to define the material data as explained in section "SPIF – Simulations".

Superplasticity tests & model

The purposes of such tests are the detection of temperature and strain range where the superplastic behaviour is reached, the measurement of the ultimate elongation, the choice of the material law and the identification of its parameters.

- Superplasticity window

In this section, the formulations of true strain: $\varepsilon_{true} = \mathrm{Ln}\dfrac{L_i}{L_0}$ and true stress: $\sigma_{true} = \dfrac{F_i}{A_i}$ are used. The engineering strain can easily be obtained from: $\varepsilon_{eng} = \exp(\varepsilon_{true}) - 1$.

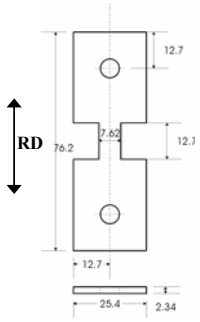

Figure A.1.9: Specimen

To start, after a bibliographical research, 44 normalised specimens (Figure A.1.9) were submitted to simple tensile tests at constant temperature and at constant true strain rate to detect the conditions of high deformation (Figure A.1.10). Some experiments performed twice showed that the stress/strain curves are almost reproducible but the ultimate elongation is difficult to replicate. The maximum strain: $\varepsilon_{true} = 2.48$ ($\varepsilon_{eng} = 10.9$) was reached at 520°C and 7.10^{-4} s^{-1} but another test with same $(T, \dot{\varepsilon})$ conditions aimed to a deformation of 2.05.

The average ultimate true strains of Table A.1.3 show dispersed results and difficulties to define the superplastic window but it is clear that high elongations systematically appear for T ∈ [500, 560]°C and $\dot{\varepsilon} \in [2.10^{-4}, 13.10^{-4}]$ s^{-1} as observed in Table A.1.3 and in Figure A.1.11.

Strain rate (s-1)	390°C	410°C	450°C	500°C	520°C	530°C	540°C	560°C	580°C
0.0002				1.4176	1.8925		1.9519		
0.0007				2.0613	2.2627		2.0373	2.0398	
0.0013			1.6575	2.1419	2.1731	2.0891	2.3776	1.8785	0.7829
0.0061					1.7863				
0.0108	1.4921	1.5420	1.6360	1.8772	1.9500		1.7859	1.4172	

Table A.1.3: Average ultimate true strain

Figure A.1.10: Superplasticity sample

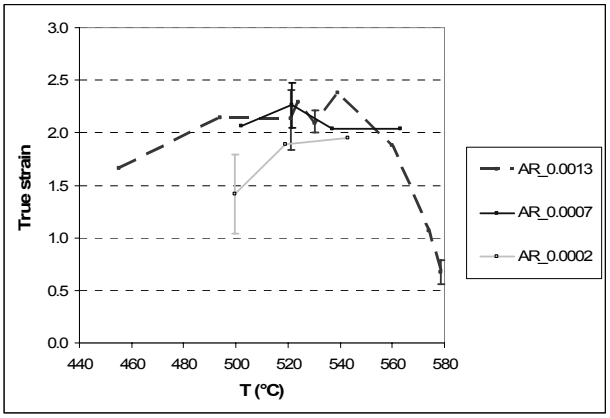

Figure A.1.11: Ultimate true strain

- Superplasticity law

The following ranges: T ∈ [500, 540]°C and $\dot{\varepsilon} \in [2.10^{-4}, 13.10^{-4}]$ s^{-1} are chosen for material data characterisation as the stress/strain curves showed reproducible results.

The two following laws: $\sigma = \sigma_0 + K.\varepsilon^n.\dot{\varepsilon}^m$ (Eq. 1) and $\sigma = C.\dot{\varepsilon}^m$ (Eq. 2) are classically used by industry to describe the material behaviour with σ= true stress and ε= true strain.

The first law (Eq. 1) is not adapted to such flat curves (see Figures A.1.12 to A.1.14) thus the second law (Eq. 2) dependending only on strain rate is chosen. Table A.1.4 represent the C and m parameters of this law (Eq. 2) fitted by Excel solver for 500, 520 and 540°C. Another global set has been fitted to characterize the behaviour at all temperature in the range [500-540] °C. Figures A.1.12 to A.1.14 show the

experimental stress/strain curves and the levels defined by the material models. Figure A.1.15 shows the stress levels comparison obtained by the four sets of data: C & m in Table A.1.4.

	500°C	520°C	540°C	[500 - 540] °C
C	33.3	50.0	279.0	161.2
m	0.212	0.281	0.534	0.448

Table A.1.4: Material data of the law: $\sigma = C.\dot{\varepsilon}^{m}$ ***for different temperature***

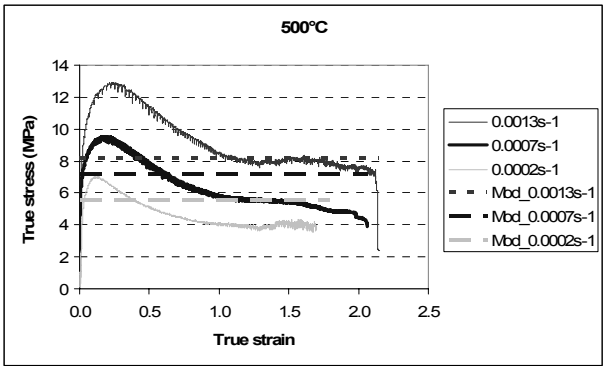

Figure A.1.12: Superplasticity tests at 500°C

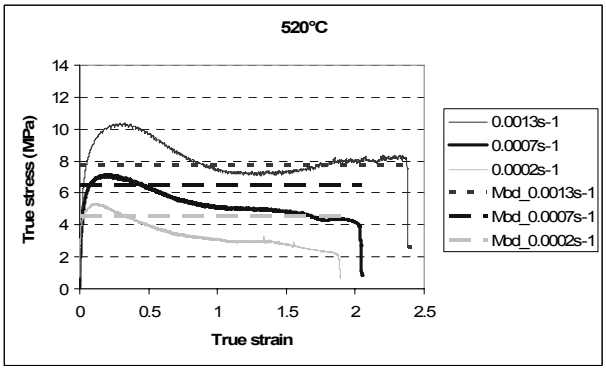

Figure A.1.13: Superplasticity tests at 520°C

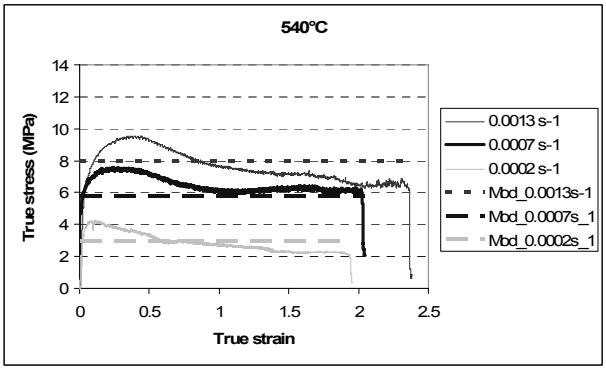

Figure A.1.14: Superplasticity tests at 540°C

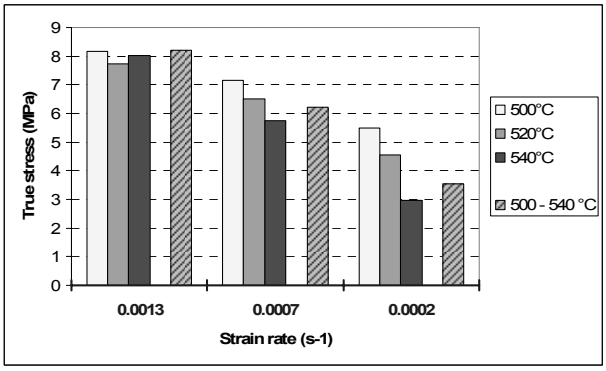

Figure A.1.15: Stresses predicted by models

Fatigue tests

The fatigue tests were performed in CRM by applying a cyclical sinusoidal stress on prismatic specimen displayed in Figure A.1.16. All the tests were performed at an R ratio value, which is the minimum peak stress divided by the maximum peak stress ($R = \sigma_{min} / \sigma_{max}$), of 0.1 (only tensile stresses).

The results of the fatigue investigation of the AR material are displayed in the following Figure A.1.17.

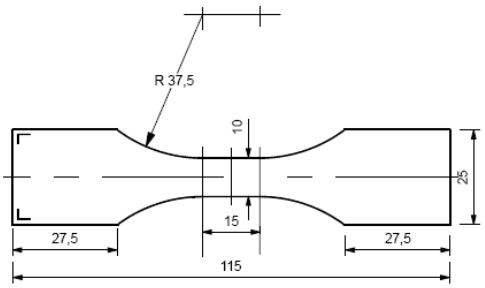

Figure A.1.16: Prismatic fatigue specimen

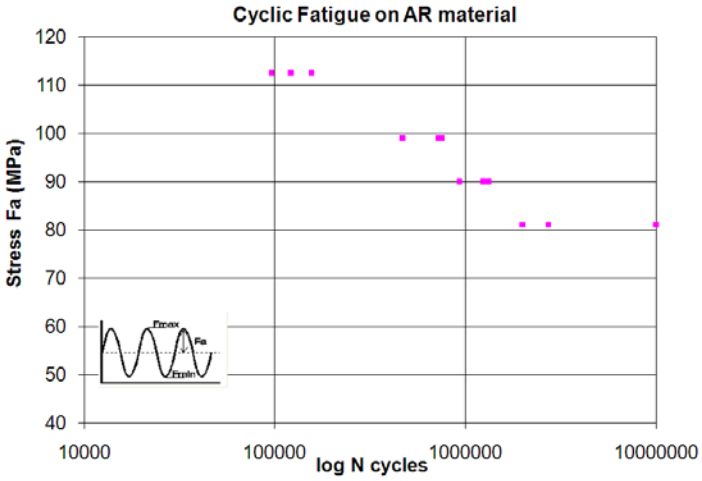

Figure A.1.17: Stress (Fa) against the number of cycles to failure (N) for the AR material

Anisotropy based on texture

The in-plane texture evolution for different directions has been studied to be compared with cold rolled material. This point is described in section 2.

2. *As Received sheets (3.2 mm) + Cold rolling (0.5 mm) + Annealing*

Cold rolling process

Samples used for SPIF process are limited in the thickness, as the maximum thickness is 1 mm. Thus, the thickness of the AR sheets has to be reduced by means of conventional cold rolling to a final thickness of 1 mm or 0.5 mm.

Annealing treatment (hardness)

The mechanical properties of the material will increase during cold rolling process due to strain hardening. Thus, an annealing treatment on these cold rolled sheets is necessary to recover the initial mechanical properties.

A range of temperatures between 100 and 400°C and 2 holding times of 30 and 60 min were investigated. Due to the time required for other tests, the measured indicator of the mechanical properties was the hardness. Figure A.2.1 shows the hardness as a function of the annealing temperature and holding time.

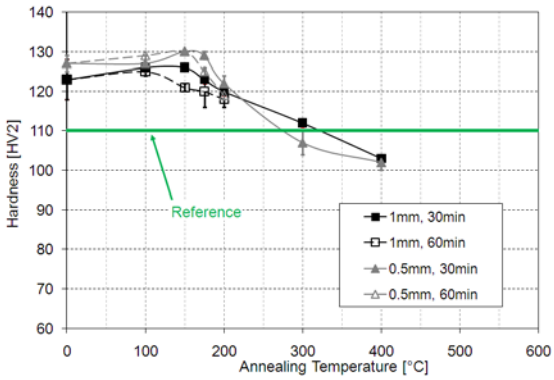

Figure A.2.1: Evolution of the hardness of the cold rolled sheets (AR) with the annealing temperature for 2 different holding times.

An annealing at 300°C - 30min leads to the initial hardness of 110 HV2 for both cold rolling processes. This reduces the range of the annealing parameter investigations. Thus, different temperatures in a range between 275 and 475°C for only a holding time of 30 min were additionally investigated. The resulting mechanical properties obtained by tensile tests after annealing are presented in Figure A.2.2.

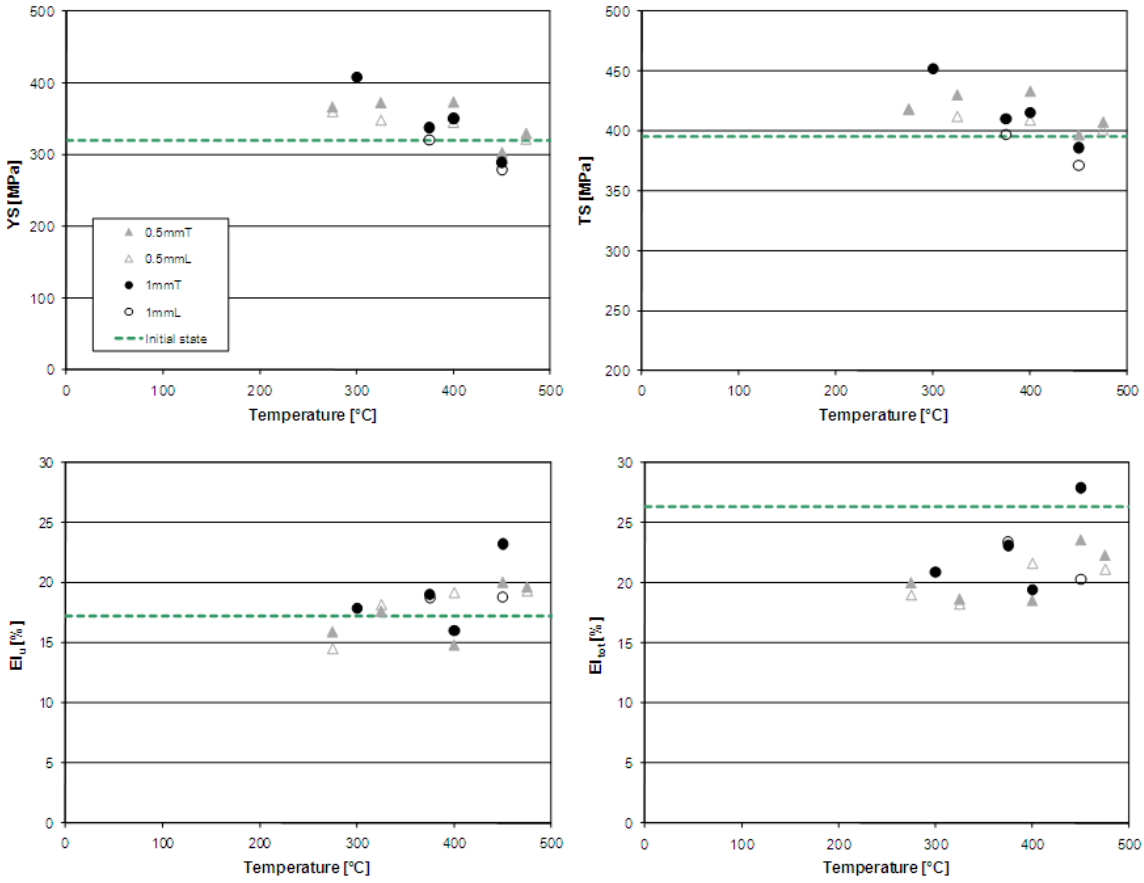

Figure A.2.2: Mechanical properties of the AR sheets after cold rolling and annealing at different temperatures (holding time of 30 min)

To reproduce the same mechanical properties, according to the previous graphics, an annealing at 410°C - 30 min on the sheets with a thickness of 1 mm and an annealing at 450°C - 30 min on the sheets with a thickness of 0.5 mm were performed.

Material difference before and after cold rolling & annealing

- Simple tensile tests

Tensile tests on smaller specimen (A25) were performed in CRM. The shape/geometry of the specimen was reduced due to the limited area of available material with a good surface quality after cold rolling. As for the AR material, specimen at 0°, 45° and 90° from the rolling direction were extracted and three tensile tests for each direction were performed. The corresponding tensile curves and the tensile curves of the AR material are displayed for all directions in Figure A.2 3 (flow curves for all tensile tests) and in Figure A.2.4 (mean curves).

Annealing treatments after cold rolling allows the material to recover the initial tensile properties. The tensile curves of the material in two different states for each direction have the same behaviour.

The uniform and total elongations cannot be compared as the tests were performed on two different specimen geometries.

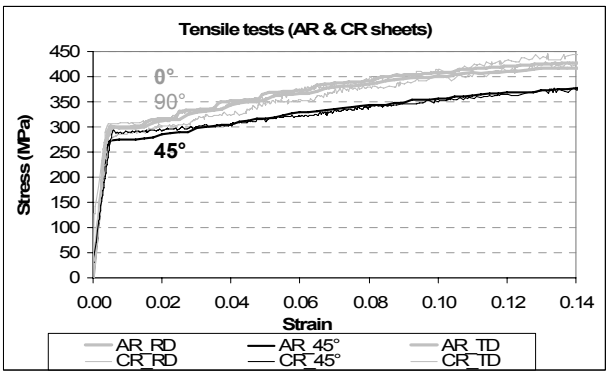

Figure A.2.3: Tensile test curves on AR material and on annealed cold rolled material located at different directions from the rolling direction

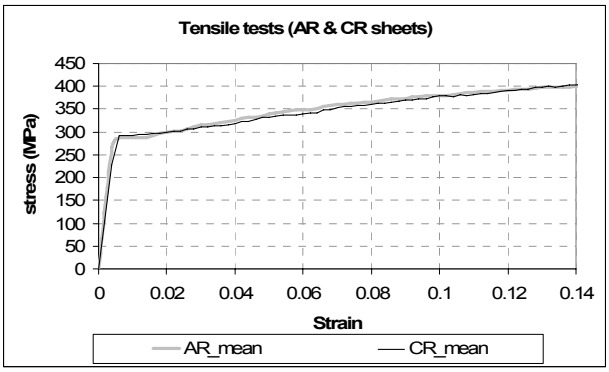

Figure A.2.4: Tensile tests on AR & CR material: average curves

- Shear & Bauschinger shear tests

These additional tests combined to the tensile tests indicate that the yield locus shape and its evolution are not modified by the cold rolling and annealing processes as observed in Figures A.2.5 & A.2.6.

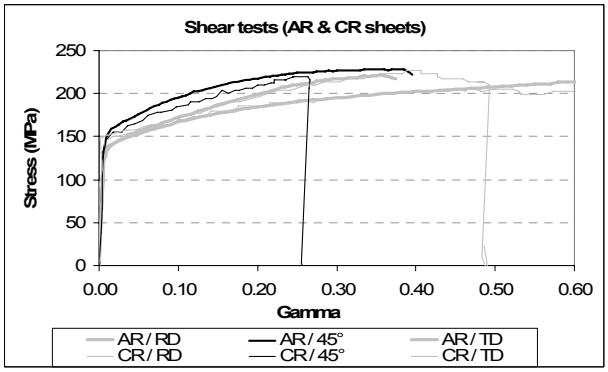

Figure A.2.5: Shear tests on AR & CR sheets

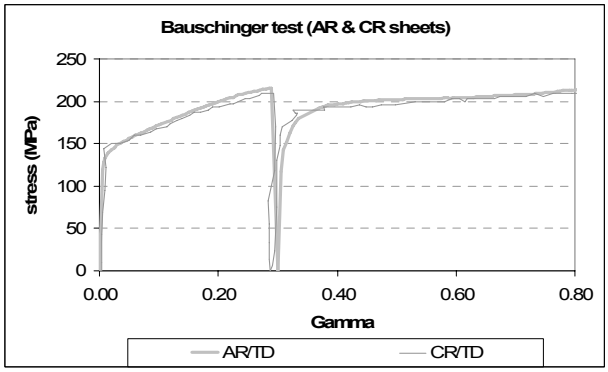

Figure A.2.6: Bauschinger tests on AR & CR sheets

- Anisotropy based on texture

The following Figures give the evolution of in-plane properties for different angle measured from the rolling direction (RD: 0°) for As Received (AR) and cold rolled (CR) materials on both the surface and the mid-section. These data are based on texture analysis and a Taylor model.

Figure A.2.7 gives the evolution of the ratio: $Q = \frac{-\varepsilon_p^{transv}}{\varepsilon_p^{length}}$ and Figure A.2.8 gives the relative yield stress (S_Y) evolution for different angles. Based on this model, $S_Y(45°)$ should reach [0.92* $S_Y(RD)$] for As Received sheets (AR) and [0.89* $S_Y(RD)$] for cold rolled sheets (CR). These predictions are consistent with the results of tensile tests performed on AR sheets where S_Y (45°)= [0.93*S_Y (RD)] (Figure A.1.1).

Based on this model, it is observed that:

- The behaviour in RD and in TD are similar but is different than at 45°;
- AR and CR materials are similar;
- SPIF performed on CR material validates the applicability of SPIF on AR sheets.

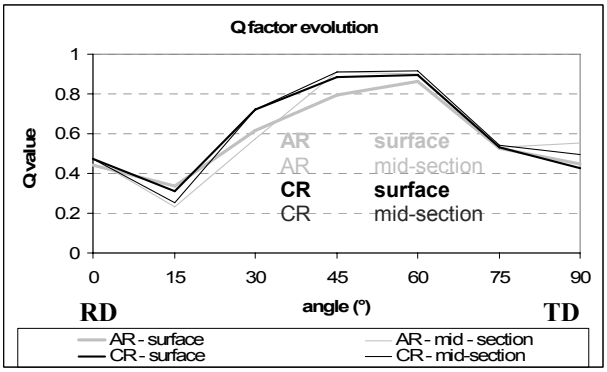

Figure A.2.7: Q factor comparison on AR/ CR sheets

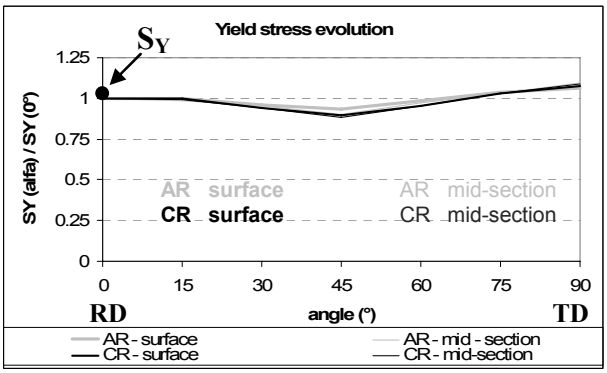

Figure A.2.8: Yield stress comparison on AR/CR sheets

Swift cup test

Additionally, some swift cup tests were performed in CRM on the cold rolled and annealed material with a thickness of 0.5 mm to investigate the homogeneity of the drawing behaviour of the sheet. As shown in Figure A.2.9, different tests were done by decreasing the specimen diameter. The lowest diameter value is associated with a cup specimen, corresponding to the sample where no crack occurred during the test. The change in the specimen diameter is also connected to a decrease of the load of the sample holder on the specimen.

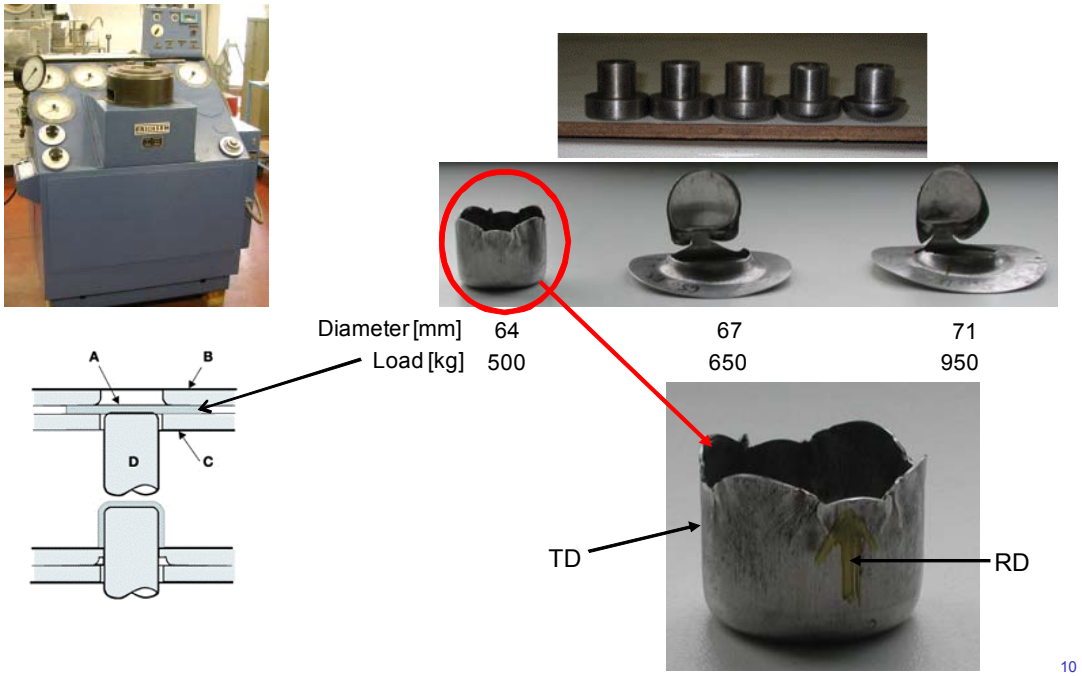

Figure A.2.9: Swift cup test device and overview of specimen with different diameters after the test

The shape of the cup obtained with a specimen diameter of 64 mm shows a strong anisotropy in the drawing properties, confirming the previous tensile test results. The drawing ears formed during the process are bigger at 45° from the rolling direction than the ears in the rolling or in the normal direction.

Bending test

Bending tests were performed in order to be used for material data validation (see section: "SPIF – Simulations / material data identification") and to give information about out-of-plane behaviour.

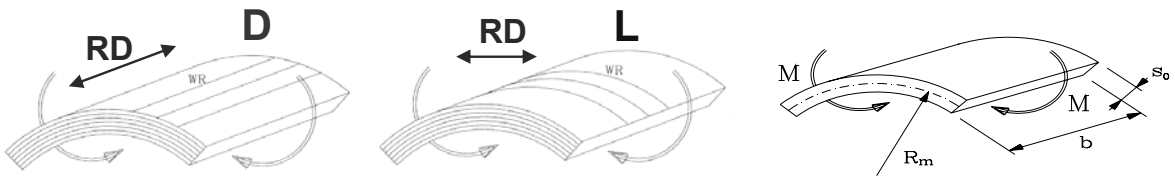

Figure A.2.10: Bending tests parallel (D) and perpendicular (L) to rolling direction and parameters used

As results, the unit moment: $\sigma^* = M / b.S_0^2$ versus strain: $\varepsilon_b = S_0 / 2*R_m$ is examined (see Figure A.2.11). Each tests, performed four times, showed a good reproducibility. Contrarily to the tensile and shear tests, these bending tests do not predict the same behaviour for the two directions: // to RD (D) and ⊥ to TD (L).

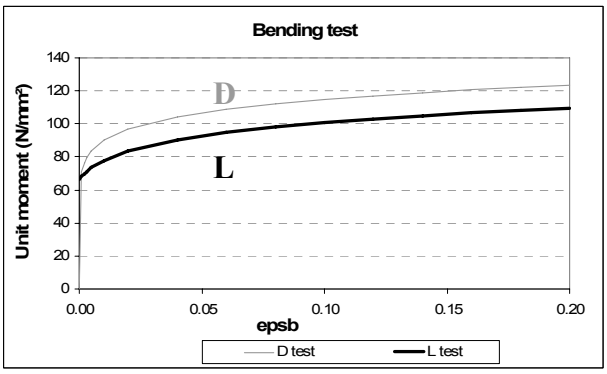

Figure A.2.11: Experimental bending test // (D) and ⊥ (L) to RD

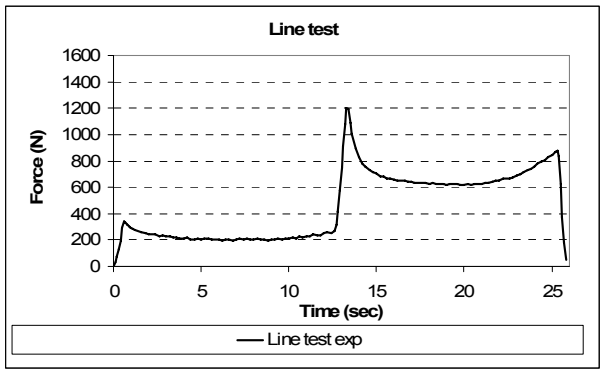

Figure A.2.12: Experimental Line test

Line test

This test presenting a deformation mechanism close to the SPIF is associated to all of the classical tests performed on AR and CR sheets to give the missing information about the out-of-plane material behaviour. Indeed, simple classical tests inducing in-plane stresses are not sufficient to describe the material behaviour during the SPIF process.

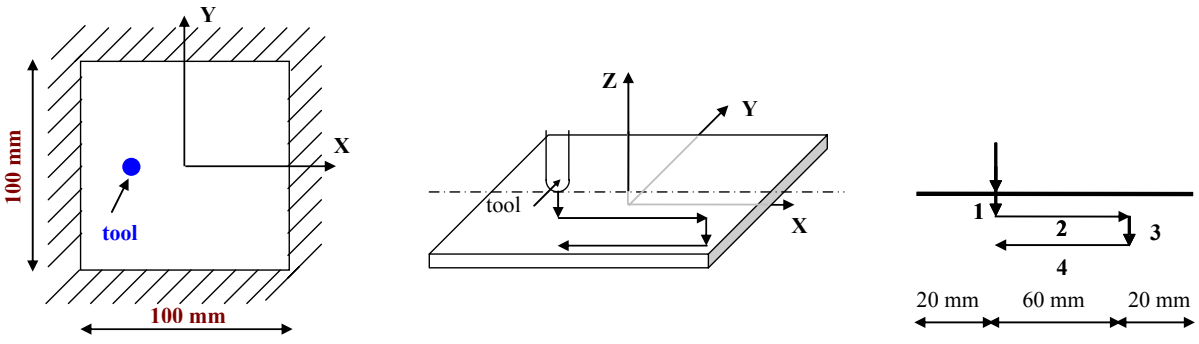

Figure A.2.13: Description of the Line test: geometry and tool displacements

A square sheet with a thickness of 0.5 mm is clamped along its edges (Figure A.2.13). The spherical tool radius is 5 mm. The test is performed three times and the bolts of the frame are tightened using the same torque to ensure the reproducibility of the results.

The displacement of the tool is composed of five steps with an initial position tangent to the surface of the sheet: a first indent of 3 mm (step 1), a line movement at the same depth along the X axis (step 2), then a second indent up to the depth of 6 mm (step 3) followed by a line at the same depth along the X axis (step 4) and the unloading (step 5).

The first step of this test (indent test) is combined to all of the classical tests to define the material data. Then the whole test (the 5 steps) is used as a first validation of the characterisation. As result, the total tool force evolution during the process (Figure A.2.12) is used (see section “SPIF – Simulations / Line test”).

3. As Received sheets (3.2 mm) + Cold rolling (0.5 mm) + Annealing + SPIF

SPIF process: Pyramid

Single Point Incremental Forming is a process characterized by the large deformations it induces in the workpieces. The influence of these deformations on the structural integrity and the microstructure of different materials is often still unknown.

For characterisation of the material discussed further in this chapter a pyramidal geometry was made using SPIF. The chosen geometry had to comply with some demands as to make characterisation tests feasible. The biggest constraint on geometry is imposed by the dimensions and flatness of the samples for tensile testing.

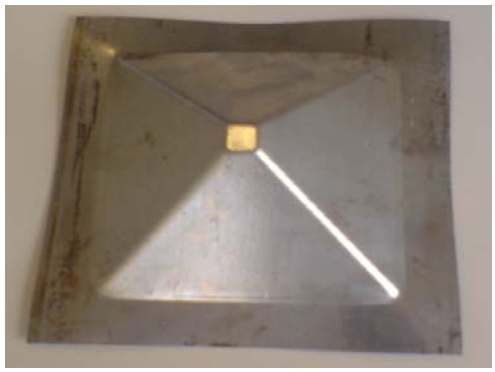

Figure A.3.1: Pyramidal geometry

In SPIF the drawing angle will have an important effect on the amount of deformation induced in the sheet. For a given material and thickness a maximum drawing angle can be determined which represents the limits of the conventional incremental forming process. Above this angle the part will fracture during forming.

Because a large range of industrial applications have features that approach the maximum forming angle, material characterisation by Tensile testing was done on a part formed close to the maximum drawing angle and on a part 6 degrees away from the maximum drawing angle.

As explained further in this report, the maximum forming angle for the As Received sheets (3.2 mm) which was cold rolled to 0.5 mm and annealed to recuperate the initial mechanical properties, is found to be 46 degrees.

In addition to the material thickness the diameter of the spherically tipped tool and incremental step between two contours are other factors which influence the maximum forming angle. In this study the step between two contours is specified as the scallop height as one would see between two milling contours using a ball nose mill.

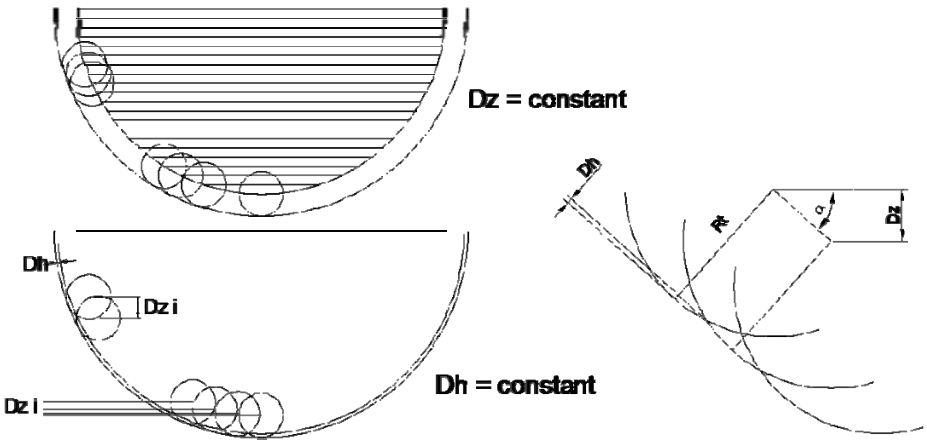

Figure A.3.2: Pyramid parameters

The parameters used in for the pyramids out of which the tensile samples were extracted are (Figure A.3.2):

- Material: As Received (3.2 mm) + cold rolling (0.5 mm) + annealing
- Tool diameter (Td) = 10 mm
- Drawing angle (α) = 40° and 45°
- Pyramid base : 176 x 176 mm
- Scallop height (Δ h) = 0.05 mm

- Initial sheet thickness (t) = 0.5 mm
- Total depth = 66 mm (40°) – 80 mm (45°)

Due to residual stress the walls of the pyramid curved after releasing the boundary conditions by cutting out the different wall features (Figure A.3.3). To extract accurate tensile samples a new mounting rig was designed to clamp the curved wall features flat. Once clamped the tensile samples were cut out using wire EDM.

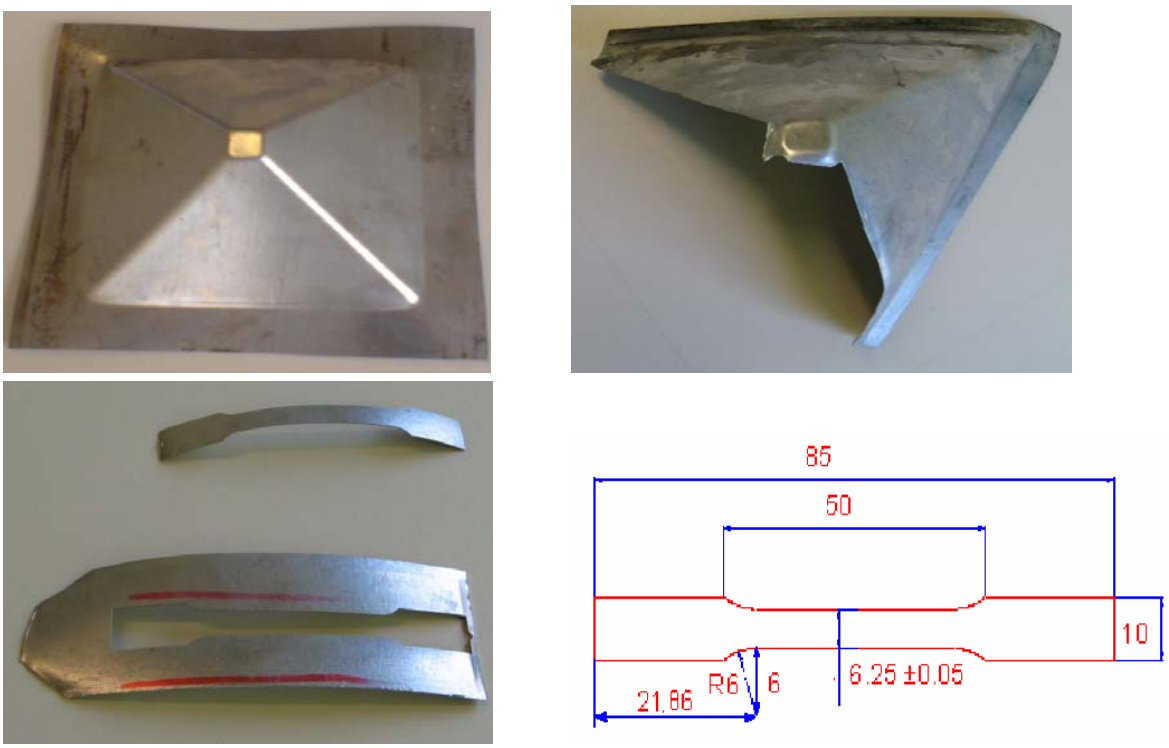

Figure A.3.3: Tensile test specimen

To study the influence of the rolling direction of the initial blank sheet and the direction of the tool progression tensile samples were extracted in all different combinations of parallel and perpendicular to these directions (Figure A.3.4).

Texture analysis was done on similar pyramids. Because only small rectangle samples are needed for this analysis there were no strict limitations for the part geometry.

Material difference before and after SPIF

- Simple tensile tests

Four different combinations of sample positions were studied: in rolling (W//) or transversal directions (W⊥) and also sample length in or transversal to the tool displacement (T// or T⊥) (Figure A.3.4). Additionally, two different cone shapes with different wall angles (40° and 45°) were investigated. The tensile tests were performed on A25 tensile specimen. Two tests for each condition were done. Before performing the tensile tests, all specimens had a bended shape due to SPIF process.

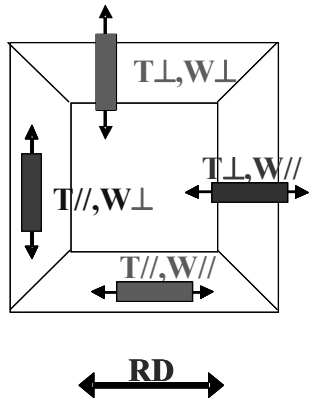

Figure A.3.4: Tensile specimen

The corresponding mechanical properties are given in the following figure. The initial tensile properties are also displayed.

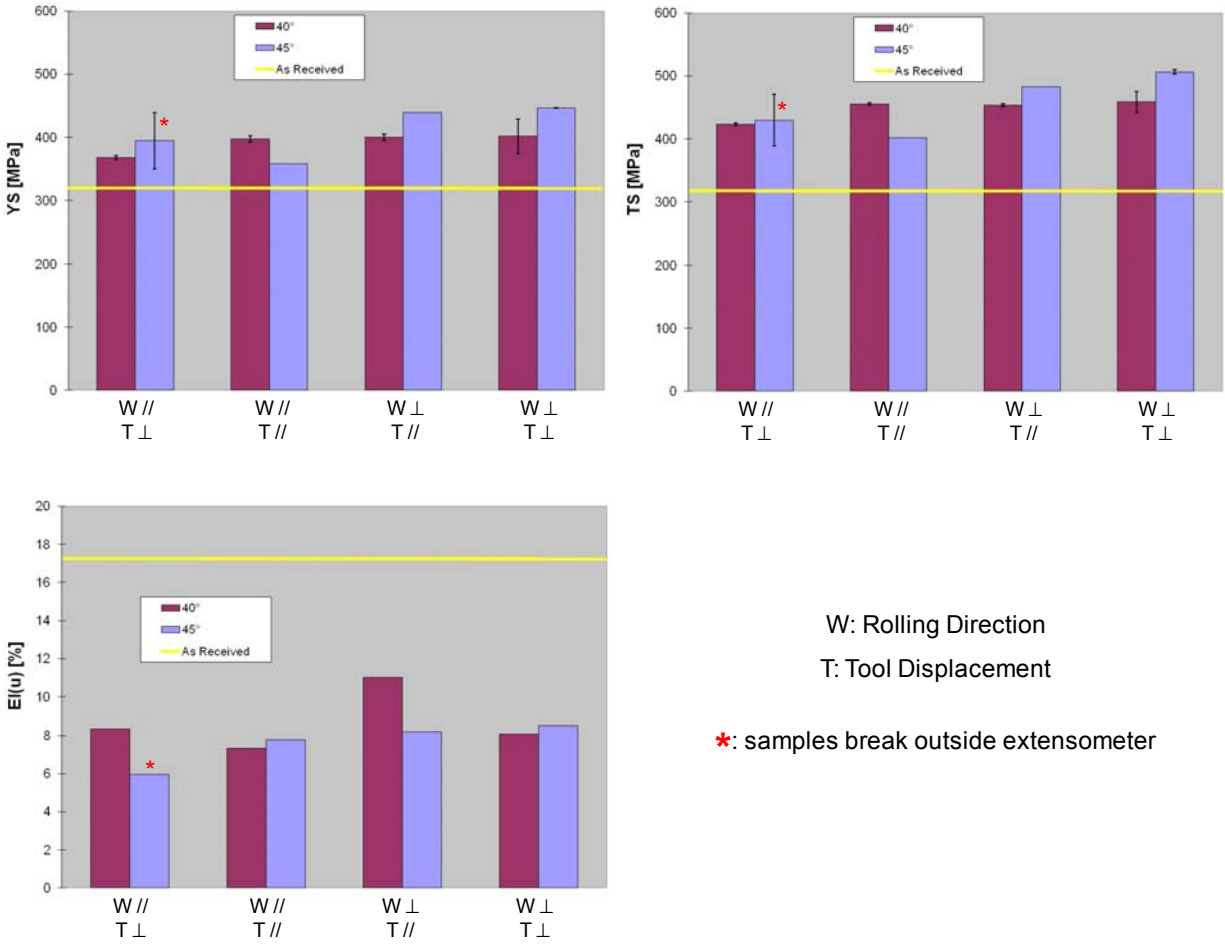

Figure A.3.5: Tensile properties after SPIF for two wall angles

The yield strength and the tensile strength are higher after SPIF process than for the As Received material; however the ultimate elongation is systematically lower. A significant effect of the displacement of the tool or of the wall angle on the mechanical properties is not observed.

The tensile tests were also compared to measure the effect of initial anisotropy and the anisotropy due to the SPIF process. To facilitate the comparison of stress/strain curves, the true stress (MPa) reached for a true strain of 7% is examined.

It is observed (in Figure A.3.6 and in Table A.3.1) that the wall angle sensitivity is observable. The SPIF clearly increases the hardening state: the stresses for SPIF 40 and 45° reach respectively 123% and 132% of the AR sheets one.

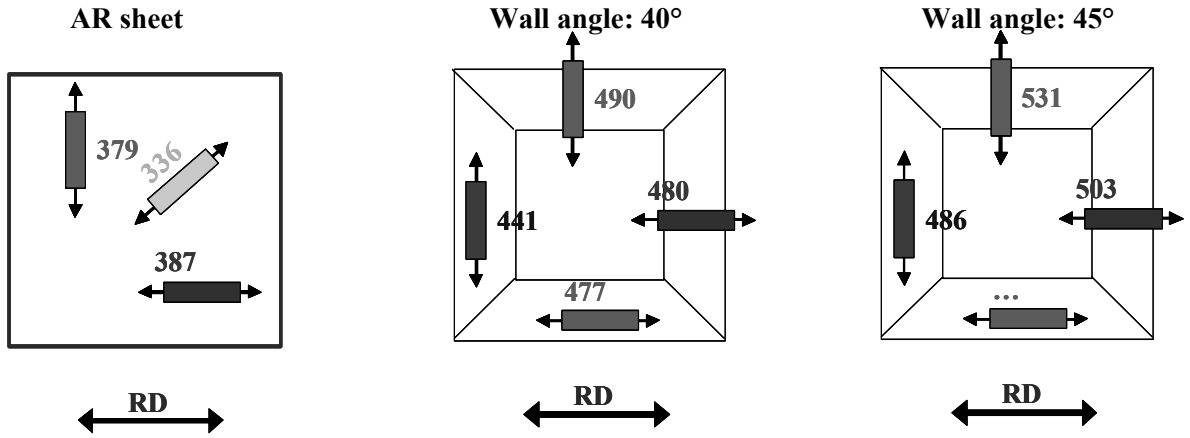

Figure A.3.6: True stress for a true strain of 7% on AR sheet and samples from pyramid (40° and 45°)

AR sheets			SPIF 40°			SPIF 45°		
RD	TD	Average	RD	TD	Average	RD	TD	Average
387	379	383	478.5	465.5	472	503	508.5	505.8
		100%			123%			132%

Table A.3.1: Stress comparison for different materials and orientations

The initial anisotropy of the sheet was relatively low; the difference between RD / TD is small and is not well observable on SPIF samples.

The analysis of anisotropy due to SPIF process does not give consistent results. The material was not homogeneous in the wall and the tests were not reproducible.

- Anisotropy based on texture

The samples of SPIF material were extracted out of a pyramid (150*150 mm², thickness: 0.5mm, tool ϕ: 10 mm, α= 40°, scallop height= 0.05 mm) from two walls (see Figure A.3.7).

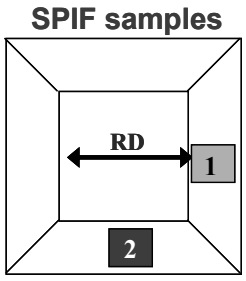

Fig.A.3.7: Samples position

Once again, the Q factor (Figure A.3.8) and the yield stress (Figure A.3.9) evolutions are studied for different angles from RD and compared with CR sheets.

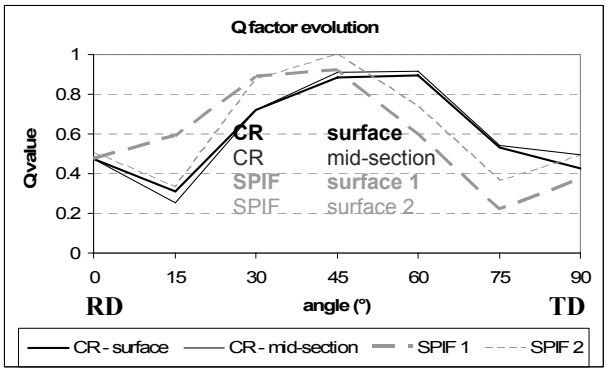

Figure A.3.8: Q factor comparison on CR / SPIF sheets

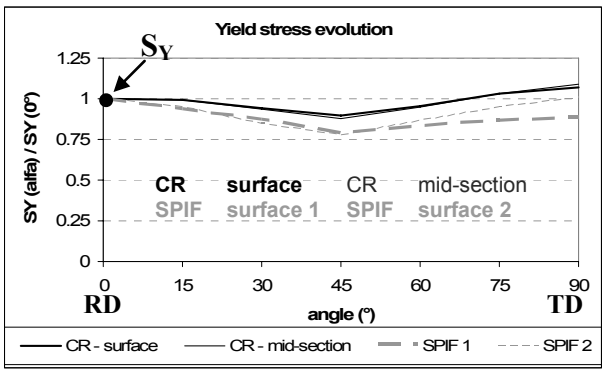

Figure A.3.9: Yield stress comparison on CR / SPIF sheets

Based on this model, it is observed that:

- The Q factor is once again similar in RD and TD but is different at 45°;
- The yield stress evolution is lower at 45° than in RD or TD;
- The anisotropy is relatively low. The ratio Sy (45°) / Sy (RD), where Sy is the yield stress, is estimated to 0.78, 0.92 and 0.89 for respectively SPIF, AR and CR material.
- The SPIF process modifies the texture.

4. As Received sheets (3.2 mm) + I-ECAP process (sheet)

IECAP process

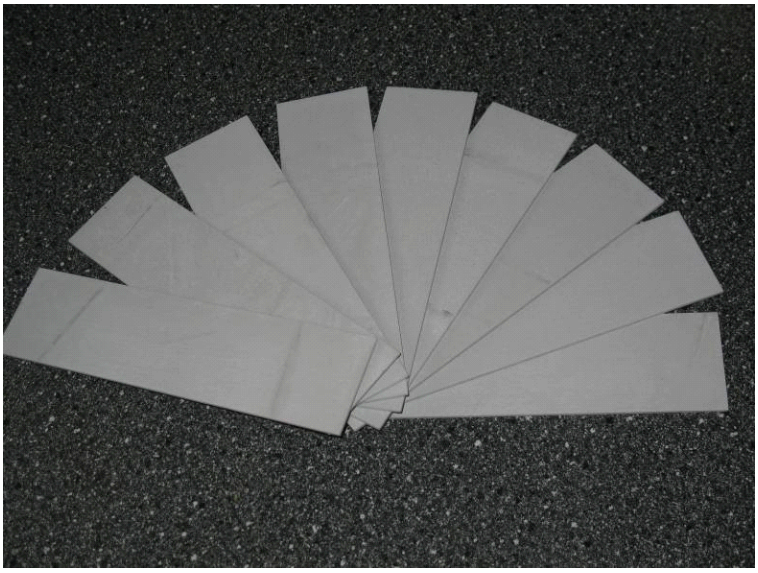

Figure A.4.1: Conversion coated strips

Figure A.4.2: I-ECAP'ed strips

The initial material was 3.2 mm thick sheet rolled by Aleris Aluminum Koblenz GmbH. This sheet was subsequently machined to reduce its thickness to 2 mm. The remaining dimensions were 50×190. The strips were covered with a conversion coating of calcium aluminate (Figure A.4.1) and lubricated with molybdenum disulphide before being subjected to I-ECAP at 200°C (Figure A.4.2). After 6 passes of I-ECAP, the strips were machined with sand paper from thickness of 1.9 mm down to 1.75 mm (6 strips) and 1.5 mm (3 strips). Thus the total number of strips produced for further testing was 9 (Figure A.4.3).

Figure A.4.3: Strips after 6 passes of I-ECAP and machining with sand paper

Material difference before and after I-ECAP process

- Simple tensile tests

Three A25 tensile specimens along the length of the sheets were machined and conventional tensile tests were performed. The corresponding mechanical properties with the values of the AR material are displayed in the following table:

	$YS_{0.2}$ [MPa]	TS [MPa]	El(u) [%]	El(t) [%]
AR sheet	317	389	15.4	27.9
I-ECAP'ed sheet	340	400	9.7	13.1

Table A.4.1: Mechanical properties of AR material and I-ECAP'ed sheet

I-ECAP process induced strain hardening which leads to an increase of yield strength and tensile strength and a decrease of the uniform and total elongations.

- Microstructure (texture)

Figure A.4.4.a shows the result of an EBSD scan, made on the longitudinal section of an Al-Mg-Sc sheet, produced by incremental ECAP (I-ECAP). The starting material was an AR 3.2 mm sheet. The microstructure after I-ECAP is not perfectly homogeneous since stringers of elongated and not subdivided grains are still present. Nevertheless, the subdivision is fairly well developed and the grain size distribution (Figure A.4.4.b) shows that the average grain size is around 1 µm.

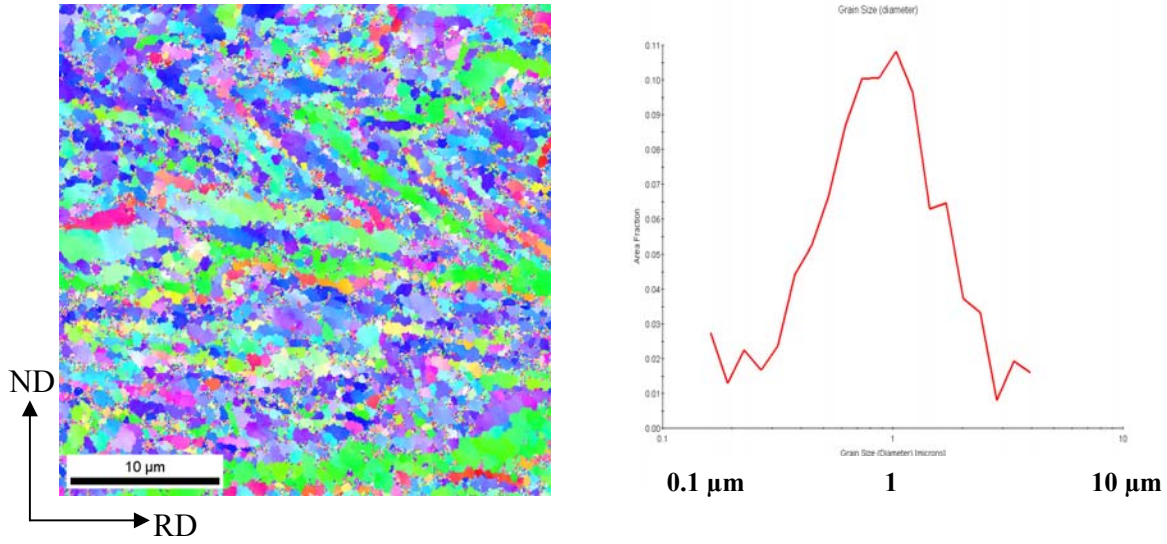

Figure A.4.4: (a) EBSD scan on a longitudinal section of an I-ECAP'ed sheet and (b) grain size distribution

According to the pole figure, shown in Figure A.4.5, a large number of grains seems to have a [111] direction parallel to TD.

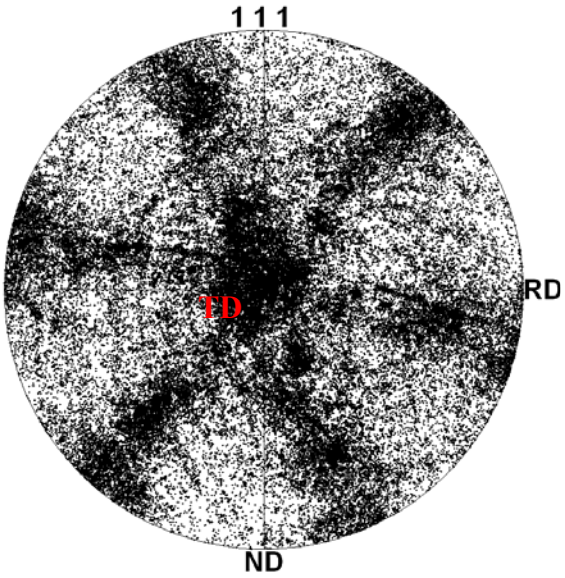

Figure A.4.5: 111 pole figure of an I-ECAP sheet
RD=rolling direction, ND=normal to the plate, TD=transverse direction

Texture measurements of the I-ECAP sheet (6 passes, route C) have been made by X-ray diffraction on the surface and on 50% depth of the sample. Some representative sections of the ODF are shown in Figure A.4.6 for the sample surface and in Figure A.4.7 for the mid-thickness.

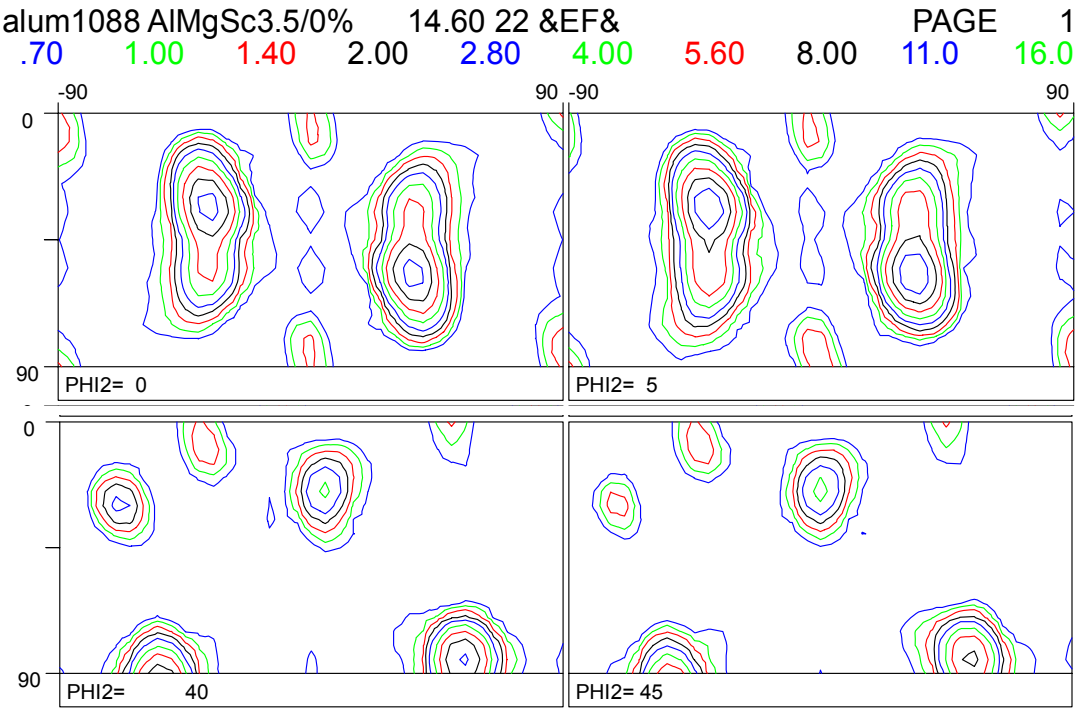

Figure A.4.6. Some φ2 ODF sections of the surface of an I-ECAP sheet, measured after 6 ECAP passes route C

The surface texture is less strong than the texture in the bulk of the sheet: the maximum intensity is less and the orientations are much more spread out around the texture maxima.

Unfortunately the peaks do not coincide with the typical peaks normally found after several ECAP passes, route C in a die with an angle of 90°C.

It is known that the ECAP die angle (or in other words, the angle of the shear plane with respect to the extrusion direction) has a strong influence on the location of the texture maxima, so perhaps the shear that occurs in each incremental pass over the thickness of the sheet is not located at an angle of 45° with to extrusion direction. Further simulations and measurements are needed to clarify this point.

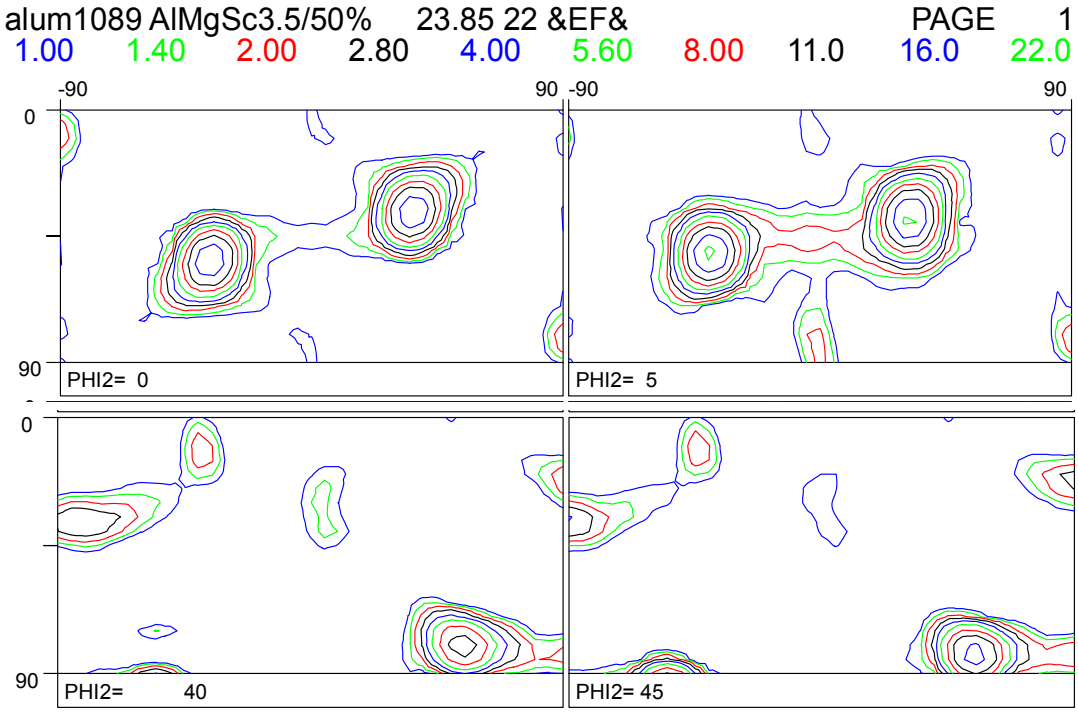

Figure A.4.7: Some φ2 ODF sections of the mid-thickness of an I-ECAP sheet, measured after 6 ECAP passes route C

Superplasticity tests

The number of I-ECAP sheets was limited and only two normalised samples per sheet could be extracted. Thus, only four tests were performed. The purpose was to verify that the superplastic behaviour was kept. Two temperatures (500 and 520 °C) and two strain rate (0.0002 and 0.0013 s^{-1}) were selected.

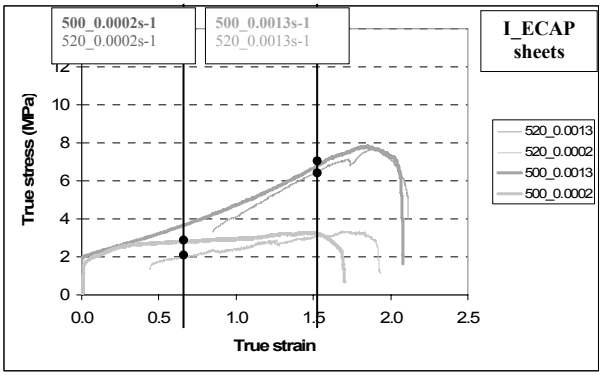

Figure A.4.8: Superplasticity tests on I-ECAP sheet

	500°C	520°C
0.0002 s-1	1.70	1.85
0.0013 s-1	2.08	2.12

Table A.4.2: Ultimate engineering strain

The reproducibility of these tests could not be verified but it is clear that the superplasticity is kept (see Figure A.4.8). The stress/strain curves have another shape than in case of As Received sheets. It is also observed that the I-ECAP process modifies the hardening behaviour.

See section: "Process comparison" for comparison of these curves with those of As Received material and I-ECAP bars.

Fatigue tests

The same procedure as for the AR material was carried out on the I-ECAP'ed sheet material for the fatigue investigation. The results are given in the following figure:

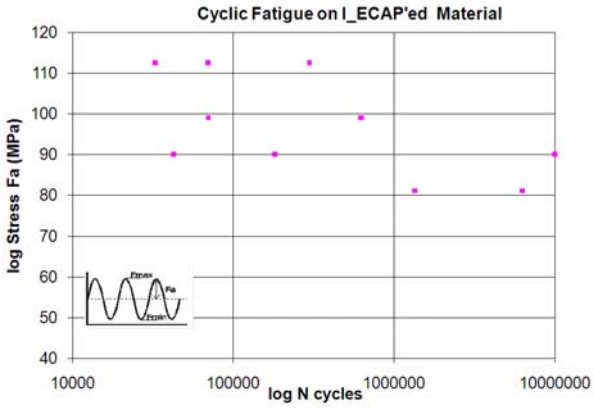

Figure A.4.9: Stress (Fa) against the number of cycles to failure (N) for the I-ECAP'ed material

The deviation of the experimental points is caused by the microstructural state of the material after I-ECAP process. The precipitation and the strain hardening could lead to a heterogeneous behaviour probably due to internal micro-cracks or different residual stresses states. The fatigue life seems to be lower for the I-ECAP'ed material than for the AR material.

5. ***As Received bulk (30 mm)***

Hardness and thermal stability

The hardness of the initial material is 76 Hv. Several heat treatments were realized, each on a different sample, at four different temperatures (310°C, 400°C, 450°C and 500°C) and during various times (45 min, 2h and 4h for all the temperatures and an additional duration of 25h at 450°C). Figure A.5.1 shows the hardness values of the AR material and also the hardness evolution versus the heat treatment time for each temperature. Taking the error bars into consideration, it appears that at 310°C and 400°C, the hardness is almost constant during at least 4h. At 450°C, a decrease of the hardness is noticed for the heat treatment applied during 25h but up to 4h of annealing the hardness doesn't change significantly. On the other hand, a clear decrease of the hardness occurs after 45 minutes annealing at 500°C.

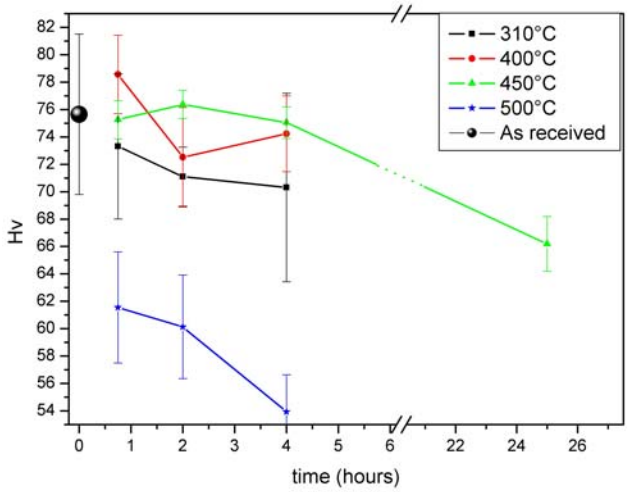

Figure A.5.1: Hardness evolution versus the duration of heat treatment realized at different temperatures.

Microstructure

The EBSD technique revealed that the As Received 30 mm plate consists of "pancake-shaped" grains, 8 – 20 µm in thickness and a minority of fine equiaxed grains smaller than 3 µm. The structure shows that recrystallisation during hot rolling is extremely difficult (Figure A.5.2.a).

SEM observations associated with EDX analysis evidenced the presence of three types of dispersoïds in the AR material: i) spherical particles containing Sc and Zr with a mean diameter around 4 µm; (ii) particles containing Si that are elongated (mean length around 6.5 µm and thickness around 180 nm); (iii) elongated particles containing Fe and Mn with a mean length around 2.5 µm and a thickness around 900 nm.

TEM observations revealed the presence of large precipitates containing Mg and Si and also a homogeneous distribution of “coffee bean” contrasts that is known to correspond to coherency strain contrast created by coherent nano-particles in the matrix. These nano-particles, which were evidenced to belong to the LI2 structure, are Al_3Sc or $Al_3(Sc_xZr_{x-1})$ precipitates (Figure A.5.2.b). The mean diameter of these nano-precipitates is around 9 nm.

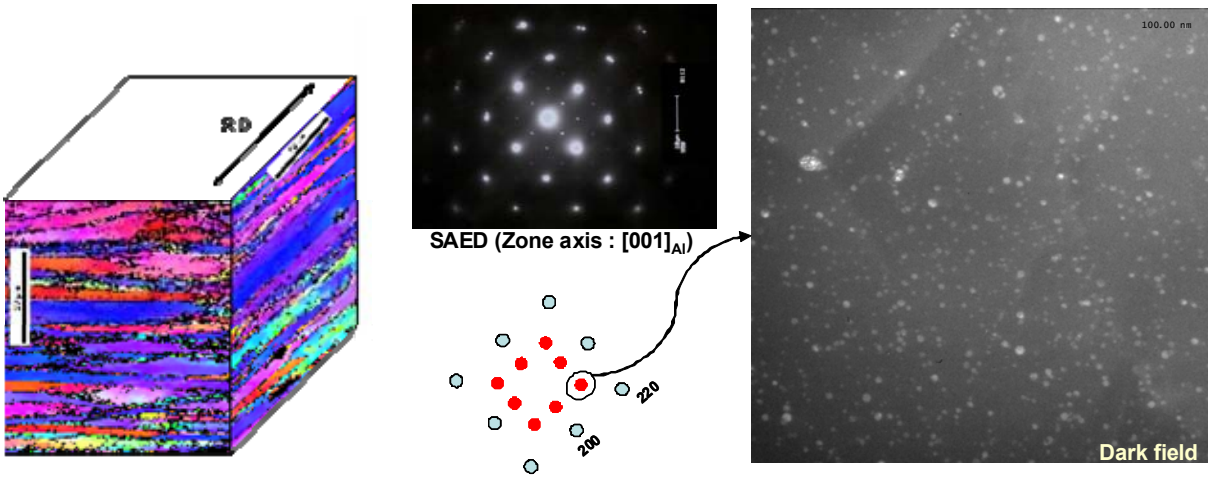

Figure A.5.2: (a) EBSD image of the AR 30 mm plate, showing pancake shaped grains; (b) dark field TEM image of the nano-sized $Al_3(Sc_xZr_{x-1})$ precipitates

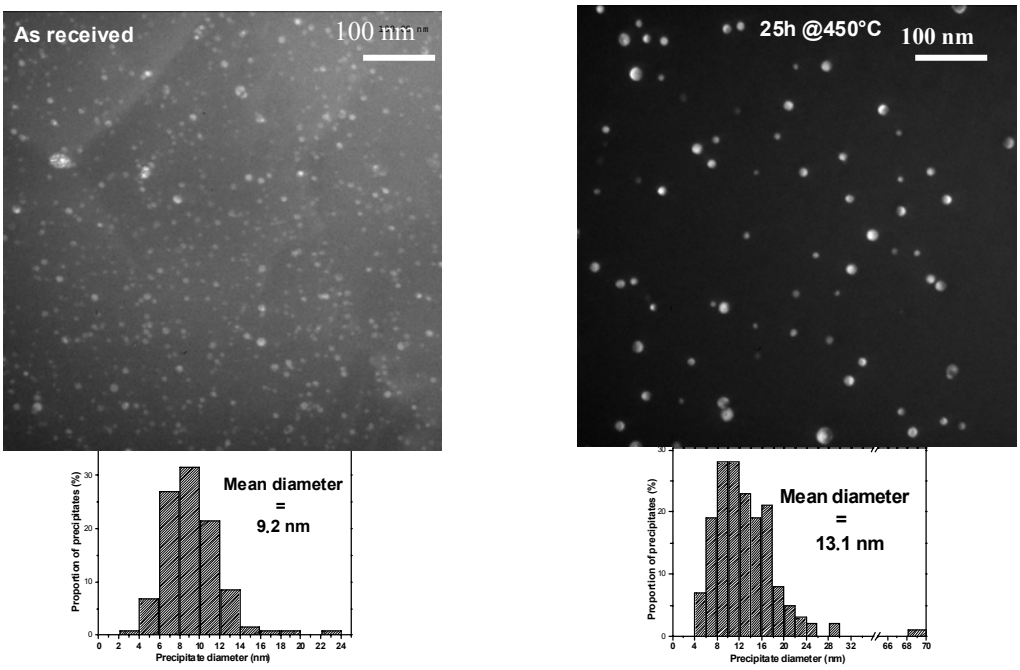

Figure A.5.3: Comparison of the size of nano-sized $Al_3(Sc_xZr_{x-1})$ precipitates in the AR material and after 25h at 450°C

For heat-treated samples characterized by a decrease of the hardness, grain boundary migration occurred, leading to a slight increase of the grain thickness to 15

- 50 µm. Moreover, SEM observations showed the presence of the same three types of dispersoïds that were evidenced in the AR material: ones containing Sc and Zr, others containing Si and the last ones containing Mn and Fe. It was also noticed that some of these dispersoïds seems to be larger than in the AR material.

TEM observations clearly evidenced that the decrease of the hardness comes with microstructural modifications at the nanometer scale. The size of the Al_3Sc or $Al_3(ScxZrx-1)$ precipitates clearly increases when a long heat treatment (25h at 450°C) is applied (see Figure A.5.3). Their mean diameter is around 13 nm and different strain contrast surrounds the largest Al_3Sc or $Al_3(ScxZrx-1)$ nano-precipitates which may become semi-coherent. This can explain the observed grain coarsening which is controlled by the coarsening of the pinning particles (increase of interparticle distance) and a decrease of the pinning force.

6. As Received bulk (30 mm) + I-ECAP process (bar)

I-ECAP process description

The preliminary trials of I-ECAP of bars were carried out at room temperature on two AlMgSc bars (10x10x190) received from MTM.

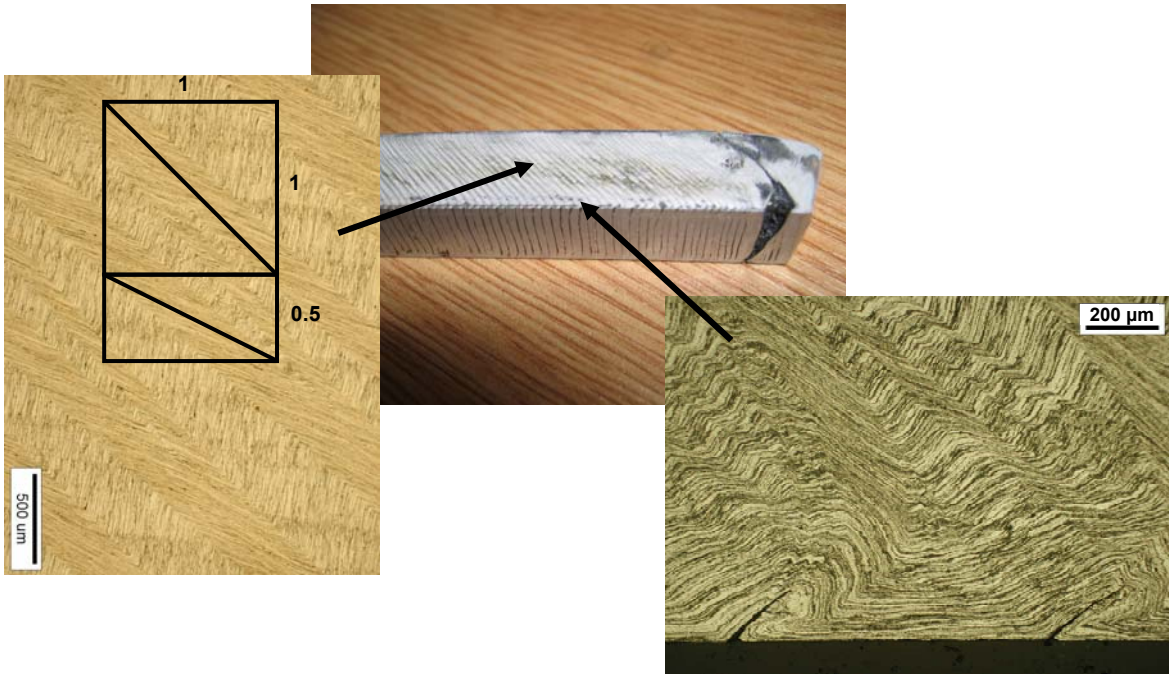

Figure A.6.1: Shear band strain localisation during 2nd pass of I-ECAP at room temperature

Only two passes of I-ECAP were achieved because of very intensive strain localisation in the form of shear bands (Figure A.6.1). These shear bands, visible on

the side surface, were inclined at about 45° (tan45°=1/1), while the material inside them was sheared at about 26.6° (tan26.6°=0.5/1), both angles being expected because of the channel bend of 90°. The crack-like features on the bottom side of the bar (from the die side) appeared to be folds. However, there was one major crack at the front end of the bar.

The next series of trials was carried out at 200°C. Twelve 10x10x190 bars were cut out from a block of AlMgSc shown in Figure A.6.2, conversion coated (Figure A.6.3) and lubricated with MoS_2. This time, no strain localisation was observed (Figure A.6.4), which enabled the bars to be processed 6 times.

Figure A.6.2: Block of AlMgSc

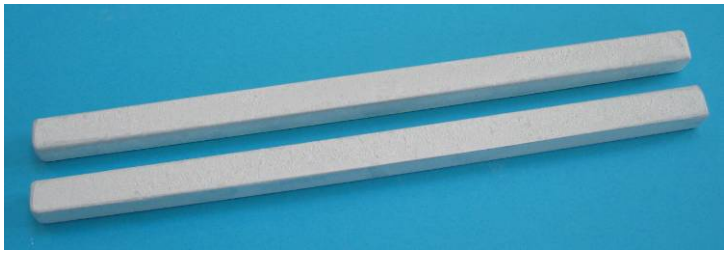

Figure A.6.3: Conversion coated bars

Figure A.6.4: ECAP processed bars

Microstructure

The microstructure of a bar, machined from the AR 30 mm plate and subjected to 6 I-ECAP passes is shown in Figure A.6.5. Although the quality of this scan is very bad, the result suggest that large parts of the structure have not yet been subdivided.

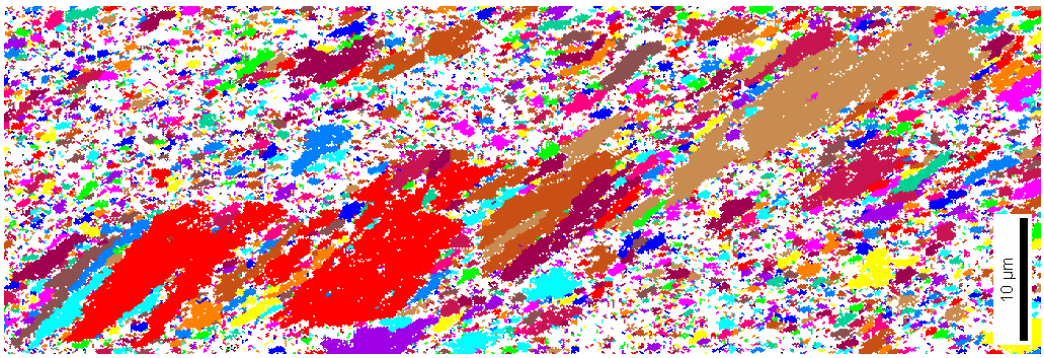

Figure A.6.5: (Partial) EBSD scan of the longitudinal section of a sample after 6 I-ECAP passes

7. As Received bulk (30 mm) + I-ECAP process (bar) + Cold rolling (1.3 mm)

Cold rolling (+ compression) process description

Specimens for mechanical characterisation require geometries larger than the geometry of the 10x10 mm² section bars. Thus, CRM performed plane strain compression on the bars, from 10 mm thickness down to 6 mm, followed by an annealing at 200°C – 30 min. A second step with a compression down to 4.8 mm was performed. The final thickness was limited by the maximal forces (2000 kN) of the MTS compression machine. Finally, the samples were annealed at 200°C – 30 min. Additionally, the compressed bars were cold rolled to a maximal final thickness of 1.5 mm.

Material characterisation

- Simple tensile tests

Three A25 tensile specimens along the length of the sheets were machined and conventional tensile tests were performed. The corresponding mechanical properties with the values of the AR material are displayed in the following table:

	$YS_{0.2}$ [MPa]	**TS [MPa]**	**El(u) [%]**	**El(t) [%]**
AR sheet	317	389	15.4	27.9
I-ECAP'ed sheet	507	558	5.4	8.4

Table A.7.1: Mechanical properties of AR material and I-ECAP'ed sheet

The procedure compression + conventional cold rolling induced a very strong strain hardening which leads to a high increase of yield strength and tensile strength and a high decrease of the uniform and total elongations. The brittleness of the resulting material connected to its bad surface quality did not allow any fatigue investigation.

Superplasticity tests

Only a limited amount of material submitted to this process was available. Therefore, only six normalised samples could be extracted out of the sheets for such tests. The purpose is to verify that the superplastic behaviour is kept by the I-ECAP process combined with the compression and a cold rolling (CR). Three temperatures (500, 520 and 540 °C) and two strain rates (0.0002 and 0.0013 s^{-1}) were selected.

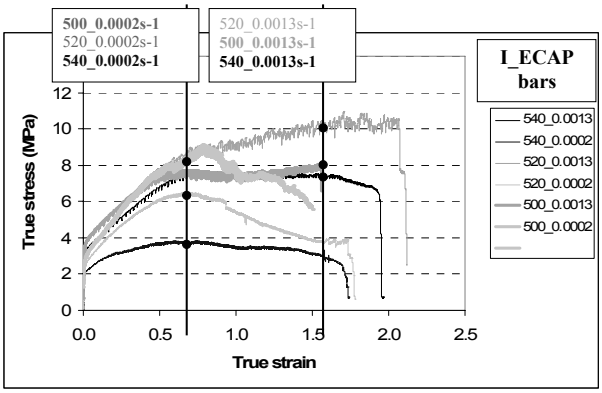

Figure A.7.1: Superplasticity tests on I-ECAP bar + CR

	500°C	520°C	540°C
0.0002 s-1	1.50	1.78	1.74
0.0013 s-1	1.56	2.12	1.97

Table A.7.2: Ultimate engineering strain

The reproducibility of these tests could not be verified but it is clear that even if the elongation is smaller than for the As Received sheet, the superplasticity is kept in these conditions (Figure A.7.1). The stress/strain curves have another shape and the peak is low or does not exist any more. The tests show the impact of the I-ECAP process (+ compression & CR) on the hardening behaviour.

See section: "Process comparison" for comparison of these curves with those of As Received material and I-ECAP sheets.

8. <u>As Received bulk (30 mm) + ECAP process (billet)</u>

Hardness

For the initial ECAP experiments, cylindrical samples (∅ 11.8 mm and h = 60 mm) have been used. The aim of these experiments is to find the optimal parameters to generate a sound block of material with submicron grains. Cylindrical samples have been extruded at 130°C, 150°C, 200°C and 400°C for 1, 4, 6 and 8 passes, using route Bc and an extrusion rate of 5 mm/min. As shown in Figure A.8.1, ECAP at 400°C generates nearly no change in hardness. During ECAP at 200°C an increase in hardness occurs during the first 6 passes (from 90 Hv to 125 Hv). After 6 or 8

passes some cracks are visible at the sample surface. ECAP at lower temperatures (130°C and 150°C) yields an increase in hardness with lower ECAP temperature.

Microstructure (TEM, EBSD)

Microstructural investigation of several ECAP'ed samples leads to the conclusion that in none of the cases displayed in Figure A.8.1, a real and fully developed submicron grain structure has been obtained. The best ECAP temperature seems to be around 200°C, but after 8 passes still some "large grains" are present in the structure. Presumably more ECAP passes (10 or 12) are needed to obtain a fully refined structure.

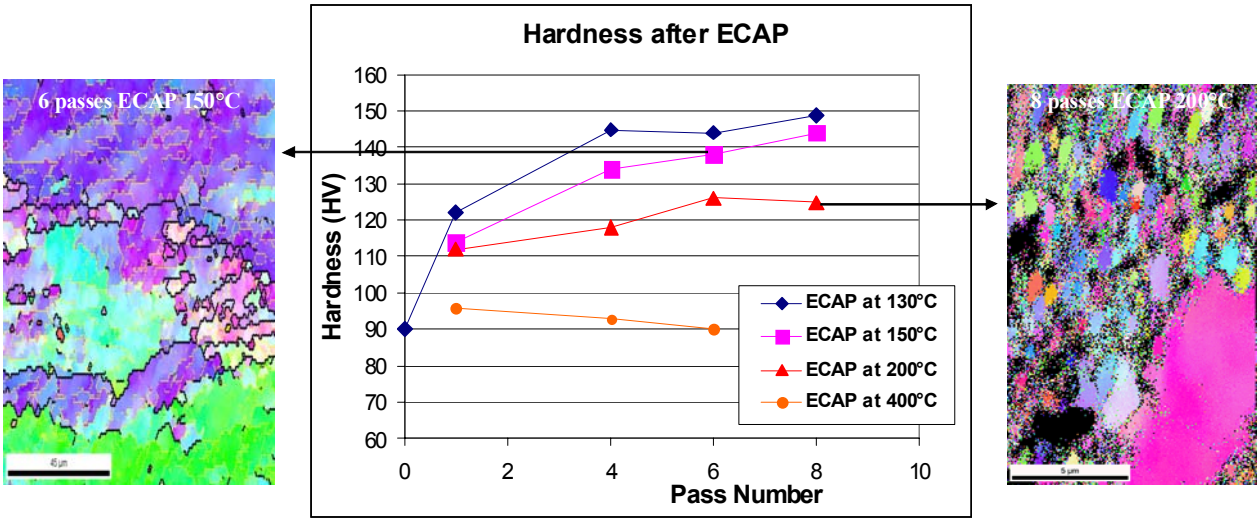

Figure A.8.1: Hardness of cylindrical ECAP samples after various ECAP passes at different temperatures. Substructure after 6 passes at 150°C (left) and 8 passes at 200°C (right)

TEM investigations have shown that in the first ECAP pass there is an increase of dislocation density inside the structure and the dislocations interact with the fine $Al_3(Sc_xZr_{1-x})$ particles. In the following ECAP passes the dislocations organize themselves into cells and low angle grain boundaries. In the last passes a progressive increase of the misorientation of boundaries and a reduction of (sub)grain size (500 nm – 1 µm) is noticed. Nevertheless a lot of defects are still present in the structure and –as also show by EBSD- some "large" grains remain present.

Optimal ECAP parameters, stability, parameters chosen

Since the ECAP'ed material must be transformed into sheet by rolling, the thermal stability of this material has been investigated. Figure A.8.2 shows the hardness evolution of ECAP blocks, produced at 175°C, 200°C and 225°C and annealed at the same temperature. At 175°C the materials is thermally stable for at least 1h. At

200°C and 225°C a small decrease in hardness can be observed (about 10% after 1h).

Based on these results, it was decided to use 200°C as the processing temperature for ECAP.

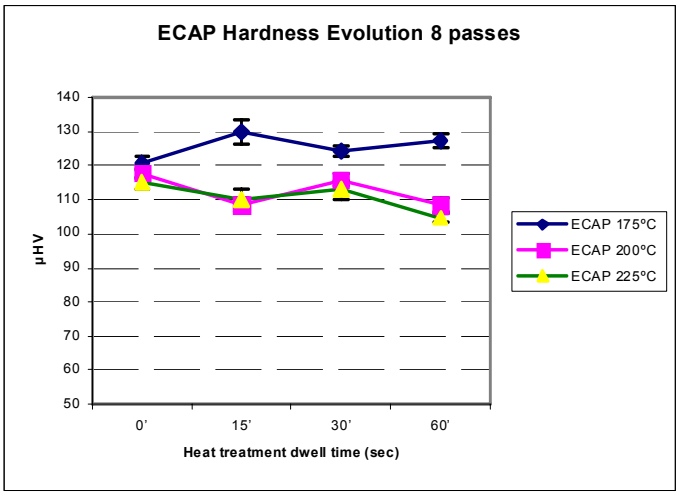

Figure A.8.2: Thermal stability of samples ECAP'ed at 175°C, 200°C and 225 °C and annealed at the same temperature

9. As Received bulk (7.2 mm)

Microstructure and thermal stability

The microstructure of the AR hot rolled plate of 7.2 mm thickness consists of pancake-shaped grains, just like in the 30 mm plate, but the average thickness of the grains is reduced to 2 – 10 µm (vs. 8 - 20 µm in the 30 mm plate). The hardness of the 7.2 mm plate is 108 Hv (vs. 76 Hv for the 30 mm plate). This shows that during hot rolling from 30 mm to 7.2 mm hardly any recrystallisation or grain growth has occurred.

On TEM scale the same "big" dispersoïds as in the 30 mm plate were found ("Si", "Sc+Zr" and "Mn+Fe") as well as the nanosized coherent $Al_3(Sc_xZr_{1-x})$ particles of the LI_2 structure. The latter are very stable; the mean size in the 7.2 mm plate is 8.7 nm vs 9.2 nm in the 30 mm plate.

The thermal stability of this AR material is shown in Figure A.9.1. At 350°C the material is completely stable, even after 24 hours of annealing. However, after 1h at 450°C a drop in hardness of about 10% is noticed.

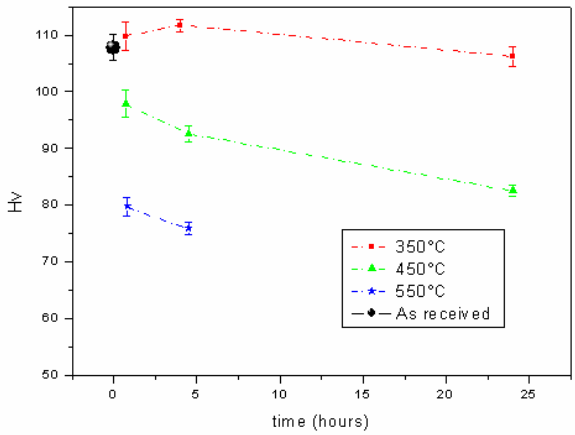

Figure A.9.1: Thermal stability of the AR 7.2 mm thick plate

10. As Received bulk (7.2 mm) + ECAP process (plate)

ECAP parameters

The few rectangular ECAP samples that were successfully extruded (cfr. "Process description"), were obtained under the following conditions: Test speed = 5 mm/min, temperature 200°C, Lubricant = MOLYDUVAL (MoS_2) and both Route A (without rotation) and route C (180° rotation after each pass), have been used. In general the surface markings were more severe on the route A samples.

Microstructure (EBSD)

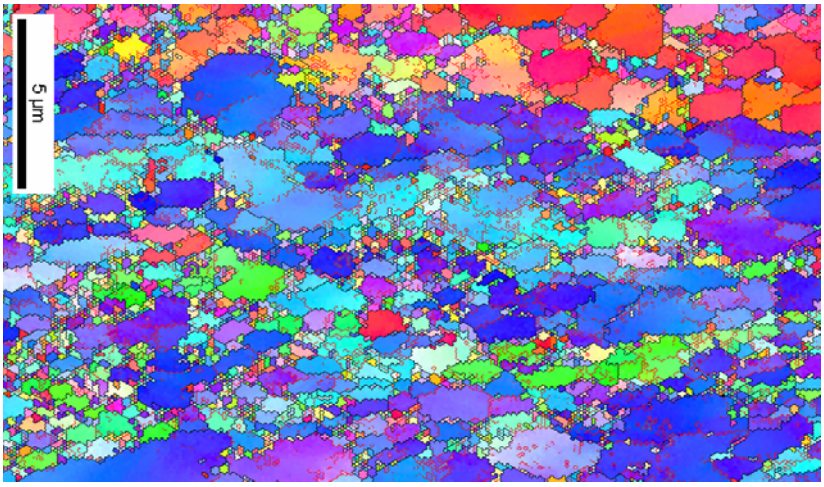

Figure A.10.1: Transverse section of a rectangular ECAP sample after 8 passes at 200°C (route C)

After 8 ECAP passes at 200°C the structure of the extruded blocks is rather homogeneous (Figure A.10.1), but the grain subdivision has not yet reached a point where the majority of the grains have reached the submicron state. The long bands of grains with nearly equal colour (orientation) indicate that still a high fraction of low angle boundaries is present.

11. As Received bulk (7.2 mm) + ECAP process (plate) + Cold rolling

Cold rolling process description

As for the I-ECAP'ed bars, additional conventional cold rolling of the ECAP'ed plates were needed before mechanical characterisation. Different rolling schemas (different number of passes, different temperatures in a range between room temperature and 175°C) were used. Some deep macro-cracks after ECAP process lead to even deeper and longer cracks during cold rolling. Thus, no specimen for mechanical testing was obtained.

12. As Received bulk (7.2 mm) + Asymmetric cold rolling

Asymmetric cold rolling process description

1. Model description:

The CRM model of rolling is based on the slab method which is a convenient way to compute the pressure distribution along the work rolls. This method is accurate if the stresses are mainly function of a specific direction in the forming operation. In this method, a discretization of the domain in thin vertical slices is performed along this extended direction, namely the rolling direction. A sketch of the asymmetric rolling is given in Figure A.12.1.

Since the material flow can be considered as plane and incompressible in the case of sheet rolling, the reduction of height of a slice must be compensated by an increase of the local velocity. As a consequence, three zones can be identified within the roll gap, namely the zones A and C where the two rolls have both higher and lower speed than the strip respectively, and the shearing zone B where the strip velocity is intermediate between the two rolls. The continuity of the flow is also true at the two neutral points where the rolls and the strip have the same speed:

$$v_1 . h_{1n} = v_2 . h_{2n}$$

The basic equation of the slab method translates the static equilibrium of the slices in the rolling direction (Figure A.12.2).

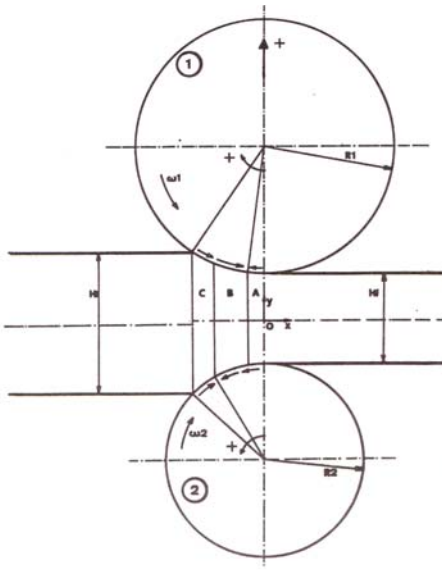

Figure A.12.1: Asymmetric rolling

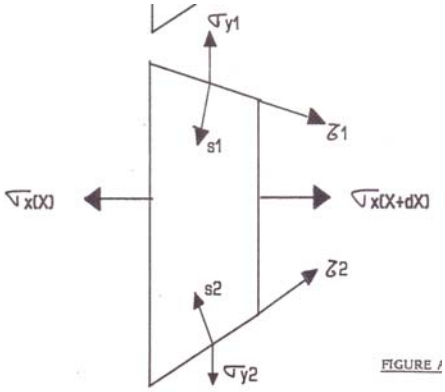

Figure A.12.2: Static equilibrium of a slice in the rolling direction

The static equilibrium of a vertical slice can be written:

$$dF_x = d(\sigma_x.h) = \left[\sigma_y.(\tan\theta_1 + \tan\theta_2) \pm (\tau_1 \pm \tau_2)\right].dx$$

θ represents the slope of the roll strip interface and the +/- signs are function of the zone considered: A, B or C.

The value of the friction stress τ at the roll strip interface is given by a mixed friction law:

$\tau = \mu.\sigma_y$ If $< k_s = \sigma_e / \sqrt{3}$ (Sliding)

$\tau = k_s$ Else (Sticking)

There remain two unknowns in this equation, the horizontal and vertical stresses. An additional relationship is given by the Von-Mises yield criterion in the case of a plane flow:

$$(\sigma_x - \sigma_y) + 4\tau^2 = \frac{4}{3}\cdot\sigma_e^2$$

In a first approach τ_z is assumed to play no role in the plasticity of the slab, a hypothesis which has to be verified in the future.

This equation set can be numerically resolved to compute the pressure distribution along the rolls. The result of such computation for constant yield strength of 100 MPa and a friction coefficient of 0.25 is given in Figure A.12.3.

The location of the two neutral points corresponds to the two kinks in the slope of the friction hill curve. An interesting simulation concerns the effect of varying the roll speed ratio on the two roll torques (Figure A.12.4).

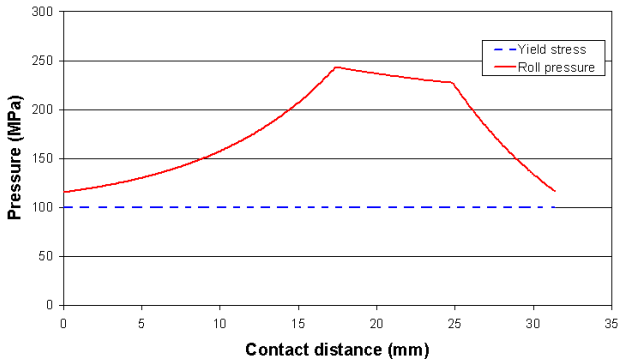

Figure A.12.3: Pressure distribution along the contact length

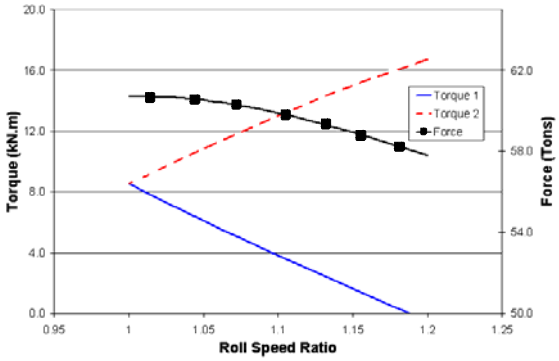

Figure A.12.4: Torque and Force with Roll Speed Ratio

It can be seen that a speed ratio of 1.18 leads to the situation of single drive rolling where one roll is completely free. From an experimental point of view, this single drive approach can be easily put in practice through the removal of one of the two drive arms.

2. Input of strain hardening behavior of AlMgSc

Some plain strain compression tests were performed on AR material with a thickness of 7.2 mm to measure its strain-hardening behaviour $\theta = d\sigma/d\varepsilon$. It could afterwards input in the so-developed model of rolling developed in CRM. The compression curves for different friction coefficients are displayed in the following picture (Figure A.12.5).

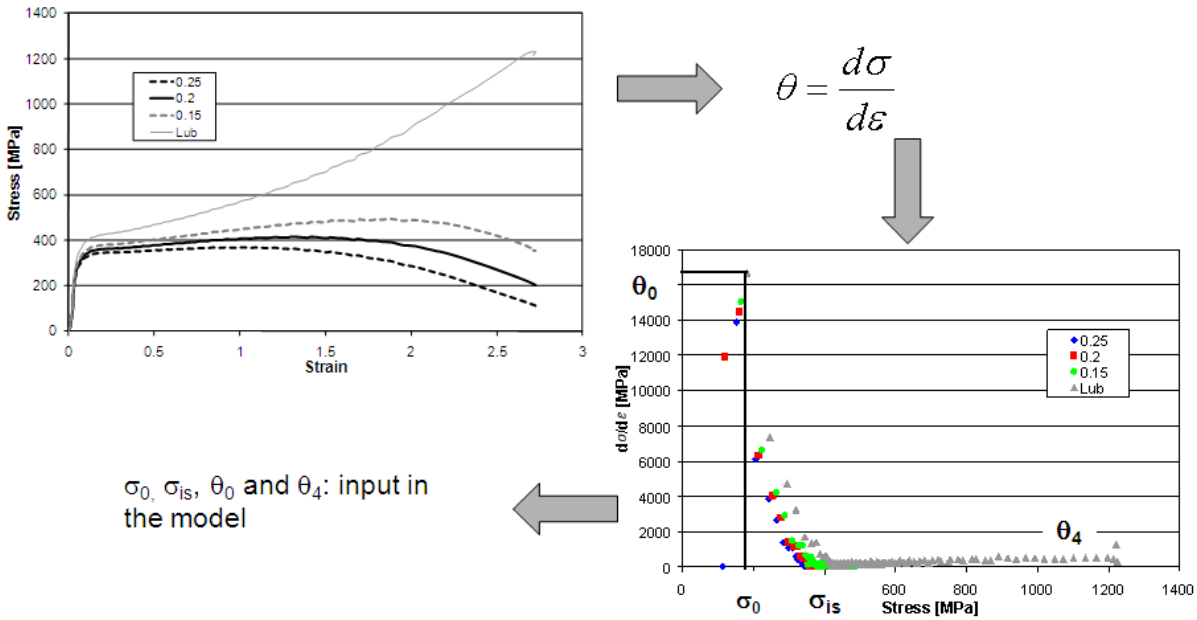

Figure A.12.5: Compression curves of AR material for different friction coefficients to obtain its strain hardening behavior

The measured indicators of the strain hardening (σ_0, σ_4, θ_0 and θ_4) were input in the asymmetric rolling model.

3. Deformation during rolling

For an incompressible plane flow, the displacement field can be described from the relative positions of material points located on the streamlines. Figure A.12.6 illustrates the deformation of two initially orthogonal fibres delimited by three points located on the adjacent streamlines SL1 and SL2, as well as the corresponding transformation of a circular disk of unit radius into an ellipse. Local orthogonal axes (*s*, *n*) may be chosen such that the unit vector *s* is parallel to SL1 and *n* is normal to *s*. Imagining these axes attached to a material point as it passes along SL1, the direction *s* remains fixed with respect to adjacent material points originally aligned in the *x* direction along the flow line, while *n* rotates with respect to material points originally along the *y* axis.

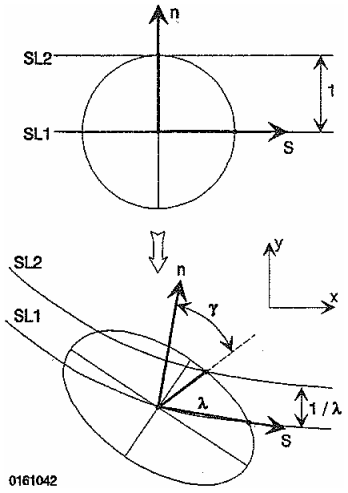

Figure A.12.6: Plane deformation of an initially circulator disk and evolution of the relative positions of three material points

The convenience of these local axes is the simplicity of the description of the displacement field in such references frame:

$$F = \begin{vmatrix} \lambda & \gamma & 0 \\ 0 & 1/\lambda & 0 \\ 0 & 0 & 1 \end{vmatrix} \qquad \textit{(Eq. A.12.1)}$$

The three real positive principal values of the symmetric tensor $F^T F$ are obtained from the characteristic equation:

$$(F^T F - p\, I) = 0 \qquad \textit{(Eq. A.12.2)}$$

By noting

$$F^T F = \begin{vmatrix} f_{11} & f_{12} & 0 \\ f_{12} & f_{22} & 0 \\ 0 & 0 & 1 \end{vmatrix} = \begin{vmatrix} \lambda^2 & \lambda\gamma & 0 \\ \lambda\gamma & \gamma^2 + 1/\lambda^2 & 0 \\ 0 & 0 & 1 \end{vmatrix} \qquad \textit{(Eq. A.12.3)}$$

The characteristic equation can be rewritten:

$$(1-p)\cdot\left(p^2 - \left(\frac{f_{11}+f_{22}}{I_1}\right)p + \left(\frac{f_{11}f_{22}-f_{12}^2}{I_2}\right)\right) = 0 \qquad \textit{(Eq. A.12.4)}$$

Where I_1 and I_2 are independent of the reference basis chosen and thus constitute invariants with respect to translation and rotation transformations.

A first root of (Eq. A.12.4) is $p_1=0$, while the others two roots p_2 and p_3 are related to the length *a* and *b* of the two principal axes of the ellipse (Figure A.12.6) whose equation reduced to its canonical form is:

$$\frac{x^2}{a^2} + \frac{y^2}{b^2} = 1 \qquad \textit{(Eq. A.12.5)}$$

with $$a^2 = \frac{1}{p_2} \qquad b^2 = \frac{1}{p_3}$$

The invariant I2 equals the product of the principal values p_2 and p_3, and is thus linked to the ellipse area which has to remain constant during deformation owing to the incompressibility of the plane flow. Starting from a circle of unit radius, this product equals 1 and the two eigenvalues:

$$p_2 = \left(\frac{I_1}{2}\right) + \sqrt{\left(\frac{I_1}{2}\right)^2 - 1} = \frac{1}{2}\left(\sqrt{\left(\frac{I_1}{2}\right)+1} + \sqrt{\left(\frac{I_1}{2}\right)-1}\right)^2 \qquad \textit{(Eq. A.12.6)}$$

$$p_3 = \left(\frac{I_1}{2}\right) - \sqrt{\left(\frac{I_1}{2}\right)^2 - 1} = \frac{1}{2}\left(\sqrt{\left(\frac{I_1}{2}\right)+1} - \sqrt{\left(\frac{I_1}{2}\right)-1}\right)^2 \qquad \textit{(Eq. A.12.7)}$$

lead to the following stretches:

$$a = \sqrt{\frac{I_1}{4} + \frac{1}{2}} + \sqrt{\frac{I_1}{4} - \frac{1}{2}} \qquad \textit{(Eq. A.12.8)}$$

$$b = \sqrt{\frac{I_1}{4} + \frac{1}{2}} - \sqrt{\frac{I_1}{4} - \frac{1}{2}} \qquad \text{(Eq. A.12.9)}$$

of the material fibres along the large and the small axes of the ellipse obtained after a finite plane deformation has been applied to a circle.

In the configuration of asymmetric rolling, the Von Mises deformation is equal to:

$$\varepsilon_{VM} = \frac{2}{\sqrt{3}} \ln a \qquad \textit{(Eq. A.12.10)}$$

with $$I_1 = \lambda^2 + \gamma^2 + \frac{1}{\lambda^2}$$

The Von Mises deformation was the variable parameter used for the asymmetric rolling.

4. Asymmetric cold rolling trials with different deformation routes

To induce different redundant shearing values, three asymmetric cold rolling schemas were chosen in a dual drive configuration (Figure A.12.7). After each pass, the sheet was turned 90° from the rolling direction.

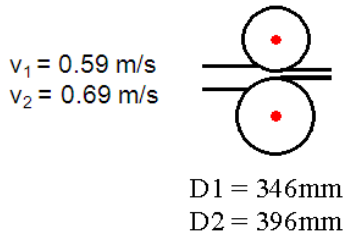

Figure A.12.7: Rolling configuration for the asymmetric trials

a- Configuration with a constant stretch ratio λ ($\lambda = e_0/e_f = 1.4$) for each pass.

The rolling trials were done in four passes (7.2 - 5.5 – 4 - 2.75 - 2 mm)

b- Configuration with a constant shear strain γ ($\gamma = 0.85$) for each pass.

The shear strain is obtained through the relationship:

$$\gamma = \frac{v_s \Delta t}{e_f} \qquad \textit{(Eq. A.12.11)}$$

with Δt the difference of the contact time of each neutral point on the roll, v_s the strip velocity at the exit of the rolling gap and e_f the final thickness.

The rolling trials were also done in four passes (7.2 -4.8 - 3.5 - 2.5 - 2 mm).

c- Configuration with a strain increase due to shearing/mm of plane reduction [%/mm] is maximum.

In this configuration the number of passes could be increased. Thus, seven passes were done (7.2 - 5.8 - 4.9 - 4.2 - 3.9 - 3.4 – 3 - 2.6 mm).

Afterwards, mechanical characterisation by means of tensile tests on A25 specimen was performed. Three samples were taken out of the sheet in the rolling direction of the last pass, and three transversal to this rolling direction. A mean value of the tensile properties including the two directions was calculated. The results are presented in Figure A.12.8.

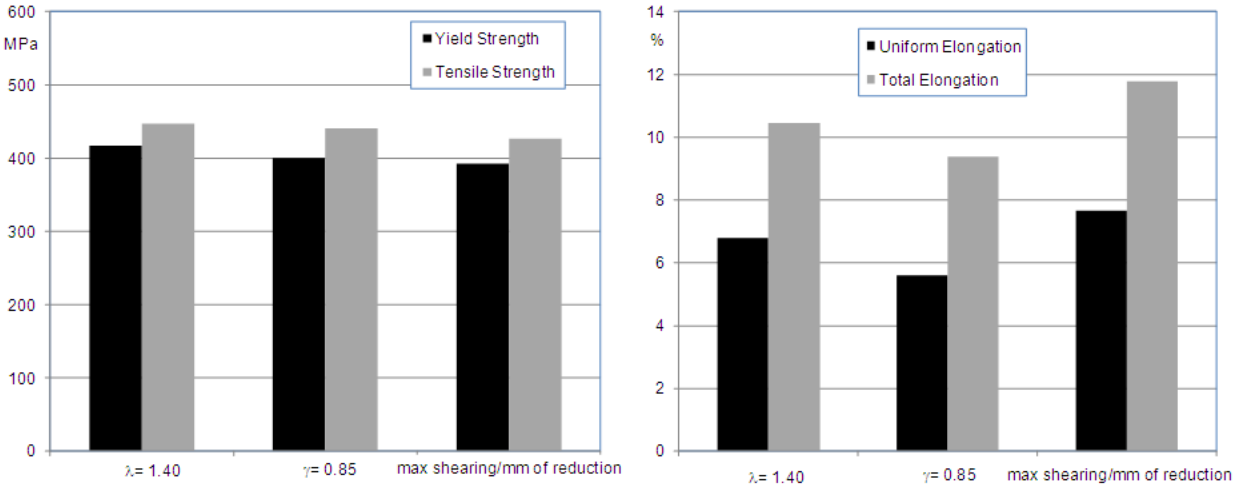

Figure A.12.8: Tensile properties after asymmetric rolling with different stretch ratio values

The yield strength and tensile strength are slightly decreasing between configuration 1 (left on the left chart) and configuration 3 (right on the left chart), due to a decrease of the stretch ratio.

The uniform and total elongations are higher under the configuration with a low stretch ratio. The deviation of the elongation values does not lead to clear conclusion.

5. Asymmetric cold rolling trials with different rolling configurations

This set of trials was performed to study the effect on the microstructure of a strong difference between the diameters of the upper roll and the lower roll. Three different configurations were chosen (Figure A.12.9). The preliminary conventional rolling was applied in configurations two and three to avoid an early bending of the sheet during the first passes, bending mainly due to the difference of the roll diameters.

Mechanical characterisation by means of tensile tests on A25 specimen was performed. Three samples were taken in the rolling direction and three in the transversal direction. For the configuration 1, no sample could be taken in the rolling direction, as the bending was too extreme. The results are displayed in Figure A.12.10.

The configuration with the higher final thickness (configuration 1) shows lower yield strength and tensile strength and higher elongations due to a lower deformation. Between configurations 2 and 3, no significant change in the tensile properties was observed. A kind of isotropy for both configurations is additionally obtained.

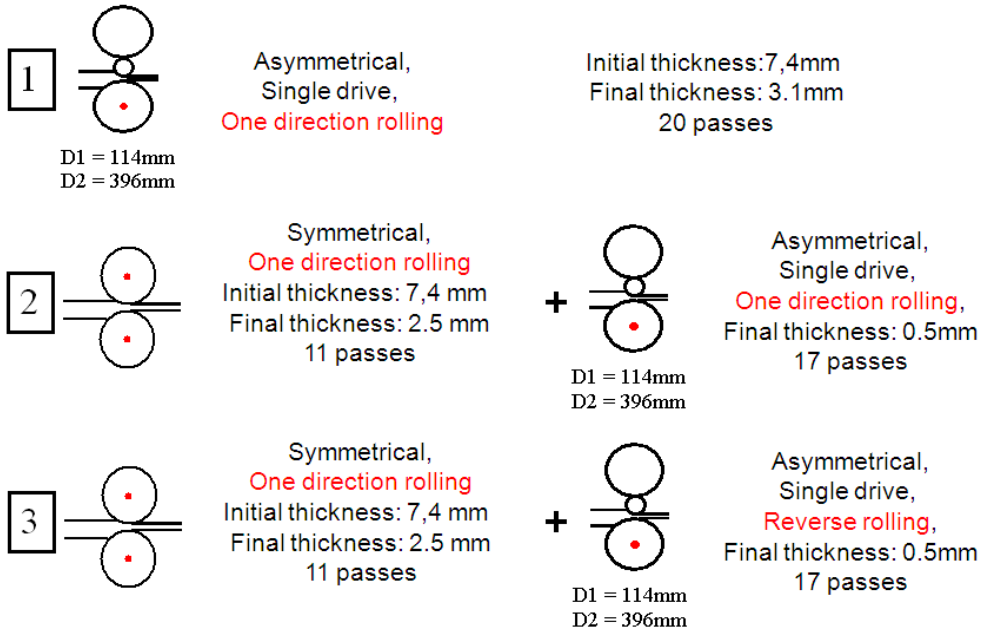

Figure A.12.9: Asymmetric rolling trials with different roll diameters, lower roll driven

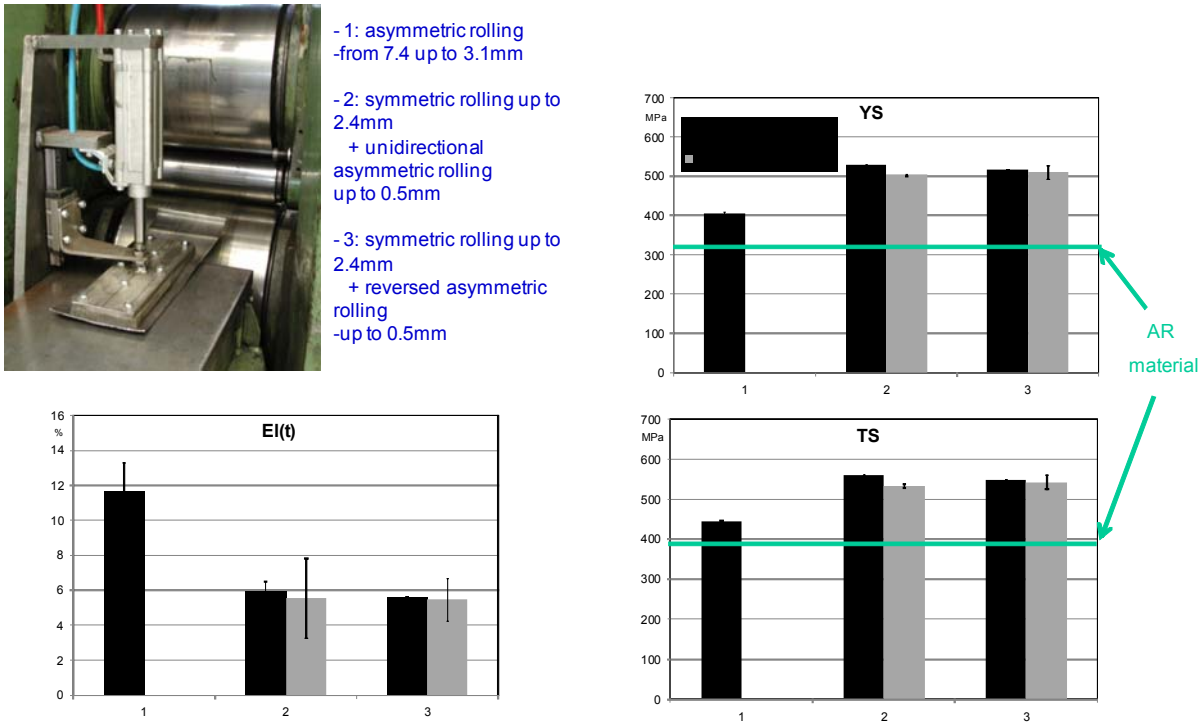

Figure A.12.10: Tensile properties after asymmetric rolling trials with different roll diameters

Microstructure

As it was often the case in this project, it was very difficult to obtain good EBSD scans of cold deformed AlMgSc samples. Figure A.12.11 shows an image of the microstructure after asymmetric rolling. Although only part of the grains have been indexed by the EBSD software, it is clear that rather large grains, elongated in the rolling direction, are still present and the desired submicron structure has not been obtained.

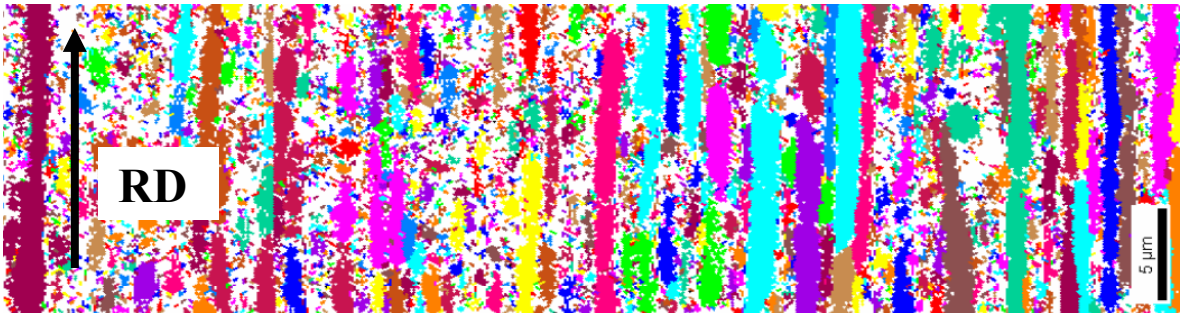

Fig A.12.11: EBSD scan of an asymmetric rolled sample

Process comparison

The three following processes are compared:

- Asymmetric cold rolling (ACR sheet)
- I-ECAP process (bar - sheet)
- ECAP process (plate)

1. Microstructure evolution due to the process

In this project 4 processes have been used to obtain submicron grains. For various reasons, described above, none of these processes has yielded a homogeneous, submicron-grained material. The process of grain splitting that takes place in all 4 processes due to the applied severe plastic deformation, seems to be slower in the studied Al-Mg-Sc alloy than in CP Aluminium or in other metals.

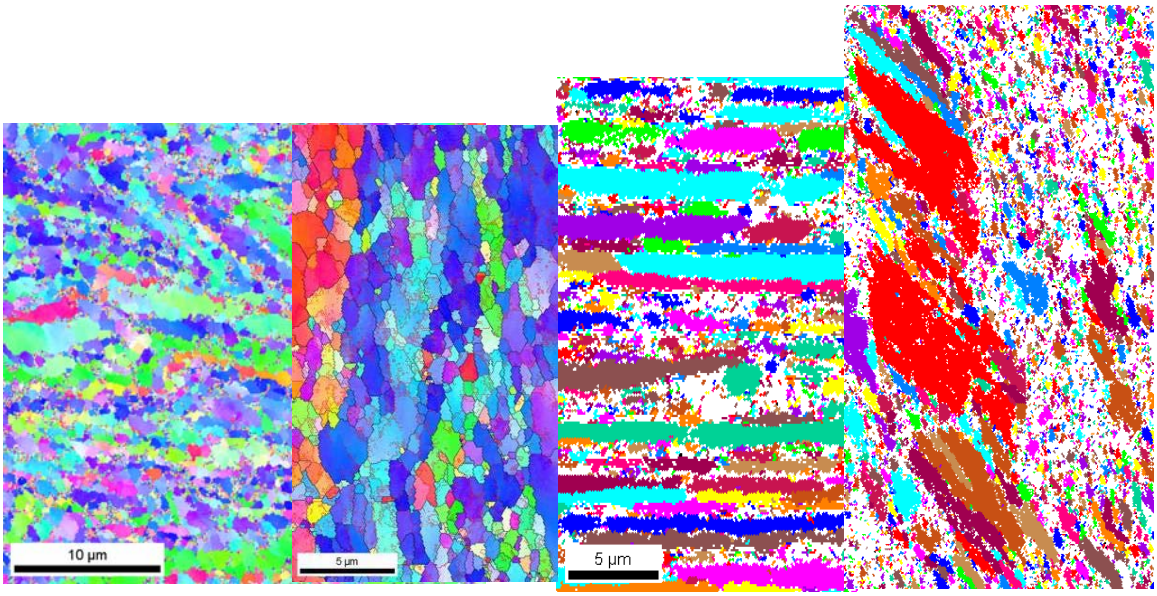

I-ECAP sheet ECAP block Asymmetric Rolling I-ECAP on bar

Figure B.1.1: Overview of the microstructure obtained after various methods of severe plastic deformation, applied on a Al-Mg-Sc alloy

Figure B.1.1 gives an overview of the obtained microstructures. Asymmetric rolling yields a very fibrous structure with long elongated grains without internal subdivision. The bar obtained after 6 passes of Incremental ECAP shows a very inhomogeneous structure. Large parts of “old” grains are still present. The badly-indexed part of this sample could have a finer structure, but this should be verified with TEM. The ECAP block is relatively homogeneously subdivided, but the grains – after 8 ECAP passes – are still larger than 1 µm. Finally the sheet obtained with Incremental ECAP has the

finest substructure – with a mean grain size of about 1 µm – but is not completely homogeneous.

2. Superplasticity

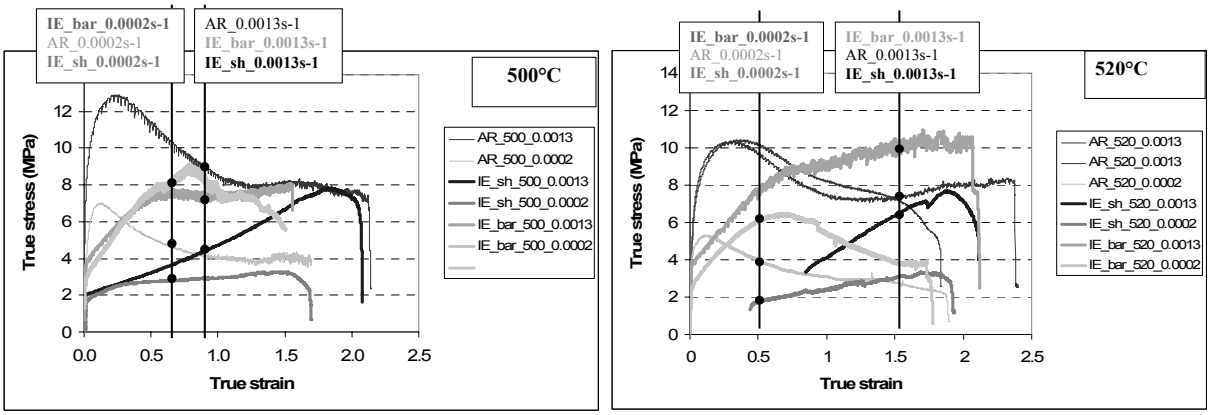

Figures B.1.2 & B.1.3: Superplasticity tests on AR sheets (AR), I-ECAP sheet (IE_sh) and I-ECAP bar (IE_bar) at two levels of strain rate, at 500°C and at 520°C

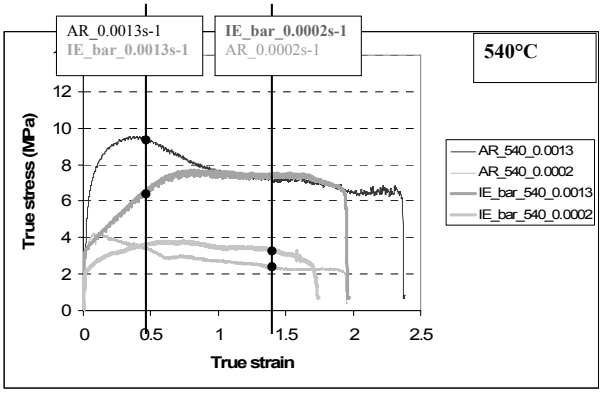

Figures B.1.4: Superplasticity tests on AR sheets (AR), I-ECAP sheet (IE_sh) and I-ECAP bar (IE_bar) at two levels of strain rate and at 540°C

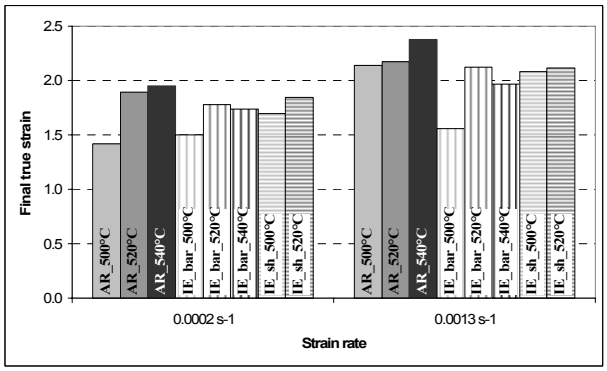

Figures B.1.5: Comparison of the ultimate true strain

	0.0002 s-1			0.0013 s-1		
	500°C	520°C	540 °C	500°C	520°C	540 °C
AR sheets	1.42	1.89	1.95	2.14	2.17	2.38
I_ECAP bars	1.50	1.78	1.74	1.56	2.12	1.97
I_ECAP sheets	1.70	1.85		2.08	2.12	

Table B.1.1: Comparison of the ultimate true strain

Figures B.1.2 to B.1.5 and Table B.1.1 indicate that:

- The superplasticity is kept after I-ECAP process for both bars and sheets.
- The maximum strain is reduced in almost all cases for I-ECAP sheet and bar but these tests should have been repeated to verify this tendency.
- The hardening behaviour is modified by the I-ECAP process.

SPIF – Analytical model

To characterize the applicability of a material for Single Point Incremental Forming the forming limits for this material have to be determined. Forming limits can be categorized in geometrical limits imposed by the part itself and machine limits enforced by the range and strength of the available machines.

For a given material and thickness a maximum drawing angle can be determined. This represents the geometrical limits of the conventional incremental forming process. A range of parts with different wall angles has to be made until the maximum angle is reached.

An accurate analytical model for the forming forces aides to determine the feasibility of making a part on a specific machine. The machines used in within the framework of this project are restricted to a maximum 2000 N. Preliminary studies showed the original thickness (3.2 mm) of the As Received material would be out of machine limits. This means the material had to be cold rolled and annealed to a thickness for which the forming forces would be within machine limits.

1. Maximum forming angle

Determining the geometrical forming limits defined by the maximum draw angle in Single Point Incremental Forming is done by means of a standardized cup test (Figure C.1.1). In it a series of cups are formed, where the wall angle of each cup is greater than that of the preceding cup. The forming limit is the angle at which the sheet fractures.

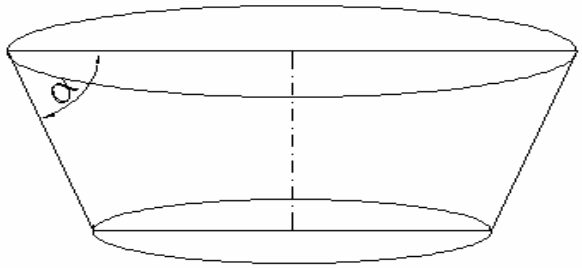

Fig C.1.1: Standardized cup test

The maximum drawing angle is mainly influenced by the thickness of the initial blank sheet. To a lesser degree the diameter of the spherically tipped tool and the scallop

height affect the drawing angle in a negative way, where the scallop height is specified as the height of the ripple between two passes of the forming tool.

Forming limit tests typically start with the formation of a cup with a 10° wall angle. Each successive cup has a wall angle that is 10° greater. After this initial exploratory study a finer search is done to an accuracy of 1°.

Tensile tests of the As Received material (2.3 mm) revealed the necessity to decrease the thickness of the initial material to limit the forming forces. Cold rolling + annealing was chosen as means to reduce the thickness and maintain similar mechanical properties as the initial sheets.

To determine the optimal reduction of the As Received material preliminary tests were conducted on a material with similar mechanical properties. Sonaca suggested and provided AA2024 T3 as a material for preliminary testing. In this paragraph the results will be reported for both AA2024 T3 and the As Received material + cold rolling + annealing (further spoken of as AlMgSc) (Table C.1.1).

Performed tests

Material	Thickness	Ø tool	Scallop	α
AA 2024 T3	1	10	0.005	42 °
AA 2024 T3	0.4	10	0.005	38 °
Al-Mg-Sc	0.5	10	0.005	46°

Table C.1.1: Material tested and maximum forming angle

In earlier studies a range of materials were tested in a similar fashion. To compare the formability of AlMgSc to other common materials a table (Table C.1.2) is included with results for Al 3003 O, DC 01, AA 5086-H111 and AISI 304.

Other materials

Material	Thickness	Ø tool	Scallop height	α
Al 3003 O	0.85	10	0.005	70°
DC 01	1	10	0.005	67 °
AA 5086-H111	0.8	10	0.005	62 °
AISI 304	0.4	10	0.005	63 °

Table C.1.2: Material tested previously and maximum forming angle

Comparing the different materials reveals a fairly low forming limit for AlMgSc. This is a strong limiting factor in the amount of geometries which can be made in this material. Earlier studies show that performing Incremental forming at elevated temperatures will improve forming limits by a few degrees.

2. Force prediction

An accurate prediction of forming forces in SPIF for a certain material helps in determining the necessary strength of forming equipment. For this prediction both SPIF-platforms at PMA were fitted with a dedicated force measuring device which recorded 3 Cartesian force components Fx, Fy and Fz.

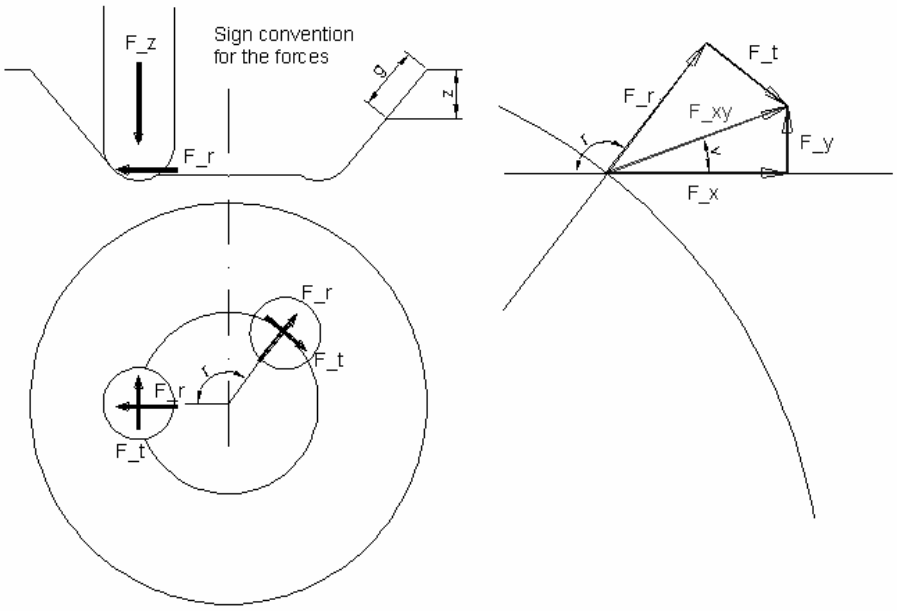

Figure C.2.1: Force components

Similar to the determination of the geometrical forming limits a cone is usually the geometry on which a force prediction model is based. This shape has the advantage that the tool encounters virtually constant forming conditions along the toolpath within one contour.

Determining forming forces in a cone is done using the axial tool force (Fz), the radial force (Fr) perpendicular to the tool progression and the tangential force parallel to the tool progression (Ft). This means the measured Fx and Fy have to be recalculated to obtain the tangential and radial force. Contrary to Fx and Fz which fluctuate along the circular contour af a cone, Fr and Ft will remain constant within one contour of the toolpath (Figure C.2.1).

3. Angle sensitivity

Earlier research on forces in SPIF has revealed the important and complex non linear influence of the draw angle on the forming forces. Because of this irregular behaviour a more in-depth study is done towards this influence.

The analysis was performed using a set of cones similar to the cones used for the forming limit analysis. While forming a set of cones with draw angle between 10 and 46 degrees forces were measured and computed.

As stated earlier in the report all tests were initially performed on AA 2024-T3, as a material with similar mechanical properties, to accurately determine the optimal thickness reduction factor for the As Received AlMgSc (3.2 mm). The results for these tests will also be stated in this report.

The tests for AA2024 (Figure C.3.1) were done using following process parameters:

- Material: AA 2024 T3
- Tool diameter (Td) = 10 mm
- Drawing angle (α) = 10 – 20 – 30 – 40 – 41 - 42(°)
- Cone base : Ø 180 mm
- Scallop height (Δ h) = 0.005 mm
- Initial sheet thickness (t) = 0.4 mm

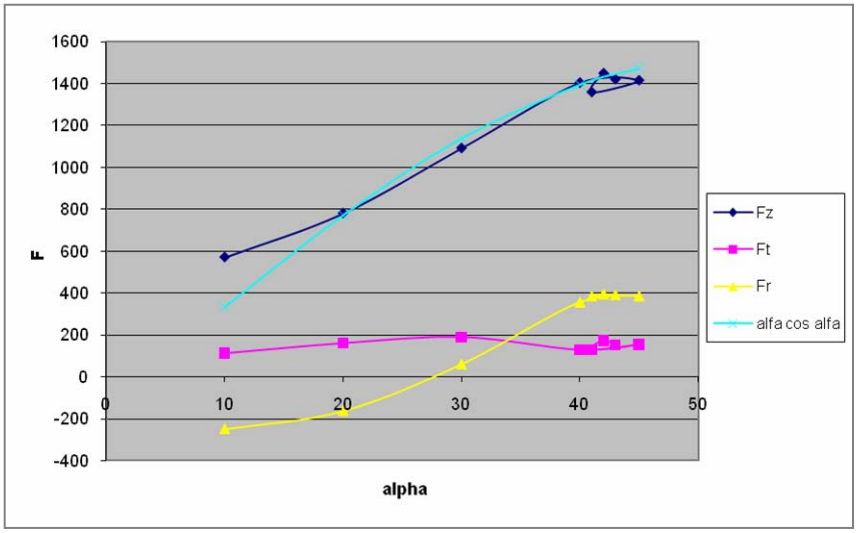

Figure C.3.1: AA2024: Force components for different wall angle

The tests for AlMgSc (Figure C.3.2) were done using following process parameters:

- Material: As Received (3.2 mm) + cold rolling (0.5 mm) + annealing
- Tool diameter (Td) = 10 mm
- Drawing angle (α) = 10 – 20 – 30 – 40 – 45 - 46(°)
- Cone base : Ø 180 mm
- Scallop height (Δ h) = 0.005 mm
- Initial sheet thickness (t) = 0.5 mm

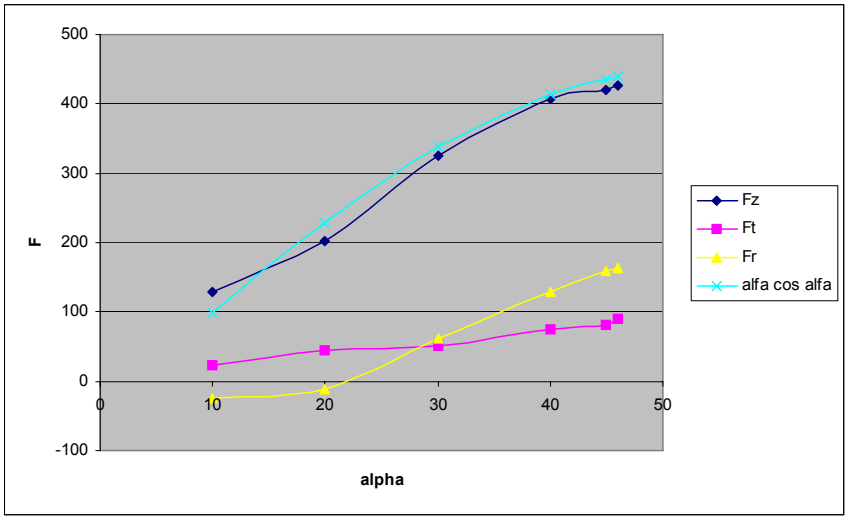

Figure C.3.2: AlMgSc: Force components for different wall angle

It is clearly visible that Fz is the dominating force component in the SPIF process. Also the non linearity is visible. When plotting the function α .cos(α) with an appropriate scale factor in the same graph a close approximation can be observed, which gives a good representation of the influence profile.

Force model

Other parameters that are influential on the forces have a less complex behaviour and can therefore be studied using factorial analysis. The parameters found to be determining for the forces at play are: tool diameter (t_d), scallop height (Δ h), sheet thickness (t) and draw angle (α).

To find regression formulas for the force prediction model a factorial analysis was done varying all influential parameters between two values.

The values chosen for AA2024 T3 were:

- Wall angle: 20 - 35°
- Tool diameter: 10 – 20 mm
- Scallop height: 0.005 – 0.015 mm
- Thickness of material: 0.4 – 1 mm

The regression formula obtained for the axial force component:

$$F_Z \approx t^{1.442}\, d_t^{0.664}\, \Delta h^{0.09}\, \alpha^{1.12}\, \cos\alpha \ldots \qquad \text{(Eq. C.3.1)}$$

The values chosen for AlMgSc were:

- Wall angle: 20 - 40°
- Tool diameter: 10 – 15 mm
- Scallop height: 0.005 – 0.015 mm
- Thickness of material: 0.5 – 1 mm

The regression formula obtained for the axial force component:

$$F_Z \approx t^{1.48}\, d_t^{0.767}\, \Delta h^{0.1}\, \alpha^{1.11}\, \cos\alpha \ldots \qquad \text{(Eq. C.3.2)}$$

Earlier testing of other materials reviled following regression formulas:

AA3003	$F_Z \approx t^{1.58}\, d_t^{0.35}\, \Delta h^{0.09}\, \alpha \cos\alpha \ldots$
AlMg3	$F_Z \approx t^{1.72}\, d_t^{0.40}\, \Delta h^{0.08}\, \alpha \cos\alpha \ldots$
DC01	$F_Z \approx t^{1.35}\, d_t^{0.48}\, \Delta h^{0.12}\, \alpha^{1.11}\, \cos\alpha \ldots$
AISI 304	$F_Z \approx t^{1.61}\, d_t^{0.42}\, \Delta h^{0.08}\, \alpha^{0.99} \ldots$

Table C.3.1: Regression formulas

In order to avoid having to study each new material meticulously before using it a generalized formula applicable for a wide variety of materials would be beneficial.

Using a common set of parameters for the different materials, the corresponding "reference" force Fz was computed for each material. The common settings are:

- Wall angle: 40°
- Tool diameter: 15 mm
- Scallop height: 0.01 mm
- Thickness of material: 0.9 mm

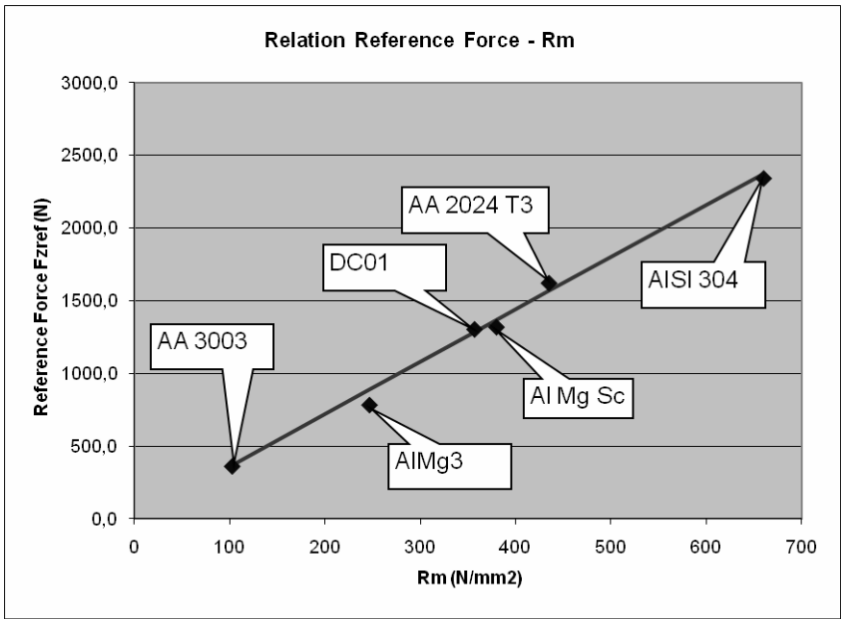

Figure C.3.3: Relation Force – Tensile strength

A simple proportionality can be observed between the "reference force" Fz_{ref} and the tensile strength Rm (Figure C.3.3). This can be expressed as follows:

$$F_{Z\,ref}\,(N) = 3.6\,R_m\,(N/mm^2) \qquad \text{(Eq. C.3.3)}$$

Since the influence exponents of the parameters in the regression formulas show a limited spread, a generalized formula using averaged exponents can be considered:

$$F_Z \approx t^{1.53}\,d_t^{0.51}\,\Delta h^{0.093}\,\alpha^{1.055}\,cos\alpha\,... \qquad \text{(Eq. C.3.4)}$$

Using previous formulas an approximate generalized formula can be obtained which allows predicting the axial force for any material based on the tensile strength:

$$F_Z = 0.0562\,R_m\,t^{1.53}\,d_t^{0.51}\,\Delta h^{0.093}\,\alpha^{1.055}\,cos\alpha\,... \qquad \text{(Eq. C.3.5)}$$

This formula gives a good estimation for a certain set of parameters for any given material.

SPIF – Numerical model improvement

1. Remeshing

Simulating the SPIF process is a complex task. First, the tool diameter is small compared to the size of the sheet metal. Moreover, during its displacement, the tool deforms almost every part of the sheet, which implies that small elements are required everywhere. The computation time is too high when using implicit method. The use of three dimensional 4 node shell elements can drop the computation time but it remains too high. That's why it has been decided to develop the adaptive remeshing in the Lagamine code. The tool motion is so important, that the chosen method to remesh is refinement and derefinement.

Refinement criterion

The criterion of the adapted remeshing depends on the distance with the tool. The elements in the "tool neighborhood" are refined in new fine elements. If the tool is farther from a refined element, then the new elements are removed and the old element is reactivated. However if the distortion is too important in this zone the old element remains refined to avoid losing accuracy of the solution. The "tool neighborhood" size is defined by the user.

Element refinement

The refinement of the element is structural. The coarse elements which respect the refinement criterion are deactivated and become a cell of smaller elements. Each coarse element is divided into the same number of fine elements. This number is defined by the user. The transfer of the stresses and state variables from the coarse element to the fine element is performed by interpolation, where the method is described in [7].

New nodes

The position and velocity of the new nodes are computed by interpolation with the old nodes. As the refinement does not take into account the transition zone between coarse and fine elements, then there are three types of nodes: old nodes, free new nodes and constrained new nodes. The constrained nodes enable to save the compatibility of the mesh. The degree of freedom of the constrained nodes depends on the degree of freedom of two master nodes. These dependence causes modification in the out-of-balanced force and the tangent stiffness matrix.

New data storage method

In computer science, a linked list is a data structure. It consists of a sequence of objects, each containing arbitrary data fields and one reference (“link") pointing to the next object. The principal benefit of a linked list compared with a conventional array is that the order of the linked items may be different from the order used to store the data in memory or on disk. This property allows the list of items to be read in a different order. Linked lists permit insertion and removal of object at any point in the list on line. During the SPIF process many elements are refined and derefined, so that many cells are created and removed. This data stocking method is interesting to follow the cells and elements.

A cell contains:

- The deactivated coarse element number
- The new nodes table (number, position, velocity, etc)
- The new element table (nodes, stress, state variable, etc)
- The edges in contact or not with another cell list
- The following cell

Dynamic allocation

At the beginning of its development, the Lagamine program language was Fortran 70 and the arrays were stoked in static manner. The remeshing causes the modification of node, element and degree of freedom numbers. Currently the program language is Fortran 90 therefore the dynamic allocation is possible for the arrays. At each step of the computation (equilibrium state after incremental displacement or force), the arrays are reallocated and the linked list input the new generated data (nodes, element and degree of freedom) due to remeshing.

Renumbering

The addition of new nodes can cause an important increasing of the bandwidth of the stiffness matrix; therefore the solving time for the degree of freedom computation can strongly increase. The renumbering of the degrees of freedom of the nodes can tackle this problem. Two methods of renumbering have been implemented: oil stain and directional method.

Validation: Line test simulation

The validation of the new approach is performed on the so-called line test simulation which is a simple SPIF process. A square metal sheet of an aluminium alloy AA3003-

O with a thickness of 1.2 mm is clamped along its edges. The spherical tool radius is 5 mm. The displacement of the tool is composed of five steps with an initial position tangent to the surface of the sheet: a first indent of 5 mm (step1), a line movement at the same depth along the X-axis (step 2), then a second indent up to the depth of 10 mm (step 3) followed by a line at the same depth along the X-axis (step 4) and the unloading (step5).

The elastic range is described by the Hooke's law. For the plastic part, the yield locus, F_{Hill}, is described by Hill'48 law. The hardening equation is described by the Swift law. The material parameters have been identified in [8].

The geometry and the loading are symmetrical about the X-axis, so that only half of the sheet is modelled. Consequently, the displacements and rotations around the X- and Z-axis are fixed for every node along the X-axis. Moreover, the nodes along the edges are fixed to model the clamping of the sheet.

Two types of meshes are performed (see Figure D.1.1). The first mesh is the reference. It is used without adaptive remeshing and contains 884 elements. The second one is used with adaptive remeshing and contains 72 elements. Two refinements have been tested. Every coarse element that needs to be refined is divided into 16 (N=3) and 25 (N=4) new elements.

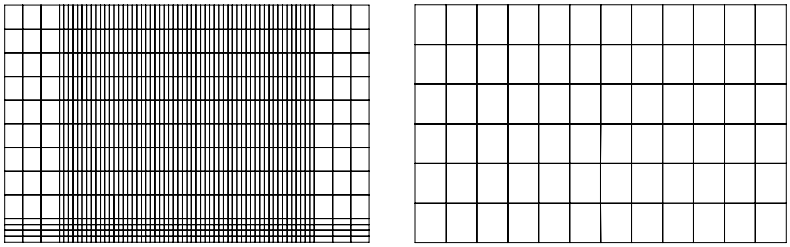

Figure D.1.1: Meshes

Figure D.1.2 shows the evolution of the mesh during the remeshing simulation (N=4). During step 1, only the elements close to the tool are refined. During the other steps, the tool moves further away. Consequently some refined elements are removed but those where the distortion is important remain refined. Finally at the end of the simulation the mesh is fine only where the distortion is high.

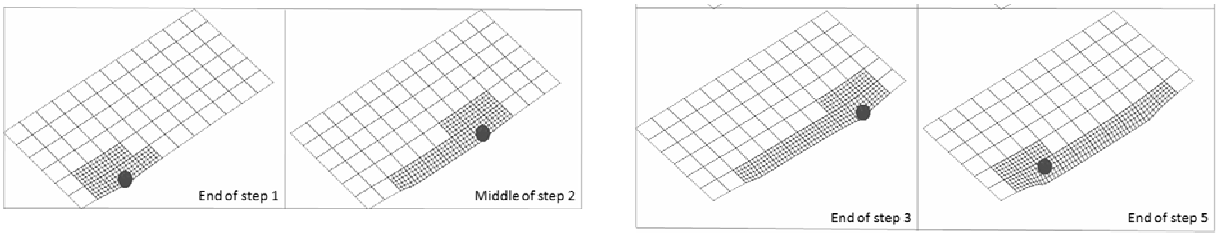

Figure D.1.2: Evolution of the mesh for N=4

The main outputs of the SPIF simulation are the final shape of the sheet and the evolution of the tool force during the simulation Figure D.1.3 shows the final shape of the sheet in a cross-section along the symmetric axis in the middle of the thickness for the reference and the remeshed simulation. Figure D.1.4 shows the evolution of the tool force during the simulations. The results are quite similar. The oscillations of the force are due to the penalty method of the contact. They are higher with remeshing because the mesh used here is coarser than the reference. Table D.1.1 shows the computation time. The N=4 simulation give equivalent results with a shorter simulation. The CPU time of the N=3 simulation is the smallest but the finale shape is less accurate.

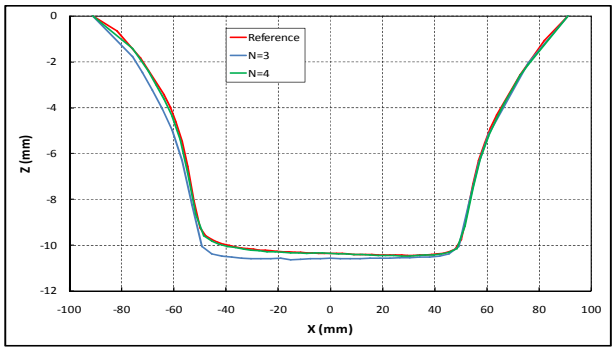

Figure D.1.3: Shape in a cross-section at the end of the line test

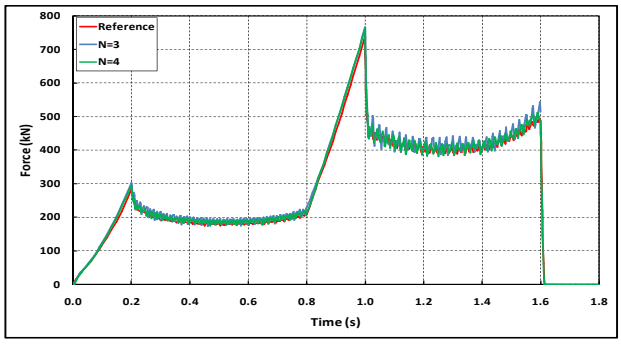

Figure D.1.4: Evolution of tool force during the line test

	Reference	N=3	N=4
CPU	9 min 28 s	3 min 45 s	6m.49s
Number of iterations	2693	2899	3304

Table D.1.1: Computation time results

2. ***Material laws***

The elastic range is described by Hooke's law and the plastic part by the Hill'48 law (Eq. D.2.1) where σ_{ij} are the stress tensor $\underline{\sigma}$ components.

$$F_{HILL}(\underline{\sigma}) = \frac{1}{2}[H(\sigma_{xx} - \sigma_{yy})^2 + G(\sigma_{xx} - \sigma_{zz})^2 + F(\sigma_{yy} - \sigma_{zz})^2 + 2N(\sigma_{xy}^2 + \sigma_{xz}^2 + \sigma_{yz}^2)] - \sigma_F^2 = 0 \quad \text{(Eq. D.2.1)}$$

Isotropic hardening

In the finite element code used, the isotropic hardening can be described either by the Swift law (Eq. D.2.2) or by Voce's law (Eq. D.2.3). Contrarily to the Swift law, the Voce's formulation can reach saturation [9] and is thus better adapted to the high deformation of the SPIF process. This is why this law has been implemented in the code.

$$\sigma_F = K(\varepsilon_0 + \varepsilon^{pl})^n \quad \text{(Eq. D.2.2)}$$

$$\sigma_F = \sigma_0 + K(1 - \exp(-n\varepsilon^{pl})) \quad \text{(Eq. D.2.3)}$$

where ε^{pl} is the equivalent plastic strain and K, ε_0, σ_0, and n are the material parameters.

These models use Green deformations and the second formulation of Piola-Kirchoff for the stresses.

Kinematic hardening

It was noticed that a simple isotropic hardening model is not sufficient to provide an accurate tool force prediction [10]. Therefore an elasto-plastic law with a mixed isotropic-kinematic hardening is used. In this law, the stress tensor $\underline{\sigma}$ in (EQ.D.2.1) is replaced by $(\underline{\sigma} - \underline{X})$, where $\underline{X}$ is the back-stress. The evolution of the back-stress is described by Ziegler's hardening equation (Eq. D.2.4):

$$\dot{\underline{X}} = C_A \frac{1}{\sigma_F}(\underline{\sigma} - \underline{X}).\dot{\varepsilon}^{pl} - G_A.\underline{X}.\dot{\varepsilon}^{pl} \quad \text{(Eq. D.2.4)}$$

where C_A is the initial kinematic hardening modulus and G_A is the rate at which the kinematic hardening modulus decreases with an increasing plastic deformation. This law was not available at the beginning of the project thus it was also implemented.

SPIF – Simulations

1. Material data identification

The inverse method is used to fit material data. This method, coupled with the Finite Element code: "Lagamine" [11], is used to determine several parameters of the complex material laws. The principle of this method is to choose a set of tests the results of which are sensible to the material data to adjust. These tests are simulated using an initial set of data, chosen arbitrarily – the better this initial guess is, the faster the method is. Then, the numerical results are compared with the experimental measurements and, using an optimization algorithm, the material data are iteratively adjusted until a sufficient accuracy is reached.

Two methods are tested and compared to describe the material behavior.

Classical method

For the first set, classical tests described in section "AlMgSc characterisation" in Figures A.1.1 to A.1.7 (in section: "Material characterisation / As Received sheets") are used in the inverse method and the material laws are the ones initially implemented in the code: Hill and the isotropic hardening of Swift law. The tests chosen are a tensile test, a monotonic shear test, a large tensile test, two orthogonal tests (tensile test followed by shear test) at two levels of pre-strain: 4% and 8% and two Bauschinger shear tests at two different levels of pre-strain: Gamma = d/b = 8.8% and 29%.

New improved method

For the second set of data, an additional indent test is used in the inverse method: the first step of the Line test (see section: "AlMgSc characterisation" and Figures A.2.12 and A.2.13) to give the missing information about the out-of-plane material behaviour. Indeed, it is observed [8] that simple classical tests inducing in-plane stresses are not sufficient to describe the material behaviour during the SPIF process. The Voce and Ziegler laws, recently implemented for the SPIF process, are chosen to characterise the material.

Material data

The Young's modulus is obtained by tensile tests (E=70500 MPa). The Poisson ratio could not be defined due to Portevin - Le Chatelier effect, thus its value was fixed equal to 0.33 as for other aluminium alloys.

The parameters F, G, H of the Hill's law and the yield stress σ_F are identified using tensile tests at 0°, 45°, and 90° from the rolling direction (Table E.1.1). The parameter N, the Swift and Voce's laws data and the back stress parameters are fitted by the inverse method.

The first set of data is defined using classical tests only and an isotropic hardening is imposed. The second set (improved data) is fitted using classical tests + indent test. All of the tests are simulated with quadrilateral shell elements with four nodes as well as for the SPIF process simulations.

	Test used	Yield surface coefficients	Swift or Voce parameters	Back stress data (Ziegler)
Set 1: HILL Swift Isotropic	Classical tests	F= 1.11 G= 1.11 H= 0.89 N= 3.53	K= 443 ε_0= 0.00057 n= 0.1	-
Set 2: HILL Voce Ziegler	Classical and Indent test	F= 1.11 G= 1.11 H= 0.89 N= 3	K= 275 σ_0= 8.5 n= 439	C_A= 930 G_A = 18.1

Table E.1.1: Material data (Units: N, mm)

2. Line test (AlMgSc, As Received + Cold rolling)

This test is used to compare the accuracy of material data.

In the FEM simulations, the nodes along the edges are fixed. The tool force is computed by the static implicit strategy. The Coulomb's friction coefficient of 0.05 is applied between the tool and the sheet. The mesh is adjusted to limit the number of elements (576 elements) while keeping accuracy (Figure E.2.1), taking into account the symmetry. The same shell elements as in the inverse method are used.

Figure E.2.2 shows that the set 2 (Voce/Ziegler) predicts a better level of the tool force.

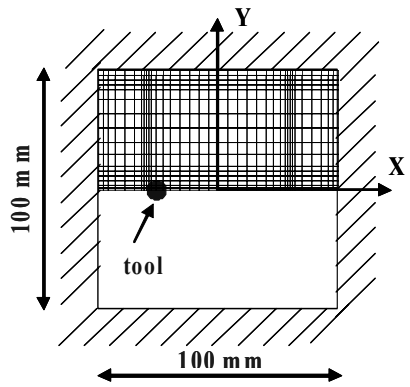

Figure E.2.1: Line test: geometry and meshing

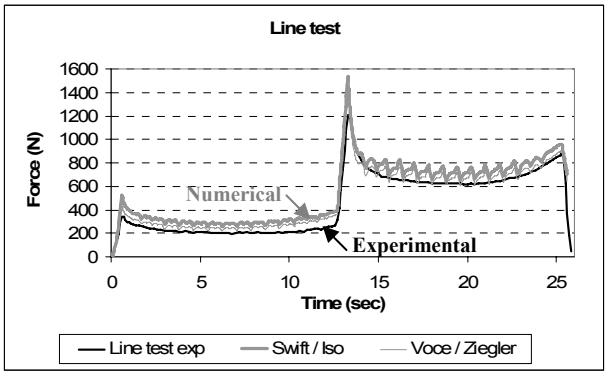

Figure E.2.2: Line test: tool force evolution Comparison between experiment and simulations

3. Bending test (AlMgSc, As Received + Cold rolling)

This test, described in section: "AlMgSc characterisation / As Received sheets + Cold rolling + Annealing" has been performed on a bending machine and didn't predict the same behaviour for the two directions: // to RD (D) and ⊥ to RD (L) (see Figures A.2.10, A.2.11 and E.3.1). It was also simulated using the two material models of Table E.1.1.

The behaviour described by the numerical models is the same in both RD / TD directions because the tensile and shear tests didn't show difference in the two directions. The simulation is performed with four shell elements.

As results, the unit moment: $\sigma^* = M / b.S_0^2$ versus strain: $\varepsilon_b = S_0 / 2*R_m$ is computed (see Figure E.3.1). The numerical model could not provide a good estimation of the experimental results. This simplified model with shell elements doesn't seem to be adapted to describe such a complex test with a high level of out-of-plane shear.
Other element type should be investigated to simulate such test.

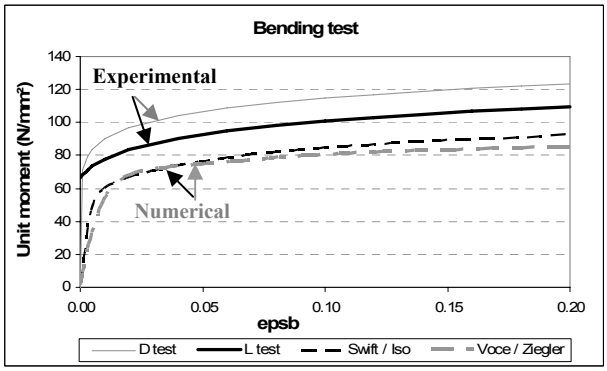

Figure E.3.1: Bending test: unit moment - Comparison between experiment and simulations

4. Cone test (AlMgSc, As Received + Cold rolling)

This test is used as a second validation of the material data. The circular metal sheet with a thickness of 0.5 mm is clamped. 30 contours are performed with a tool radius of 5 mm, a step down of 0.5 mm between successive contours and a wall angle of 40° (Figure E.4.1).

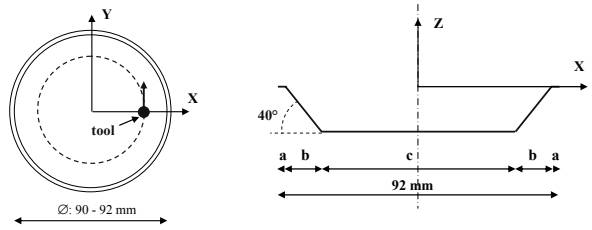

Figure E.4.1: Description of the Cone test (a=1 mm, b= 17.77 mm and c= 54.25 mm)

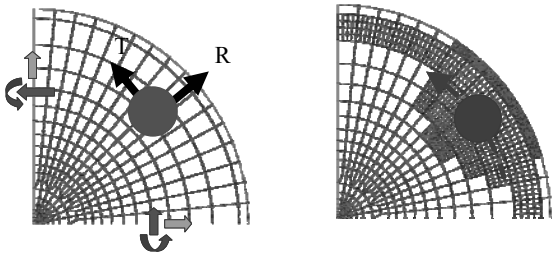

Figure E.4.2: Cone test: Initial mesh, radial (R) and tangential (T) directions, boundary conditions and mesh evolution

The mesh used to simulate the process is presented in Figure E.4.2. To reduce the computation time, only a quarter of sheet is modelled and rotational boundary conditions are imposed by a link between the displacements of the edges [12]. The remeshing method is used to refine the mesh of the elements close to the tool. The refinement is removed when the tool goes further but it is kept when the element distortion is high. This method is described in section: "SPIF – Numerical model improvement".

Two meshes were tested: a very fine mesh (2692 elements) without the remeshing method and the coarse mesh of Figure E.4.2 (248 elements) combined with the remeshing method. The level of the force is almost the same for both simulations but the computation time is divided by a factor of 49 for this second case. The Coulomb friction coefficient ϕ is 0.10.

The radial F_R, tangential F_T and axial F_Z force components (Figure E.4.2) and the norm of the force F_{tot} are compared with the experimental ones. To simplify the comparison, the numerical force evolution during each contour is replaced by the average of the force. This one is computed when the tool is in the central third of each contour to avoid small inaccuracy due to the boundary conditions.

Figure E.4.3 shows a better correlation between the level of the numerical and measured axial tool force for the set 2 (Voce/Ziegler). The combinaison of an isotropic hardening law with saturation (Voce), the kinematic hardening and the use

of the indent test in the inverse method giving information about the out-of-plane material behaviour, has a high impact on the accuracy of the force evolution.
Figure E.4.4 shows similar results with a fine meshing without remeshing and a coarse meshing combined with the remeshing method. Only a small difference can be observed for all of the force components.

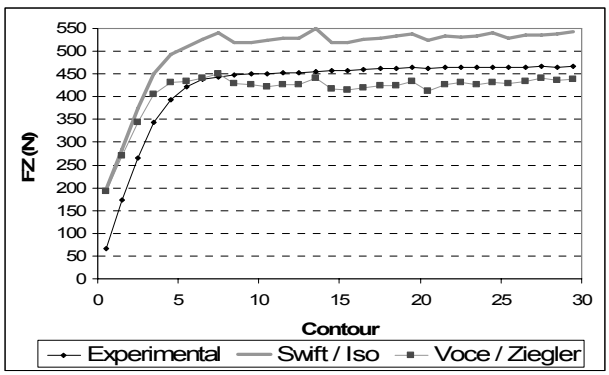

Figure E.4.3: Axial force predicted by sets 1 and 2

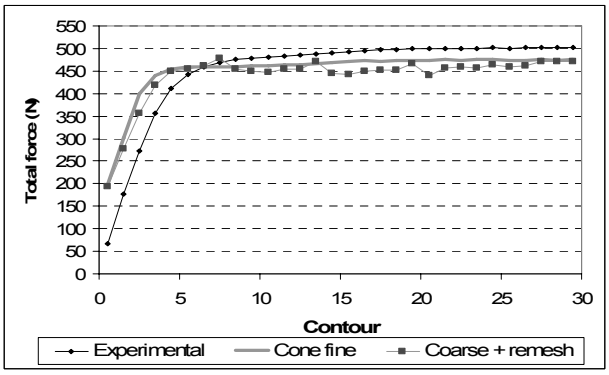

Figure E.4.4: Comparison with / without remeshing

Figures E.4.5 & E.4.6 shows the numerical forces obtained with the set 2 and the experimental values. It is clear that this model combined with a good material behaviour description gives a good prediction of all of the force components. The final predicted levels are respectively 0.9%, 19%, 5.8% and 6.1% lower than the experimental F_R, F_T, F_Z and F_{tot} components. It is possible to improve the level of the F_T component by adapting the friction coefficient. It was observed in [13] that friction has almost no impact on F_R and F_Z and that F_T is linearily affected by the friction coefficient. The ratio F_T/F_Z reached by two simulations with ϕ= 0.05 and ϕ= 0.10 was respectively: 0.157 and 0.212. By extrapolation, the value: ϕ= 0.14 should lead to the experimental ratio F_T / F_Z of 0.256.

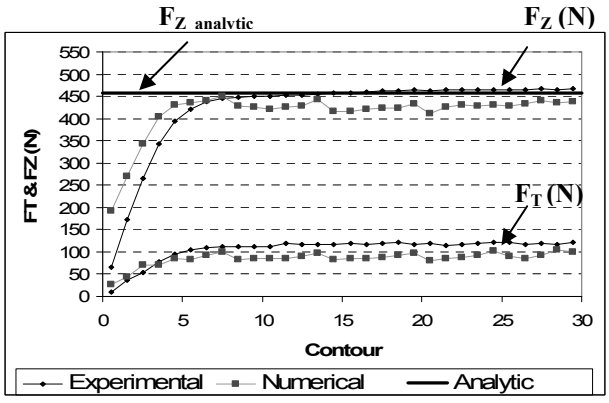

Figure E.4.5: Comparison of the numerical, analytical and experimental axial and tangential forces

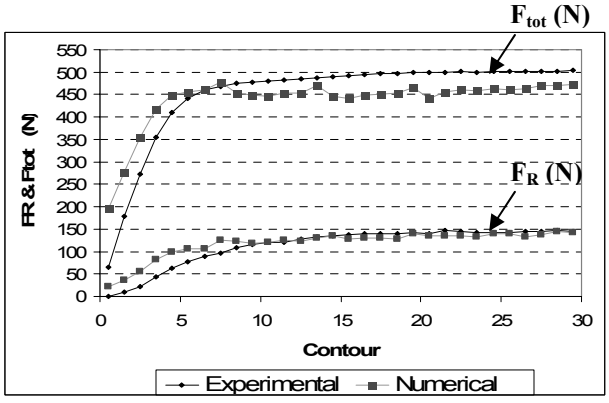

Figure E.4.6: Comparison of the numerical and experimental total and radial forces

The steady state axial force F_{Z_S} can be predicted by a generalized formula [14] based on the tensile strength of the material R_m, the sheet thickness t, the tool diameter d_t, the scallop height Δh and the wall angle α (Eq. E.4.1):

$$F_{Z\_S} = 0.0716.R_m.t^{1.57}.d_t^{0.41}.\Delta h^{0.09}.\alpha.\cos\alpha \qquad \text{(Eq. E.4.1)}$$

where F_{Z_S} is expressed in N, R_m in N/mm², t, d_t and Δh in mm and α in degrees.
The scallop height Δh is linked to the depth increment ΔZ, the tool diameter and the wall angle by the relation (Eq. E.4.2):

$$\Delta z = 2\sin\alpha\sqrt{\Delta h(d_t - \Delta h)} \approx 2\sin\alpha\sqrt{\Delta h.d_t} \qquad \text{(Eq. E.4.2)}$$

The tensile strength determined by the tensile tests is 352 MPa, the scallop height is 0.0151 mm and thus the force prediction F_{Z_S} is equal to 458.5 N. This level represented in Figure E.4.5, gives a good prediction for this alloy and geometry.

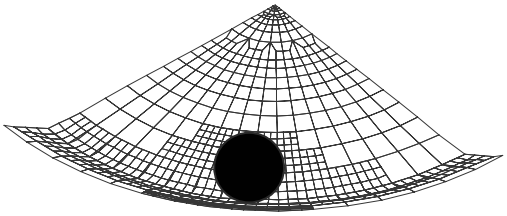

Figure E.4.7: Shape throughout contour 11

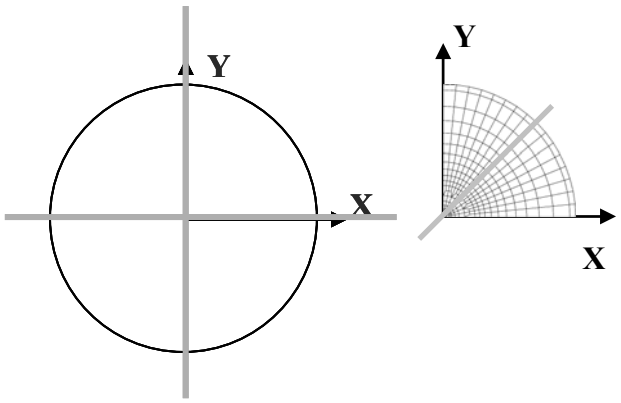

Figure E.4.8: Position of the sections

The experimental shapes in X= 0 and Y= 0 sections (Figure E.4.8) are obtained by digital camera measurement at the end of the process when the tool is removed. Two different experimental SPIF machines are used: Maho and the robot. The measurements represent the surface shape on tool side: the inner shape. The average layer is computed (Figure E.4.10) point by point from the thickness (Figure E.4.9) and the local wall angle. The numerical shape is extracted from the section: X= Y to avoid small imprecision due to boundary conditions. It is the average layer obtained by the nodes coordinates. These figures indicate a good prediction of the shape.

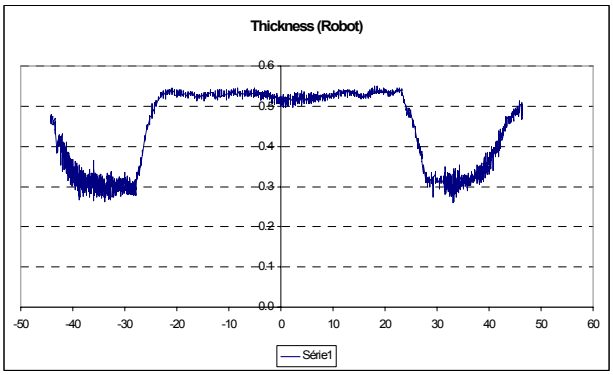

Figure E.4.9: Experimental thickness

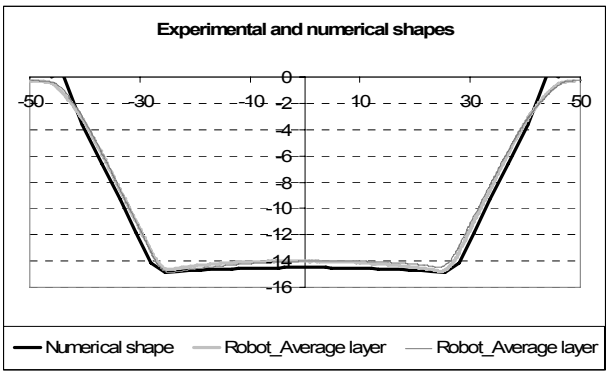

Figure E.4.10: Comparison of the average shapes

5. Pyramid test (AA3103)

Another shape, a pyramid with two wall angles, formed with by the SPIF method has been investigated (Figures E.5.1 & E.5.2) to test our model on a complex shape and to see whether our model predict a twist effect as described in the article publicated by H. Vanhove. As it is described in [P.6], the phenomenon is observed only in case of high wall angle, higher than the maximum forming angle of AlMgSc. For this reason and also for problem of available sheet size, the pyramid was performed on AA3103. This material was already studied and characterised in a previous project [8].

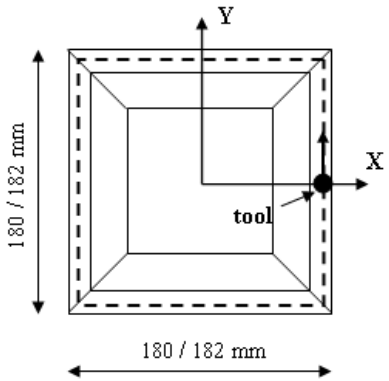

Figure E.5.1: Pyramid test description

The squared sheet (182 * 182 mm²) with a thickness of 1.5 mm is clamped. With a tool radius of 5 mm, 63 and 27 contours are performed respectivelly with a wall angle of 65° and 30° and a step down of 0.5 mm.

Due to symmetry, only the half of the sheet is meshed. The boundary conditions are adapted as it is described in figure E.5.3. A coarse meshing with 800 shell elements combined with the remeshing method is used.

Another fine meshing with 1800 elements is also used as benchmark to show the accuracy of the results predicted by the simplified model.

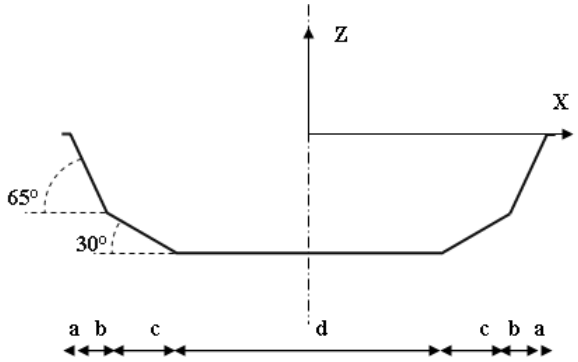

Figure E.5.2: Pyramid shape

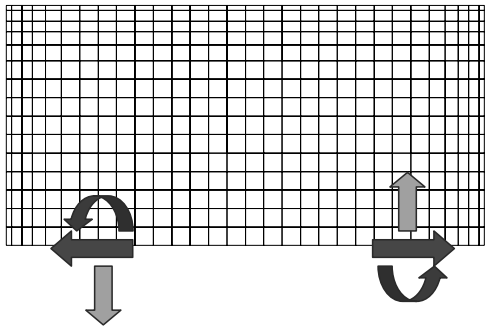

Figure E.5.3: Meshing and boundary conditions

The first simulation with the fine meshing shows that the model is adapted to simulate the process (Figure E.5.4) but the computation time is high in this case.

The simulation with the coarse mesh combined with the remeshing method should help to reduce the computation time but it stopped before the end due to convergence problems. It indicates that investigations must be done to solve the problem by optimising the remeshing method parameters.

The force and the shape will be studied to verify the accuracy of both numerical models.

The reverse twist effect as described in [P.5] was not observed in this model. It is clear that such shell elements are rather simple. Once again, as observed in case of the bending tests, other complex shell elements should be developped to help to predict such phenomenon.

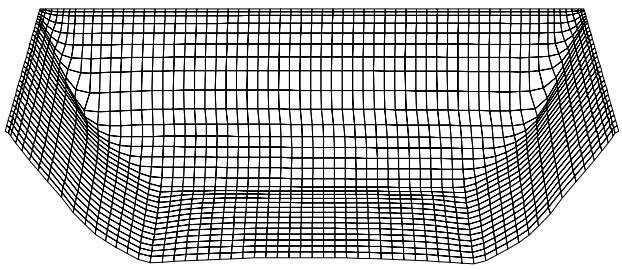

Figure E.5.4: Final shape predicted by the fine mesh

Statement & conclusions

1. Cold rolling

The cold rolling processes (conventional and asymmetric) performed on Al-Mg-Sc sheet/bulk induced, as expected, a strong strain hardening in the material, but no grain refinement due to the mechanical deformation was observed. Concerning asymmetric rolling, the redundant shearing component was not high enough for a sub-grain refinement.

Moreover, this material didn't show a good behaviour under cold rolling because the precipitates in the microstructure and also the surface quality lead to cracks during conventional rolling.

2. I-ECAP process

The new process of I-ECAP can be used for bars, plates and sheets. In the current project, the emphasis was on producing UFG sheets. However, the starting point was I-ECAP of bars, which, was carried out at an elevated temperature. This led to the next step of I-ECAP being, for the first time, successfully used for direct SPD of sheets, which resulted in substantial refining of the grain structure of an AlMgSc alloy. However, the trials have shown that there are still a few problems, which require further work.

One of these problems is manual feeding of the material, which has to be replaced with automated feeding, synchronised with the reciprocating movement of the punch. This should allow higher punch frequency to be used (within the limits of the hydraulic servo actuator) and productivity increased.

Control over geometry of strips is a bit problematic. The thickness of the strips depends on the bottom position of punch, which in turn changes with load (due to press/tool deflection) and tool/press temperature (due to thermal expansion). This requires precise measurement and control of the punch position by using a temperature resistant displacement transducer and a control loop, which feeds the punch distance information to the hydraulic servo actuator.

The strips tend to be slightly bent like in rolling, which requires straightening. This should be possible to avoid by better (FE informed) design of the tools. However, there may also be another bending, this time in the plane of the sheet. It may result

from an uneven gap between the punch face and the die surface as well as different friction conditions along the strip edges.

Regarding the tool design, the punch and the feeder proved to work properly, while the die experienced problems. Its redesign will be considered to take into account the fact that I-ECAP causes fatigue of the die material. In this series of experiments, five pairs of strips were subjected to six passes, using about 1000 punch strokes in each pass. This resulted in about 30000 load cycles.

The load on the punch was 150 kN, which was about 50% more than in the case of I-ECAP of square bars of the same cross-section area ($10\times10=2\times50$), made of the same material and processed at the same temperature. This means that predicting the maximum force, by scaling it according to the ratio of the cross-section areas, works only for the same shapes.

Despite the above problems, the process of I-ECAP is very promising. It allows the feeding force to be greatly reduced (to about 10% of the forming force). This enables long, possibly infinite bars, plates and sheets to be fed. The latter option would require a redesign of the feeding system, but taking into account the small feeding force (or even no feeding force at all), it should not be too difficult. This would open up industrial applications and help promote the use of UFG metals.

3. ECAP process

ECAP of cylindrical specimens could be carried out without problems. The optimal ECAP temperature is 200°C and both routes A or C are feasible. The production of rectangular samples has been hampered by severe technical problems with the newly designed die.

Irrespective of the shape of the samples, the microstructure after 8 ECAP passes has not yet reached the state of a real submicron material. More passes seems to be necessary but this is difficult in practice because –even with the cylindrical samples– cracks appear on the sample surface after 8 ECAP passes.

The reason that a submicron grain structure is hard to obtain in this AlMgSc alloy, is probably related with the presence of nano-size coherent Al_3Sc or $Al_3(Sc_xZr_{1-x})$ particles of the LI_2 structure. These particles hamper the dislocation movement and pin the (sub)grain boundaries and retard the evolution of the substructure into a submicron grain structure.

4. SPIF process

In the framework of the project the As Received AlMgSc material was characterized for SPIF. Three aspects were closely studied.

Firstly, the geometrical limitation for SPIF of AlMgSc is explored using a standard cup test. The outcome of this set of tests is a maximum obtainable draw angle for a particular thickness, tool diameter and scallop height. For As Received AlMgSc (3.2 mm)+ cold rolling (0.5)+ annealing with a standard spherically tipped tool of Ø10 mm and scallop height of 0.005 mm a maximum wall angle of 46° is found. Compared to other materials this is a fairly low value.

Practically, it means that using conventional SPIF all geometries are restricted to wall angles below 46°. Using strategically chosen nesting, optimized toolpath strategies and local heating of the workpiece steeper wall angles can be formed.

Secondly, during the course of the project an analytical force prediction model was developed for this material and integrated in a generalized model, which aims to predict the forming forces for any material. Forming forces in SPIF are characterized by the draw angle, tool diameter, scallop height and initial sheet thickness. Of these parameters the draw angle has the most irregular influence pattern.

An in-depth study was done to explore the correlation between draw angle and forming forces. The result of this study showed a relation of 'α cosα' where α equals the draw angle. After this a general factorial analysis was performed varying all influential parameters between two values. The result of this analysis is a regression formula for the main force component Fz:

$$F_Z \approx t^{1.48}\, d_t^{0.767}\, \Delta h^{0.1}\, \alpha^{1.11}\, cos\alpha \ldots$$

When comparing with earlier studied materials a relation can be observed between the tensile strength and this force component. This leads to a more generalized formula with which the forming forces of any material can be determined:

$$F_Z = 0.0562\, R_m\, t^{1.53}\, d_t^{0.51}\, \Delta h^{0.093}\, \alpha^{1.055}\, cos\alpha \ldots$$

Finally the impact of SPIF on the As Received material (3.2 mm) + cold rolled (0.5 mm) + annealing was studied, to verify the structural integrity of workpieces formed by SPIF. A set of pyramids with wall angles close to and 5 degrees under the maximum wall angle was formed and samples extracted. A variety of simple tensile

tests and microstructure analysis were performed on these samples. Results of these tests were discussed earlier in the report.

To conclude we can state that SPIF is a valid production process for AlMgSc but do to the low maximum forming angle steep walled parts are need additional heating and toolpath strategies or are even completely outside the process window.

5. Material data identification

It is observed that the identification of material data is far from being trivial. An indent test, performed with the SPIF setup, inducing heterogeneous stress and strain fields similar to those present in the SPIF process is combined to classical tests. It provides information for both in-plane and out-of-plane strain states and gives a better prediction of the global material behaviour than when using simple homogeneous classical tests.

6. SPIF simulation

Previous researches indicate that it is very difficult to predict accurately the force in the SPIF process.

This study which combines the request of accuracy and a short computation time leads to the choice of a mixed isotropic-kinematic hardening described by Voce's and Ziegler's laws, a good identification procedure and some simplifications in the numerical model.

The use of Shell elements, a coarse mesh combined with the remeshing method, a 90° pie and rotational boundary conditions aim to reduce the computation time. It was possible to simulate the 30 contours of the Cone test with a simple personal computer within 5 hours and last but not least, with a good precision.

Publications and knowledge transfer

[P.1]. C. Bouffioux, P. Eyckens, C. Henrard, R. Aerens, A. Van Bael, H. Sol, J.R. Duflou, A.M. Habraken. Identification of material parameters to predict Single Point Incremental Forming Forces. In Proc. of the Esaform 2008 Conference, April 23 – 25, 2008, France

[P.2]. C. Bouffioux, C. Henrard, P. Eyckens, R. Aerens, A. Van Bael, H. Sol, J.R. Duflou, A.M. Habraken. Comparison of the tests chosen for Material Parameter Identification to Predict Single Point Incremental Forming Forces. In Proc. of the IDDRG 2008 conference, June 16 – 18, 2008, Sweden

[P.3]. C. Lequesne, C. Henrard, C. Bouffioux, J.R. Duflou, A.M. Habraken. Adaptive remeshing for incremental forming simulation. In Proc. of the Numisheet 2008 conference, September 1 – 5, 2008, pages 399-403, Switzerland

[P.4]. C. Bouffioux, P. Pouteau, L. Duchêne, H. Vanhove, J.R. Duflou, A.M. Habraken. Material data identification to model the single point incremental forming process. In Proc. of the Esaform 2010 conference, April 7 – 9, 2010, Italy – "in press"

[P.5]. H. Vanhove, J. Verbert, J. Gu, I. Vasilakos, J.R. Duflou. An experimental study of twist phenomena in single point incremental forming. In Proc. of the Esaform2010 conference, April 7 – 9, 2010, Italy – "in press"

[P.6]. A. Rosochowski, M. Rosochowska, L. Olejnik, B. Verlinden. Incremental equal channel angular pressing of sheets. 13th Int. Conference Metal Forming, September 19 - 22, 2010, Steel Research International (2010) Special Edition

Acknowledgments

The authors would like to thanks Aleris for the material supply and Sonaca for their efficient collaboration in the project definition and their regular participation.

References

[1]. V.M. Segal: Materials Science and Engineering A, 271 (1999), 322-333.

[2]. L. Olejnik, A. Rosochowski: 12th Int. Conference Metal Forming, Krakow, 21-24 September, 2008, Steel Research International, 79 Special Edition (2008), 439-446.

[3]. A. Rosochowski, L. Olejnik: Proc. of the 10th Int. Conference on Material Forming, Esaform 2007, April 18-20, 2007, Zaragoza, Spain, American Institute of Physics, Proceedings 907 (2007), 653-658.

[4]. A. Rosochowski, L. Olejnik: Proc. of the 11th Int. Conference on Material Forming, Esaform 2008, April 23-25, 2008, Lyon, France, International Journal of Material Forming, 1 Suppl 1 (2008), 483–486.

[5]. A. Rosochowski, L. Olejnik, M. Richert: Materials Science Forum, 584-586 (2008), 139–144.

[6]. L. Olejnik, A. Rosochowski, M. Richert: Materials Science Forum, 584-586 (2008), 108–113.

[7]. A.M. Habraken: Contribution to the modelling of metal forming by finite element model. Ph D thesis of University of Liege (1989).

[8]. C. Bouffioux, C. Henrard, P. Eyckens, R. Aerens, A. Van Bael, H. Sol, J.R. Duflou, and A.M. Habraken: Comparison of the Tests Chosen for Material Parameters Identification to Predict Single Point Incremental Forming Forces. In Proc. of the IDDRG 2008 conference, Olofström, Sweden, 1 (2008), 133-144.

[9]. C. Henrard: Development of a Contact Model Adapted to Incremental Forming. Master's thesis, September 2005, University of Liège. Supervisor: Dr. Anne Marie Habraken.

[10]. P. Flores, L. Duchêne, C. Bouffioux, T. Lelotte, C. Henrard, N. Pernin, A. Van Bael, S. He, J.R. Duflou, A.M. Habraken: Model Identification and FE Simulations: Effect of Different Yield Loci and Hardening Laws in Sheet Forming, International Journal of Plasticity, 23/3 (2007), 420-449.

[11]. L. Duchêne, A.M. Habraken: Analysis of the sensitivity of FEM predictions to numerical parameters in deep drawing simulations, European Journal of Mechanics - A/Solids, 24 (2005), 614-629.

[12]. C. Henrard, C. Bouffioux, P. Eyckens, H. Sol, J.R. Duflou, P. Van Houtte, A. Van Bael, L. Duchêne, A.M. Habraken: Forming Forces in Single Point Incremental Forming. Computational Mechanics (2010) – Submitted.

[13]. P. Eyckens, J.R. Duflou, A. Van Bael, P. Van Houtte: The significance of friction in the single point incremental forming process, In Proc. of the Esaform 2010 conference, April 7 – 9, 2010, Italy – "in press".

[14]. R. Aerens, P. Eyckens, A. Van Bael, and J.R. Duflou: Force prediction for single point incremental forming deduced from experimental and FEM observations, International Journal of Advanced Manufacturing Technology (2009) - Doi:10.1007/s00170-009-2160-2.